PULSED-LASER DEPOSITION OF PEROVSKITE POLAR OXIDE FILMS ON $SRTIO_3$ AND STUDY OF INTERFACIAL TRANSPORT PROPERTIES

LI DANFENG

M.Phil

The Hong Kong Polytechnic University

2011

The Hong Kong Polytechnic University
Department of Applied Physics

Pulsed-Laser Deposition of Perovskite Polar Oxide Films on $SrTiO_3$ and Study of Interfacial Transport Properties

Li Danfeng

A thesis submitted in partial fulfillment of the requirements
for the degree of Master of Philosophy

September 2010

CERTIFICATE OF ORIGINALITY

I hereby declare that this thesis is my own work and that, to the best of my knowledge and belief, it reproduces no material previously published or written, nor material that has been accepted for the award of any other degree or diploma, except where due acknowledgement has been made in the text.

_____ (Signed)

LI Danfeng (Name of student)

To my beloved parents

ABSTRACT

Recently, motivated by the discovery of a high-mobility (~10^3 cm^2 V^{-1} s^{-1} at 4.2 K) quasi-two dimensional electron gas (q2-DEG) with high carrier density (10^{14} cm^{-2}) at heterointerfaces combining two band insulators $LaAlO_3$ (LAO) and $SrTiO_3$ (STO), numerous electronic properties at such interface have been deeply investigated, revealing superconducting and intriguing magneto-transport properties at low temperatures. These significant results show the potential for this oxide interface to be applied in nanoelectronics.

However, there is still an ongoing debate concerning the origin of the conducting interface formed between LAO and STO. Since the fundamental mechanism of generating the q2-DEG at perovskite oxide interfaces has always been the main issue of this field, instead of investigating deeply into the physics behind LAO/STO interfaces, it would also be worthy to fabricate other heterointerfaces using another insulating perovskite, which has the same polar atomic planes as LAO, on top of STO.

Based on this idea, another “polar” perovskite Dysprosium Scandate ($DyScO_3$, DSO) was chosen in this project, and the electronic transport properties of the DSO/STO polar heterointerface grown at different oxygen pressures were studied. This heterointerface not only holds some similarities to LAO/STO interface, such as metallic behavior, high mobility and high carrier density, but also presents some phenomena not usually been observed at the LAO/STO interface, such as metal-to-semiconductor (M-S) transition. The electric field effect to the formed electron gas has also been revealed, indicating pronounced modulation of electric doping level and quantum phase transition. This heterostructure promises the potential interest for understanding quasi-two-dimensional electron gases as well as its applications in all-oxide device, thus opens new route to complex oxide physics and ultimately for the design of devices in oxide electronics.

In addition, it is generally believed that STO itself plays a vital role in generating q2-DEG at the LAO/STO heterointerfaces. In order to deeply understand the functions of STO and tackle the potential in applications through building LAO/STO conducting interfaces on artificial STO, the LAO/STO (artificial)/STO (single-crystal) structures were also studied. LAO/STO/STO structures were fabricated using pulsed-laser deposition by firstly growing an artificial STO layer on top of STO single crystal and followed by sequential growing of LAO on top. Structural, transport and dielectric measurements have been performed and the importance of STO in such conducting heterointerfaces has been demonstrated. The results show that with artificial STO layer grown at different temperatures the conductivity of LAO/STO heterointerfaces can be very different.

LIST OF PUBLICATIONS

1. D. F. Li, Y. Wang, and J. Y. Dai, "Tunable Electronic Transport Properties of $DyScO_3/SrTiO_3$ Polar Heterointerface", *submitted to Applied Physcis Letter*.

2. D. F. Li, S. Gariglio, C. Cancellieri, A. Fête, A. D. Caviglia, and J.-M. Triscone, "Effect of the artificial $SrTiO_3$ on the $LaAlO_3/SrTiO_3$ interface electronic properties", *Manuscript*.

3. Y. Wang, D. F. Li, and J. Y. Dai, "Microstructure and magnetic properties of a novel spinel $(Zn,Co)Fe_2O_4$ thin film on the $SrTiO_3$ substrate", *accepted by Journal of Crystal Growth*.

4. K. C. Chan, P. F. Lee, D. F. Li, and J. Y. Dai, "Memory characteristics and tunneling mechanism of Au nanocrystals embedded in $DyScO_3$ high-k gate dielectric layer", *accepted by Semiconductor Science and Technology*.

ACKNOWLEDGEMENT

I would like to express my sincere gratitude to my supervisor Dr. J. Y. Dai for his supervision and support throughout my M.Phil study. I am so grateful for the latitude and care he gave me. I will never forget that he was always providing ever-present understanding and trust especially when I was upset by the difficulties that I encountered during the research. I thank him for his invaluable guidance and remarkable comments that have been always with me in last two years. I am now more than glad that I met with him at a workshop held in PolyU in 2007 and I am so proud to be his student.

I would like to specifically thank Prof. J.-M. Triscone in Condensed Matter Physics Department, University of Geneva, for accepting me as an exchange research student staying in Geneva, Switzerland. Prof. Triscone's personality and great passion on physics inspired me and lightened my interest on physics. Without his encouragement and guidance, I cannot complete the work in Geneva, which is one of the most important parts in this project. And I really like the open discussions in the group. I also wish to thank Dr. S. Gariglio for his invitation and assistance on every aspect. He is one of the kindest people that I ever met.

I would like to thank Prof. H. W. L. Chan for her support and guidance. Without her, I could not have managed to meet with Dr. Dai so that I would not have the chance to come to Hong Kong.

I would like to thank Dr. Y. Wang for the discussion and the suggestions he provided.

I sincerely thank Dr. P. F. Lee and Ms. K. C. Chan who are my friends and colleagues. They have been teaching me so much since the time when I was still a "stranger" in our group.

I want to thank Dr. W. Huang, Dr. Y. Wang, Dr. J. X. Zhang, Dr. D. Zhou, Mr. J. Liu, and Ms. Y. Chen in our group for their kindly help in my study. Thanks also go to Dr. G. Y. Gao, Mr. K. Zhang, Mr. Z. P. Wu, Mr. Y. Jiang and Mr. L. F. Fei.

I would also like to thank Dr. N. Reyren, Dr. C. Cancellieri, Dr. P. Zubko, Dr. M. Gibert, Dr. A. Sambri, Mr. A. Caviglia, Mr. A. Fete, Mr. R. Scherwitzl and Ms. J. Guyonnet in Prof. Triscone's group for their useful help and fruitful discussions. It is they that make me experience the free atmosphere and traditions of Physics in Europe. Special thanks are given to Mr. M. Lopes for his technical support on my experiment and my thesis. Thank Ms. E. Schwarz for the accommodation arrangement in Geneva.

I also want to thank Dr. J. Wang for his trust and help during my teaching assistant work under his guidance.

I thank Mr. M. N. Yeung from Materials Research Center for the technical assistance.

Financial support from The Hong Kong Polytechnic University Research Studentship and Overseas Research Student Attachment Program is gratefully acknowledged.

Finally, I give my appreciation to my parents, who raised me up so laboriously, for the education and edification they gave me.

TABLE OF CONTENTS

LIST OF ABBREVIATIONS

Abbreviation	Description
AFM	Atomic force microscopy(e)
BHF	Buffered-HF
DSO	Dysprosium Scandate, $DyScO_3$
LAO	Lanthanum Aluminate, $LaAlO_3$
Laser-MBE	Laser-molecular beam epitaxy
MIT	Metal-insulator transition
MR	Magnetoresistance
NGO	Neodymium Gallate, $NdGaO_3$
PL	Photoluminescence
PLD	Pulsed-laser deposition
q2-DEG	Quasi-two-dimensional electron gas
RHEED	Reflection high-energy electron diffractions
RT	Room temperature
STO	Strontium Titanate, $SrTiO_3$
TEM	Transmission electron microscopy(e)
u.c.	Unit cell
XRD	X-ray diffractions
2D	Two dimension(al)
3D	Three dimension(al)

CHAPTER 1

INTRODUCTION

1.1 Background of the Thesis

"Often, it may be said that the interface is the device." [1] This "famous" quote is from Nobel laureate, H. Kroemer. It describes the amazing fact that in many devices it is physics arising at the interface, rather than the bulk materials themselves, leads to the functionality. This fact also inspires a large amount of significant scientific work on different material interface systems, from metals to insulators, and from typical semiconductors to transition metal oxides. Those work and interfaces have somehow changed our modern world and the life we are living for. As we will see, the $LaAlO_3/SrTiO_3$ interfaces, particularly known as a novel conducting interface between insulators is a recent representative example of the interface engineering.

Actually, modern devices whose functions are based on the interfacial properties are quite common in our daily life. One prominent example is the electronics made from the semiconductor heterostructures. The history for studying the semiconductors currently in use can originate to a few decades before. Their transport properties, which are along and across the interfaces between two different materials or two semiconductors with different doping levels, yield real success of integration of electronic devices. Nowadays, various types of transistors are designed based on different kinds of interfaces and heterostructures. Those structures and devices become more and more complex and sophisticated, and are produced in a great amount. This success indeed was stimulated by the large development in the techniques for preparing and growing semiconductor heterostructures. By the benefit of this advancement, one can even modulate the local band structure thus generate new special electronic systems at the hetero-interfaces, like often used and studied two-dimensional electron gases (2DEG) in semiconductor heterostructures [2].

What exactly makes the interfaces so fascinating? Actually, miniaturizing the devices to nanoscales demands a deep understanding of the surfaces and interfaces. At the same time, such surfaces and interfaces are so fascinating because the electronic systems can differ from bulk due to many reasons. First of all, due to the broken translational symmetry, the crystal field can be reconstructed. Furthermore, atomic reconstruction may happen in the form of changing atoms' positions. These two factors can directly influence the bonding conditions and lattice constants. In addition, defects can be generated and incorporated into the interfaces to help building the atomic reconstructions. And also, the possibility of variation of chemical composition at interfaces from bulk ratio gives rise to local profiles that are special compared to bulk constituents. Ultimately, all of these can modify the band structures at the interfaces and shift electronic states. Utilizing the combination of all these aspects therefore enables one to build semiconductor heterostructures with different properties. This made a great success in semiconductor physics and industry.

In the last few decades, a new group of materials named oxides semiconductor came into sight. In contrast to conventional semiconductors in which the electronic systems can be simply described as a combination of single charge particles by neglecting their interactions, oxides often have strongly correlated electrons. That is why oxides are studied as strongly correlated systems, behaving numerous functionalities; and many of them are being used in daily life served as sensors and actuators. In addition, such correlations can be strongly affected by external parameters, such as temperature, pressure and even doping (atomically or electronically). More importantly, not only the bulk properties can be tuned in oxides, the interfacial properties and correlation strength at interfaces can also be tuned. These modifications can bring huge functional changes.

Recently, several research groups reported experimental results showing that some properties can be improved by joining different oxide materials to build oxide heterostructures. For example, $PbTiO_3/SrTiO_3$ (ferroelectric/paraelectric) superlattices can give rise to improper ferroelectricity [3]. Superlattices of both

non-superconducting $BaCuO_2$ and $SrCuO_2$ can be superconducting [4]. Moreover, $CaRuO_3$ is paramagnetic and $CaMnO_3$ is antiferromagnetic; while the interface between them shows ferromagnetics [5].

These examples indicate that oxide interface is a rather active research field. Along with the possibility to control oxide thin film growth in unit-cell level and the large development in deposition techniques, more and more striking phenomena can be discovered. The startling results on oxide interfaces were even "awarded" one of the major scientific breakthroughs throughout the year from *Science* magazine in 2007. This work was originally stimulated by the discovery of A. Ohtomo and H. Y. Hwang in 2004, who firstly observed a surprisingly conducting sheet with high carrier mobility between two band insulators $LaAlO_3$ and $SrTiO_3$, depending on the precise control of atomic stackings [6]. Before entering this attractive area, I would like to give a short introduction on perovskite oxides and try to briefly summarize some contributing results related to the structural and transport properties of $SrTiO_3$, the basis of 2DEG, and finally discuss about main discoveries that have been made in the past few years on $LaAlO_3/SrTiO_3$ heterointerfaces.

1.2 Short Introduction to Perovskite Oxides

Compound perovskites have the general formula ABX_3, where A and B denote a large cation and a small cation, respectively, and X stands for an anion, which is usually either oxygen or halogen, that bonds A and B. So, just as the name implies, perovskite oxides represent the family with formula ABO_3. In the following context of this thesis, this family of "amazing" compound with this specific formula will be the focus of study.

Due to the multiple choices for the A site and B site of this compound, the chemical forms of perovskite oxides are enormous. In addition, perovskite oxides can usually condense in variable crystal structures, which include cubic, tetragonal, orthorhombic, rhombohedral and even monoclinic structures. Besides that, oxygen

stoichiometry [7], the amount of stabilized vacancies [8], doping by solid solution [9] and chemical substitution [10] can also be the effective factors to increase the diversity of perovskite oxides. As a result of all these possibilities, perovskite oxides can show a broad spectrum of physical and chemical properties such as metallic, semiconducting, insulating, superconducting, pyroelectric, piezoelectric, ferroelectric, (anti-)ferromagnetic as well as multiferroic behaviors [11-16]. These behaviors can be dramatically changed, enhanced or tuned especially when the perovskite oxides are under or near a structural phase transition due to the change of temperature or pressure; and if further extended to the thin films, substrate clamping effect, size and strain effect also have a great impact on these properties [17].

A typical unit cell of an ideal perovskite oxide with cubic structure is drawn in Fig. 1.1(a). The *A* ions are at the corners of the cube, where the whole three dimensional cubic networks are linked together; while *B* ions are at the center of the cell surrounded by 6 oxygen first neighbors which form a BO_6 octahedron. In this framework, the structure filling the whole space can also be described as a network of corner-sharing BO_6 octahedra, as shown in Fig. 1.1(b). The BO_6 octahedron is very important due to the reason that many structural and electronic properties are highly related to it.

A typical perovskite oxide can also be considered as a sequence of alternating AO and BO_2 atomic layers of (001) planes. The schematic is shown in Fig. 1.1(c). This way of instructive description is quite essential for this work here and will be referred later in this chapter when $LaAlO_3/SrTiO_3$ interfaces are discussed.

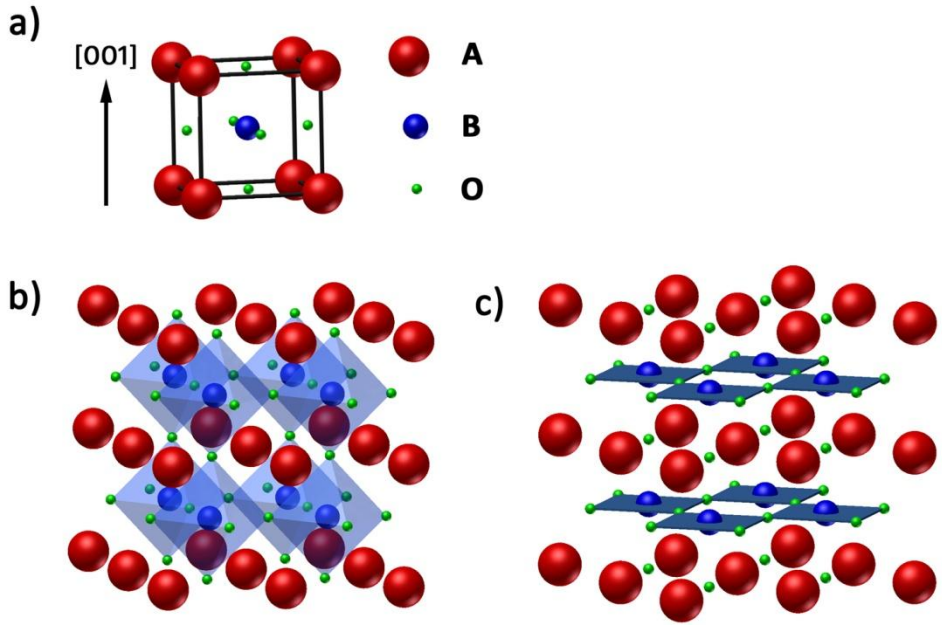

Figure 1.1 Schematic sketch of the perovskite oxide ABO_3 structure. (a) One cubic unit cell of perovskite oxide with *A* ions at the corners, a *B* ion at the center of the cube, and O ions at the center of every faces; (b) Perovskite oxide structure in terms of BO_6 octahedra networks; (c) ABO_3 structure can also be described as a stacking of AO and BO_2 atomic planes. (Sketch by M. Lopes)

1.3 Strontium Titanate ($SrTiO_3$)

Transition metal oxides in the form of perovskite exhibit abundant physics and extraordinary properties. Among them, $SrTiO_3$ is a twinkling example material. $SrTiO_3$ has been intensively studied during past decades. This is not only because $SrTiO_3$ is a band insulator (indirect band gap 3.2 eV) [18] and an incipient ferroelectric [19] ($T_C \rightarrow 0$ K), but also because of its unique electronic properties which can be tuned into insulators, semiconductors or metallic state by doping [20]. Even the superconductivity can be achieved in doped $SrTiO_3$ with critical temperatures <400 mK [21, 22]. Another reason for $SrTiO_3$ to be fascinating is that, due to the comparability of lattice constant and inert chemical nature, $SrTiO_3$ is regarded as a standard substrate for growing many oxides. For example, ferroelectrics [17], high-T_C superconductors (HTSs) [23] and Colossal Magnetoresistance (CMR)

oxides [24] have been successfully grown on $SrTiO_3$ substrate. In this work, $SrTiO_3$ was also used as standard substrate.

1.3.1 Structural Aspects and Dielectric Property of $SrTiO_3$

In a strain-free state, $SrTiO_3$ is cubic at room temperature (space group $Pm\bar{3}m$) with a lattice constant of 3.905 Å. In this cubic structure, the TiO_6 octahedra have well-aligned 90° angles. But when temperature is below 110 K, the material undergoes an antiferrodistortion in which the neighboring TiO_6 octahedra [Fig. 1.2(a)] are slightly rotated in opposite directions respect to formerly cubic axis [25]. This behavior leads $SrTiO_3$ to be tetragonal (space group $I4/mcm$) at low temperatures [26] and the phase transition is a second-order transition. However, since the tetragonal structure is still center-symmetric, this transition does not give rise to ferroelectricity down to cryogenic region.

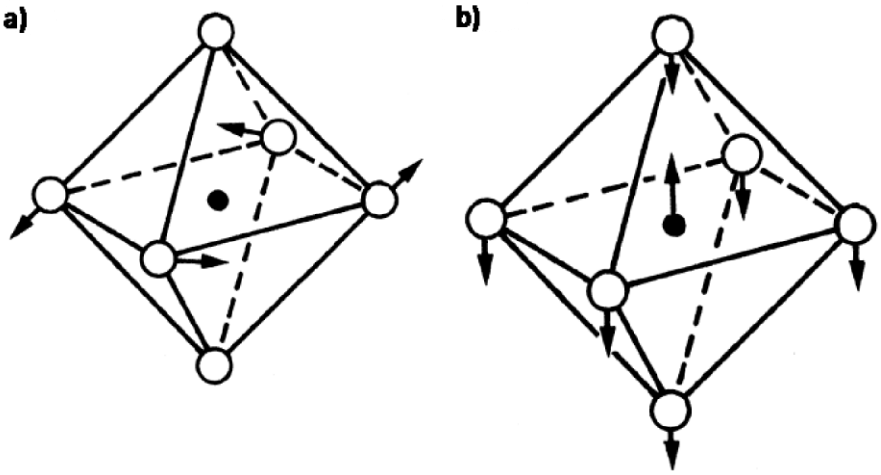

Figure 1.2 Schematics of two soft-mode-driven phase transitions in STO single crystals. (a) cubic-to-tetragonal second-order phase transition by antiferrodistortion (AFD) at about 110 K; (b) the ferroelectric phase transition which is suppressed by quantum fluctuation. The open circles are O ions and the solid circles are Ti ions. (Adopted from Ref. [27])

Theoretically, there should be another phase transition occur at about 40 K, at which Ti ions would prefer to shift respect to oxygen ions [Fig. 1.2(b)]. This, basically, should lead to the spontaneous polarization and thus ferroelectricity. In fact, this transition is strongly suppressed by the antiferrodistortion and quantum fluctuation so that ferroelectricity cannot be established in pure $SrTiO_3$ single crystal [28]. Hence, $SrTiO_3$ is regarded as an incipient ferroelectric and remains paraelectric when temperature approaches 0 K [19]. As a consequence, the dielectric permittivity increases dramatically with decreasing temperature especially at cryogenic region, from a few hundred at room temperature to up to 25k at 4 K in bulk samples. This increase of dielectric response is the same as in other ferroelectric materials, where the dielectric constant increases a lot when the material approaching the paraelectric-ferroelectric transition driven by lowering the temperature, such as in $BaTiO_3$ [29]. Furthermore, it is reported that at low temperatures, a reduction of dielectric constant can be observed upon applied electric fields, as shown in Fig. 1.3.

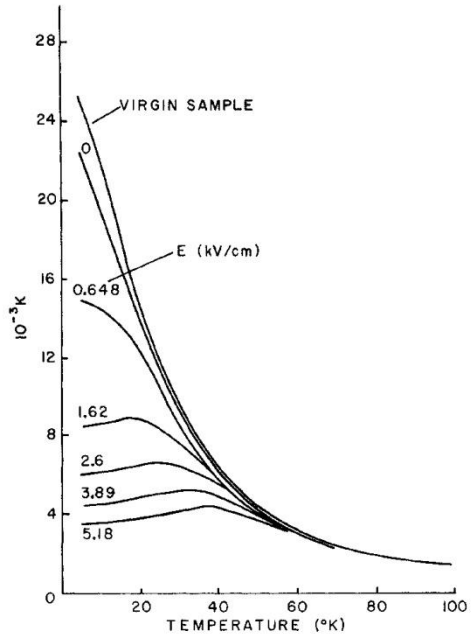

Figure 1.3 Temperature dependence of dielectric permittivity under weak-field for an unannealed crystal of $SrTiO_3$ with measuring field in [100] direction and dc bias fields along [100]. (Adopted from Ref. [30])

In homoepitaxial $SrTiO_3$ thin films, dielectric constant up to 4000 has been reported [31, 32], and high dielectric constant over 10^4 under external bias, which is near the bulk value, has also been achieved [33]. Moreover, $SrTiO_3$ thin films can also be driven into ferroelectric state by strain [34]. More details of $SrTiO_3$ thin films will be discussed later in Chapter 4 of this thesis. Exactly because of its large dielectric response, $SrTiO_3$ makes itself a proper candidate to be the gate dielectric in field effect configuration, which is utilized in this work, as to be shown in Chapter 3.

1.3.2 Transport Properties of $SrTiO_3$

Stoichiometric $SrTiO_3$ has a relatively large indirect band gap of 3.2 eV, which marks $SrTiO_3$ a band insulator. Thus $SrTiO_3$ has been used to combine with semiconductors, especially silicon, to fabricate metal-insulator-semiconductor based field effect transistors and data storage devices [31, 35]. $SrTiO_3$ has also been employed as an active component of superlattices and heterostructures with other ferroelectrics and oxides, because of its insulating dielectric nature [36, 37]. Examples include its use as an insulating barrier layer in Magnetic Tunnel Junctions (MTJs) [38] and as a dielectric layer for tuning the carrier density in manganite and cuprate thin films [39-41]. Among these, a special example is that it is served as a critical insulating component to generate quasi-two-dimensional electron gases (q2-DEG) in oxides heterointerfaces, as will be mainly discussed in this thesis.

$SrTiO_3$ can be doped into *n* type or *p* type to be conducting, where the *n*-type conduction can be conventionally doped either by substitution of A-site, i.e. Sr ions, or B-site, i.e. Ti ions (for example, substitute La^{3+} for Sr^{2+} [42] or Nb^{5+} for Ti^{4+} [10, 43]), or even by reduction to $SrTiO_{3-\delta}$ by creating oxygen vacancies in the crystals or thin-films [8, 20, 44]. Similarly, *p*-type doping can be achieved by substituting Ti^{4+} by some trivalent metal ions (for example, Fe^{3+} and Al^{3+} [45, 46]). Actually, the study of electronic transport properties of $SrTiO_3$ can originate to as early as 1964 [20], when people indeed were puzzled by and debating on some fundamental questions regarding the temperature dependent phase transitions occurred in bulk $SrTiO_3$. But

even before the paper of Ref. [20], it had been already noticed that usually pure $SrTiO_3$ crystal is transparent [Fig 1.4(a)] with highly insulating property; while after reduction of the crystal to $SrTiO_{3-\delta}$, for example by heating, the material will possess a wide range of absorption making the crystal blue or dull blue, as shown in Fig. 1.4(b). In the meantime, the material becomes conducting.

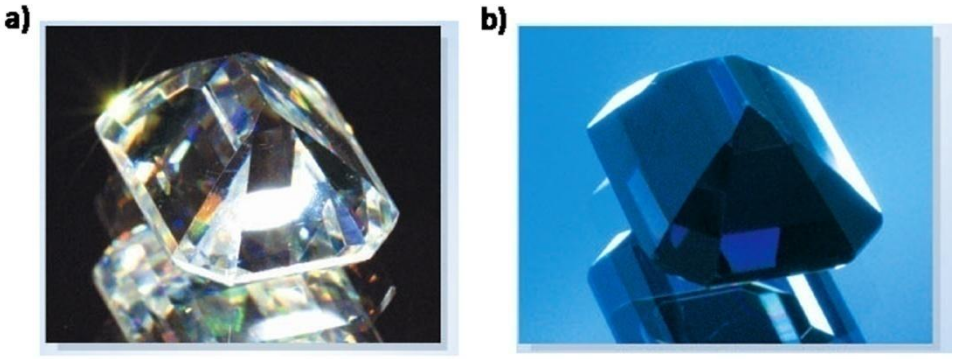

Figure 1.4 Photos of a $SrTiO_3$ crystal showing the effect of removing oxygen atoms, leaving vacancies in the crystal lattice: (a) the glistening oxidized gem is transformed into a dull blue, conductive crystal in (b). (Adopted from Ref. [47])

In past decades, detailed studies on the conductivity of doped $SrTiO_3$ and non-conductivity of non-doped $SrTiO_3$, as well as the mechanism underlying, have been widely performed in terms of characterization of temperature-dependent Hall coefficient, carrier density and mobility, residual resistance ratio (RRR) and magnetoresistance (MR) [48]. Figure 1.5(a) demonstrates temperature-dependent resistivity of $SrTiO_3$ crystals with different doping levels. In this picture, one can clearly see that the increase in doping level can significantly influence the conductivity. Especially in this case, reduction of $SrTiO_3$ at high temperature and more substitution of Ti^{4+} by Nb^{5+} ions will lead to high conductivity (low resistance state), and the change of the charge carrier concentration will also have great impact on the conducting behavior especially in low temperature regime (in this picture, more specifically, around a critical carrier concentration $n = n^*$, $d\rho/dT$ changes sign).

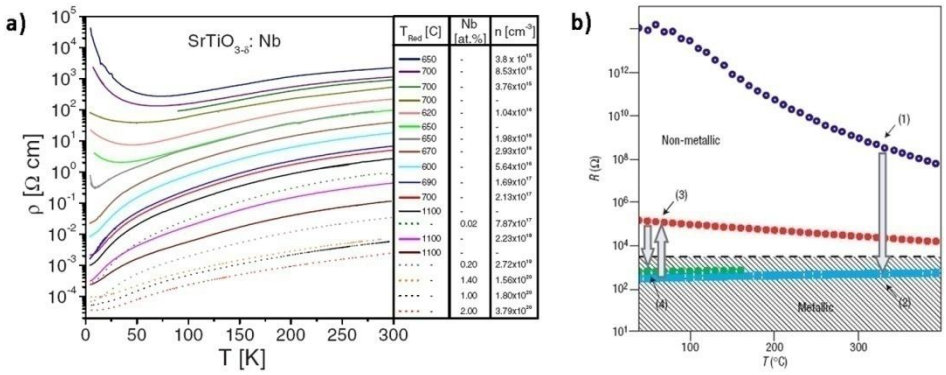

Figure 1.5 (a) Temperature dependence of the resistivity (log scale) of $SrTiO_3$ single crystals with different Nb doping levels or reduced at different temperatures (adopted from Ref. [48]); (b) Resistance switching in undoped $SrTiO_3$ single crystal and measurements of the resistance versus temperature: (1) the initial stoichiometric crystal, (2) after thermal treatment, (3) after re-oxidation, (4) after electroreduction (adopted from Ref. [49]).

This doping effect on conductivity indeed endows one with degree of freedom to tune the conductivity of $SrTiO_3$ crystal between bistable states, i.e., high resistance state (HRS) and low resistance state (LRS) [49], as shown in Fig 1.5(b). It would be particular promising if one can switch the conductance of $SrTiO_3$ between non-metallic and metallic states by applying an appropriate external electric field. Actually, taking the advantages of the ability to modulate nanometer-scale behaviors at the surfaces, one can use Atomic Force Microscope (AFM) to locally modify the oxygen profile at the surface of $SrTiO_3$ crystal thus switch the local conductance by playing with surface defects state, such as dislocations [49]. This opens an avenue for developing and assembling bistable nanowires on $SrTiO_3$, thus holds particular promise for terabit memory applications.

Interest in the electronic transport of $SrTiO_3$ was even further extended by the discovery of superconductivity dome under transition temperature of 400 mK, as shown in Fig 1.6(a), where a charge carrier concentration plane with charge carrier densities of 10^{19}-10^{21} cm^{-3} is formed [20-21, 50]. A similar superconducting dome was also discovered at $LaAlO_3/SrTiO_3$ interface [51], which is in fact a two

dimensional (2D) superconducting regime. Remarkably, it was pointed out that doping $SrTiO_3$ with oxygen vacancies of as small as 0.03% can sufficiently induce superconductivity in this intrinsic insulator [52], and this insulator-superconductor transition (IST) can be tuned electrostatically [53]. Moreover, it was demonstrated that the $SrTiO_3$ based heterostructures built with a ultra-thin Nb-doped $SrTiO_3$ film lying between a bottom $SrTiO_3$ buffered layer and a $SrTiO_3$ cap layer [Fig. 1.6(b)] can display both 2D superconductivity and 2D quantum oscillations (Shubnikov-de Haas oscillations) [54], as illustrated in Fig. 1.6(c) and Fig. 1.6(d).

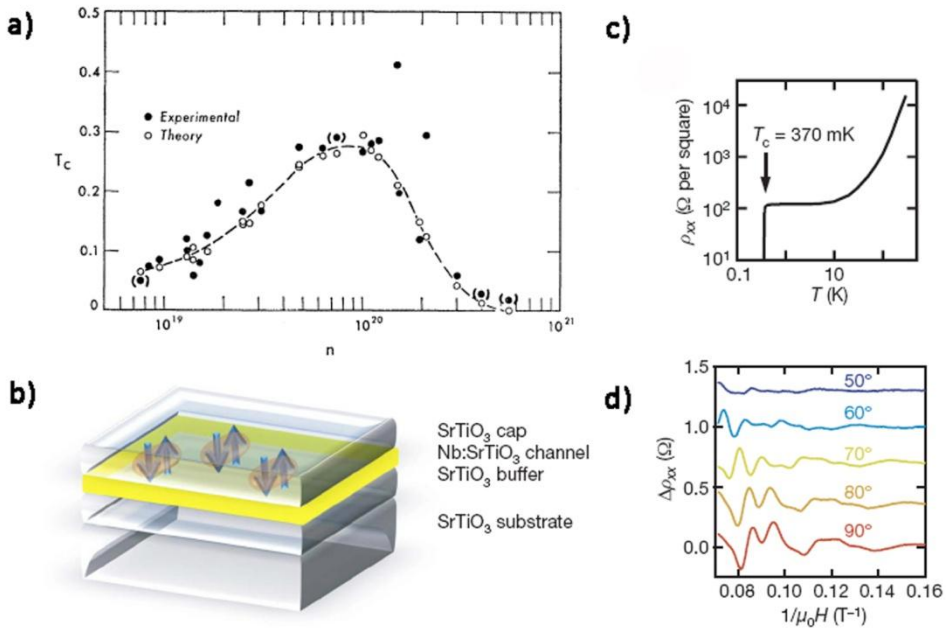

Figure 1.6 (a) Transition temperature as a function of carrier concentration of superconducting $SrTiO_3$ single crystals; (b) A sketch of the delta-doped NSTO layer sandwiched between insulating STO buffer and cap layers on an STO substrate; (c) Sheet resistance of the sandwiched sample versus temperature showing a clear superconducting transition at 370 mK; (d) Amplitude of the Shubnikov-de Haas oscillations after background subtraction versus the reciprocal total magnetic field at T = 100 mK. [(a) is adopted from Ref. [50] and (b) (c) (d) are all adopted from Ref. [54]]

Other transport properties of doped-$SrTiO_3$ under magnetic fields, such as

charge carrier mobility adopted from Hall measurements have also been studied in details [55]. These not only provide information that doped-$SrTiO_3$, especially the La- or Nb-$SrTiO_3$, can exhibit very high mobility (Fig. 1.7), but also help to unveil some fundamental questions on conducting or scattering mechanisms of $SrTiO_3$. Besides, magnetoresistance of semiconducting $SrTiO_3$ have been intensively investigated since 1960s [56]. All these established results and methods light up the road to explore new phenomena and physics emerging at perovskite oxide interface, which is the focus of this work.

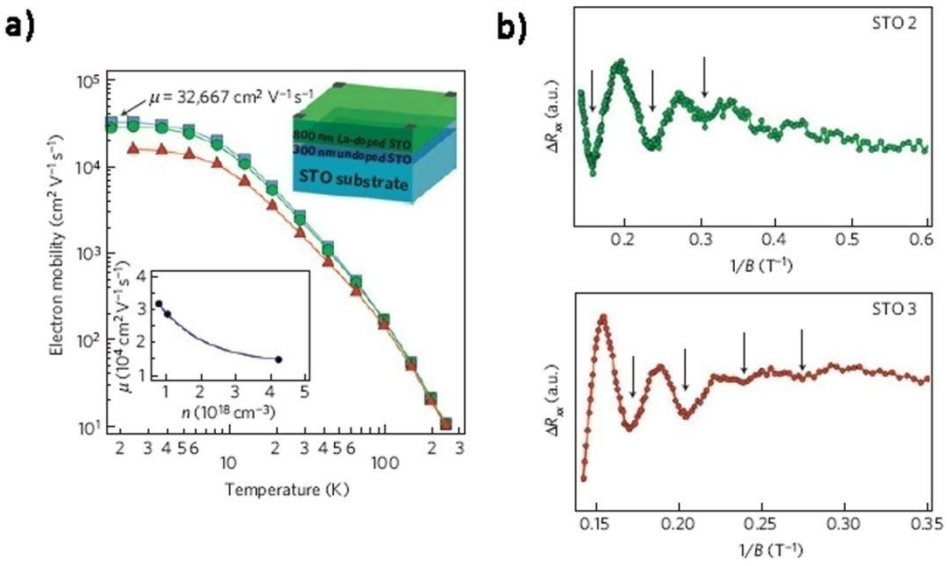

Figure 1.7 (a) Hall electron mobility as a function of temperature for three samples with the structure shown in the upper inset; and (b) Shubnikov-de Haas oscillations in homoepitaxial $SrTiO_3$ thin films. (Adopted from Ref. [55])

1.4 Two-Dimensional Electron Gases (2DEG) in Semiconductors

A two-dimensional electron gas (2DEG) is a gas of electrons which is free to move in two dimensions, but tightly confined in the third. Such 2DEG systems, mainly due to boundary condition confinement in the third direction, behave many useful and interesting properties, as well as allow access to interesting physics. Up to now, experimental observations of physical properties of 2DEG, predicted by

theoretical derivations, have been massively reported in some model 2DEG structures [2, 57-58] and boosted up the comprehension on this system. For example, the Quantum Hall Effect (QHE) was first observed in a 2DEG [59], which led to two Nobel Prizes, in 1985 and 1998. Besides, the strongly prospective properties for applications have driven the motivation for building up future high electron mobility transistors (HEMTs).

Practically, 2DEG can be found in commercialized MOSFETs, which is made from semiconductors combined with gate oxide and metal electrodes, operating in inversion mode [Fig. 1.8(a)]. The electrons underneath the gate oxide are confined to the semiconductor-oxide interface, and thus occupy well defined energy levels. Nearly always, only the lowest energy level is occupied, and so the motion of the electrons perpendicular to the interface can be ignored. However, the electrons are free to move near and parallel to the interface, and so it is quasi-two-dimensional.

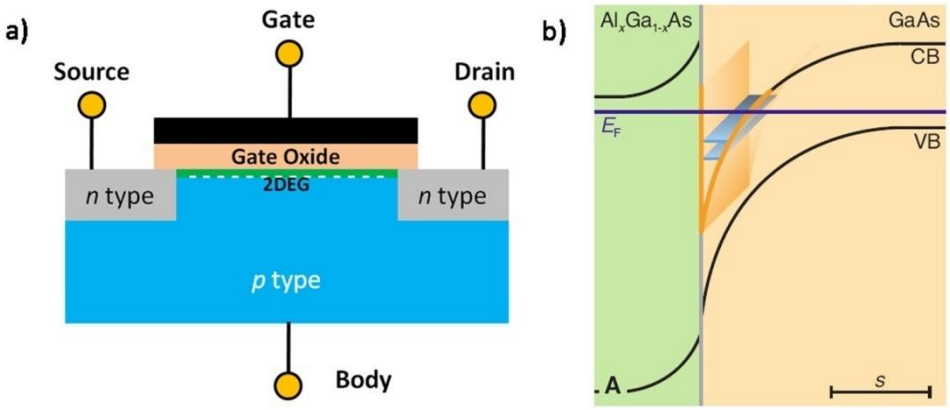

Figure 1.8 (a) Schematic diagram of a MOSFET in which the 2DEG is present only when the transistor is in inversion mode; (b) Illustration of the configuration of two-dimensional electron systems in standard semiconductor interfaces (figure adopted from Ref. [60]).

In advanced research, most studied 2DEG systems are constructed at semiconductor heterojunctions between different materials or materials with different doping levels, such as model systems like $Mg_xZn_{1-x}O/ZnO$ and $Al_xGa_{1-x}As/GaAs$. In

these systems, electrons accumulated at the heterointerfaces are well confined in a triangular quantum well and the mobility of the carriers can be very high. The electrons are created at the highly doped side of the heterojunction, then "drop off" to the quantum well that has a lower potential at the interfaces formed by the band bending, which is due to the adjustment of Fermi levels between the two different materials. As shown in the electronic band diagram of $Al_xGa_{1-x}As/GaAs$ heterostructure in Fig. 1.8(b), the electrons inside the well can "travel" more freely in a channel lying at the intentionally undoped side by minimizing the "poisoned" scattering effect by ionized impurities,. This leads to higher mobility compared to those in MOSFETs.

With this important feature, by carefully tuning the carrier concentrations, QHE and Shubnikov-de Haas (SdH) oscillation can be observed (Fig. 1.9). More specifically, $Al_xGa_{1-x}As/GaAs$ heterostructures are reported to be combined with a carbon nanotube to function as a highly sensitive terahertz detector [61] and with a probe-integrated gate electrode to function as a scanning nanoelectrometer [62].

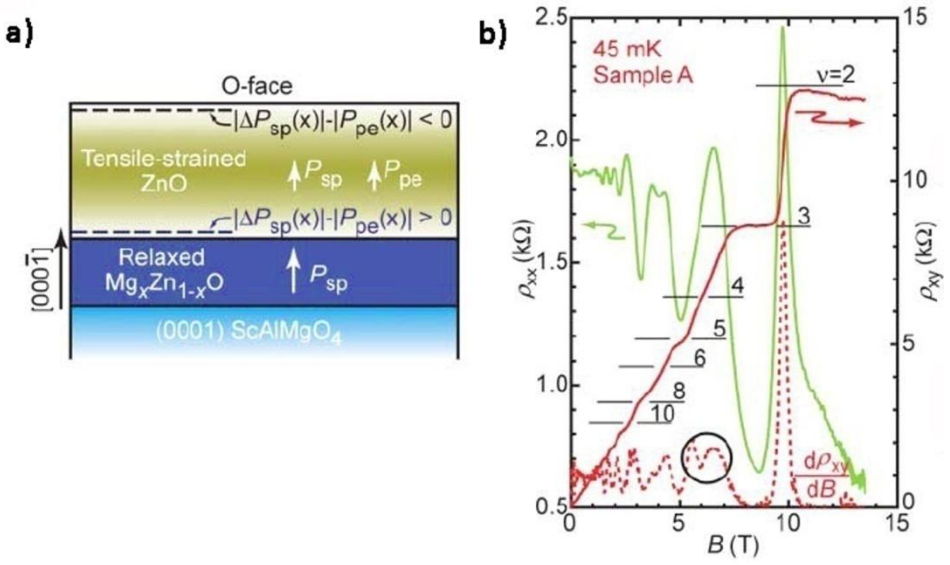

Figure 1.9 (a) Schematic of the $ZnO/Mg_xZn_{1-x}O$ heterostructures grown on $ScMgAlO_4$ substrates; (b) Longitudinal resistivity ρ_{xx}, Hall resistivity ρ_{xy}, and differential Hall resistivity $d\rho_{xy}/dB$ versus B measured at 45 mK for the corresponding

sample, in which integers on the horizontal tick marks are the Landau level filling factors defined as $\nu = h/(\rho_{xy}/e^2)$. (Adopted from Ref. [2])

1.5 $LaAlO_3/SrTiO_3$ Heterointerfaces

As discussed at the beginning of the thesis, the introduction of interfaces within semiconductor heterostructures has produced a large amount of semiconductor devices of giant utility and fascinating physics. Similarly, it is also charming and straight forward to incorporate high-quality interfaces into oxide heterostructures to obtain novel properties. However, because oxide heterostructures and multilayers are far more difficult to fabricate than conventional semiconductor ones, progress made in this field was limited for many years. Over last two decades, the growth of oxide heterostructures and multilayers are well developed, benefiting from large advances in growth techniques and characterization methods, including the application of high vacuum pulsed-laser deposition (PLD) [63], molecular-beam epitaxy (MBE) [64], the ability of obtaining well-defined terminations of substrates [65], and the development of high-pressure reflection high-energy electron diffractions (RHEED) [66]. As a result, epitaxial heterostructures of oxides can be well fabricated with atomic scale precision. Thus, the ability to precisely control interfaces between different oxide materials provides new opportunities to create new electronic phases. Among them, a model system is that heterointerfaces between perovskite transition metal oxides emerge as one of the focused topics in condensed matter physics. In the building blocks of this area, one can take a deep insight of strongly correlated electrons systems to explore some fundamental physical bulk properties similar to those in conventional semiconductor heterostructures. More excitingly, there is more freedom to build a large number of combinations of different materials with different functionalities, thus produce plenty categories of interfaces where novel physical properties, that are absent in their bulk components, may arise.

Triggered by the work of Ohtomo and Hwang from Bell Laboratory in 2004 [6], a perovskite oxide heterointerface $LaAlO_3/SrTiO_3$ (LAO/STO) becomes a hot topic in

recent years. A conducting layer with quasi-two-dimensional electron gas (q2-DEG) can be formed when these two insulators join together. Many interesting phenomena have been observed in this LAO/STO interface since 2004, including superconductivity [67] and indications of magnetism [68]. Electronic phase diagram of the system was also depicted by tuning interfacial states using field effect [51]. Besides, more and more physical phenomena have been observed, predicted and discussed in both experimental [51, 67-73] and theoretical [74-77] work, revealing that such q2-DEG holds many similarities with the parallel systems in semiconductors. However, the debate on the origin of the conductivity and high mobility [73, 75, 78-81] together with the more complex electronic phase diagram has somehow indicated the fundamentally extraordinary extra properties and complexity in such a 2D system. And these bring huge interest on this novel system.

1.5.1 Properties of $LaAlO_3$

$LaAlO_3$ is the "second floor" of the building of this LAO/STO heterostructure. Thus before entering the q2-DEG at LAO/STO interfaces, we should have a general knowledge about this material.

At high temperatures, $LaAlO_3$ has a cubic perovskite structure with space group $Pm\bar{3}m$, but under a transition temperature, it undergoes a phase transition to a rhombohedral structure which is a distorted perovskite (space group $R\bar{3}c$) [82]. Usually at room temperature, the structure of $LaAlO_3$ can be described as a pseudocubic structure with a lattice parameter of 3.791 Å, which is slightly differed from cubic perovskite by small rotation of AlO_6 octahedra, [83]. Just like $SrTiO_3$, $LaAlO_3$ holds a good mismatch with many perovskite oxide materials so that it is also popularly used as substrate material; and due to the reasonable lattice mismatch with $SrTiO_3$ (about 3%), the epitaxial growth of $LaAlO_3$ films on $SrTiO_3$ can be realized.

$LaAlO_3$ is also a band insulator with a wide band gap of 5.6 eV. Because of its insulating behavior and relatively high dielectric constant (about 25 at room

temperature and low temperatures [84, 85]), it is usually used as a high-*k* gate oxide material [86].

1.5.2 Electronic Reconstruction at $LaAlO_3/SrTiO_3$ Interfaces

Since the conductivity of the LAO/STO interface was quite surprising, the origin of this conducting q2-DEG was under intensive discussion both theoretically and experimentally. In Ohtomo and Hwang's paper [6], they traced the fundamental mechanism by preparing two different stackings using pulsed-laser deposition to grow $LaAlO_3$ on top of $SrTiO_3$ substrate along [001] direction. Because for this direction, perovskite oxides (ABO_3) can be described as sequence of alternating AO and BO_2 atomic layers, apparently, two kinds of interfaces can be formed between $LaAlO_3$ and $SrTiO_3$, as shown in Fig. 1.10.

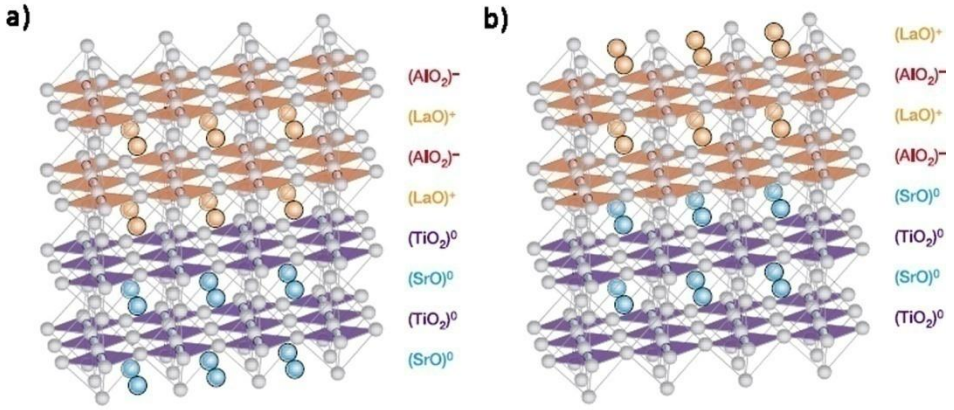

Figure 1.10 Schematic of the resulting $(LaO)^+/(TiO_2)^0$ interface (a), and $(AlO_2)^-/(SrO)^0$ interface (b). (Adopted from Ref. [6])

In Fig. 1.10(a), $LaAlO_3$ was epitaxially grown on a TiO_2 terminated (001) $SrTiO_3$ single crystal substrate and interface of TiO_2/LaO was established; while in Fig. 1.10(b), interface of SrO/AlO_2 was established by inserting a monolayer of SrO on top of the original substrate. It was shown in Ref. [6] that the electronic transport properties of these two kinds of interfaces between $LaAlO_3$ and $SrTiO_3$ are dramatically different, where one setup (TiO_2/LaO stacking) is highly conducting and

the other (SrO/AlO_2 stacking) is insulating. Due to the different valence states of the cations (La^{3+}, Al^{3+}, Sr^{2+}, Ti^{4+}), $LaAlO_3$ can be described as alternating sheets of $(LaO)^+$ and $(AlO_2)^-$, which are both charged planes; while $SrTiO_3$ is composed of a sequence of charge neutral layers of $(SrO)^0$ and $(TiO_2)^0$. Therefore, a polar discontinuity is formed at the interface when these two materials join together, and due to the sequence of charged planes, a potential build-up can be established within $LaAlO_3$ layer (see Fig. 1.11). This polar discontinuity has a name of "polar catastrophe", and in fact, such a discontinuity was firstly discussed in 1980s for semiconductor Ge/GeAs heterostructures [87].

For semiconductor heterostructures formed by charged layer and charge neutral layer, systems can avoid such a "polar catastrophe" by redistributing the atoms at the interfaces, known as atomic reconstruction, which will lead to interface roughness; but this is the only option because typical semiconductor cations have a fixed valence. However, for complex oxides formed heterointerface, such as LAO/STO, some cations have mixed valences available which allow for charge compensation by accommodating extra electrons in their bands. At TiO_2/LaO interface in LAO/STO heterojunctions, electrons can cross the interface to locate at interfacial Ti ions' conduction bands leading to an *n*-type interface (electron doped). This causes Ti ions to become Ti^{3+}, thus eliminates the divergence of the electrostatic potential within $LaAlO_3$ layer (see Fig. 1.11); while the actual potential oscillates around a finite value. Therefore the fundamental mechanism underlying this new phenomenon was proposed to be electronic reconstruction at the beginning.

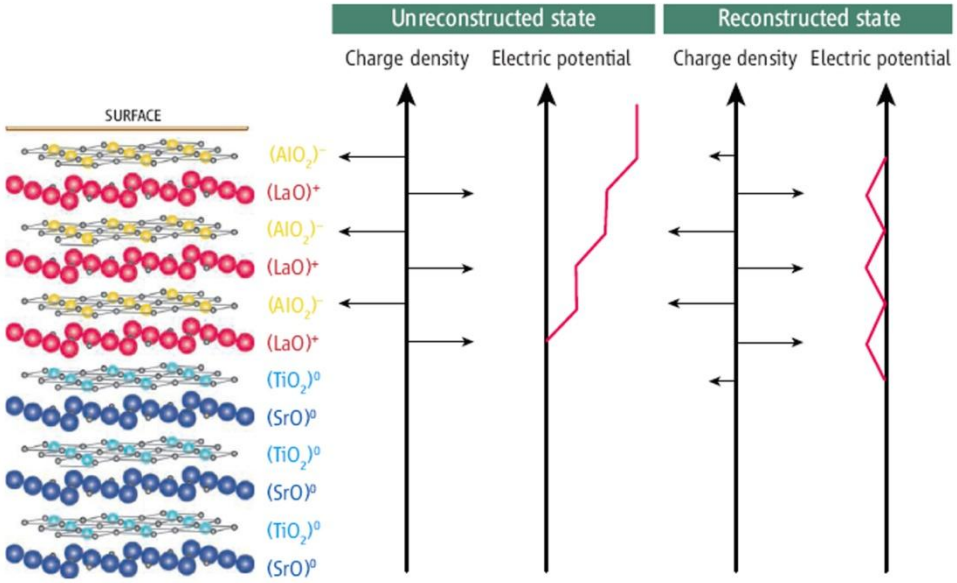

Figure 1.11 Schematic of the polar discontinuity. (Left) The unreconstructed interface. (Middle) This charge configuration leads to an electric potential that diverges with $LaAlO_3$ thickness. (Right) Above a threshold thickness, the charge distribution reconstructs, removing the divergence. This is shown as a layer of $Ti^{3.5+}$ at the interface, and a simple reconstruction of the polar surface of $LaAlO_3$. (Figure from Ref. [88])

The electronic reconstruction picture seemingly provided a good interpretation on the origin of the metallic interfaces at LAO/STO heterostructures. However, quite soon it became clear that this picture should be extended by including other possibilities because some experimental results cannot be rationalized only using polar discontinuity model. For example, the insulating behavior of the *p*-type interfaces (built from SrO/AlO_2 interfaces) observed was not reconciled in this approach. Among them, the structural aspects should also be considered, such as formation of an ultra-thin conducting sheet built by interdiffusion, formation of defects from oxygen vacancies localized at interfaces, as well as the important role of $SrTiO_3$. Nevertheless, the origin of the q2-DEG is still under debate and more calculations and experiments need to be done in this field. But the discussion will not be depicted in details in this chapter and the introduction of this electronic reconstruction scenario is proposed in order to take a glance at the mechanism

underlying and try to shed light on understanding of the origin of this buried q2-DEG.

1.5.3 Transports of $LaAlO_3/SrTiO_3$ Interfaces

The $LaAlO_3$ thickness dependence of the conductivity of the LAO/STO interfaces were thoroughly investigated by Thiel et al. [89] who grew $LaAlO_3$ films with different thicknesses on TiO_2 terminated (001) $SrTiO_3$ single crystal substrates. An insulator-to-metal transition was found when the thickness of $LaAlO_3$ layer equals 4 unit cells or above. This abrupt transition was characterized by the increase of several orders of magnitude in conductivity, showing a "step" in sheet conductance diagram as a function of $LaAlO_3$ layer thickness. This discovery reconciled the polar discontinuity model as the thickness of $LaAlO_3$ layer has to be over a critical thickness so that the built-up potential in $LaAlO_3$ is large enough to drive electrons across the interface making the interface conducting. But they also found that the carrier concentration determined from Hall measurements are far less than the value expected from the polar discontinuity model, which is about 3.3×10^{14} calculated by assuming 0.5 electrons per 2D unit cell. So far, the reason for this large discrepancy remains an open question.

After this feature of the q2-DEG was revealed, other transport properties were also reported. 2D Superconductivity was observed with transition temperature of about 100 mK ~ 200 mK by Reyren et al. in 2007 [67], as shown in Fig. 1.12(a). The transition into superconducting state was conceivably interpreted as a Berezinskii-Kosterlitz-Thouless (BKT) transition from the current-voltage relation and temperature-dependent sheet resistance. Since the transition temperature falls into the range of superconducting transition temperature for reduced $SrTiO_3$, the mechanism for the superconductivity of LAO/STO interface is not clear. The question that whether this superconducting is due to a superconducting sheet of typical $SrTiO_{3-\delta}$ or the cooper pairs in q2-DEG induced by $SrTiO_3$ is still open. But a sheet carrier density over 5×10^{14} is needed to provide such transition temperature (3D carrier density about 3×10^{19}) according to the calculation by only considering

$SrTiO_{3-\delta}$ scenario, therefore, it was claimed that the 2D conductivity cannot be solely attributed to oxygen vacancies.

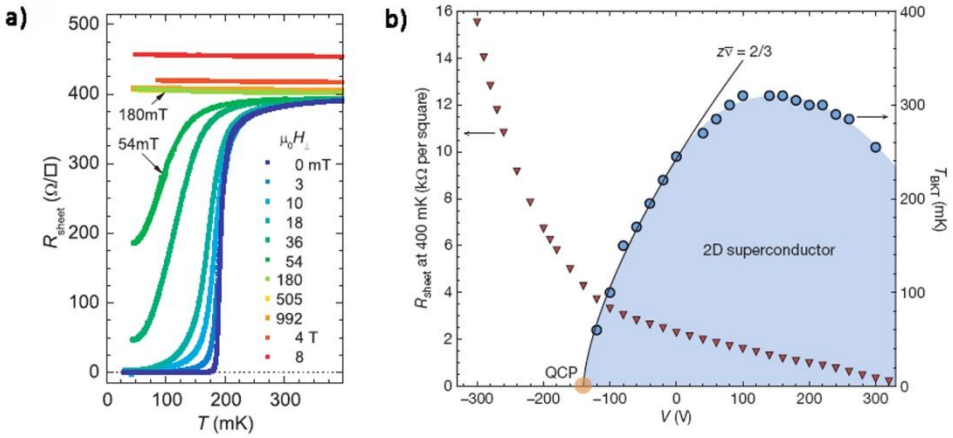

Figure 1.12 (a) Sheet resistance of the 8-uc LAO/STO sample plotted as a function of *T* for magnetic fields applied perpendicular to the interface revealing obvious superconducting behavior (adopted from Ref. [67]); (b) Electronic phase diagram of the LAO/STO interface (adopted from Ref. [51]).

Two years later, it was further shown that by using electric field effect the ground state of the LAO/STO interface system can be tuned between insulating and superconducting and the electronic phase diagram was successfully mapped [51], as illustrated in Fig. 1.12(b). This phase diagram provided plenty of characterized information on this system and also raised some interesting questions that need to be explored and answered. Based on this phase diagram, large tunable spin-orbit interaction was found [72, 90]. Besides, negative magnetoresistance in some circumstances [68], anisotropy of superconductivity [91] and anisotropy of magnetoresistance [92] were also displayed. Recently, quantum oscillation has also been observed. All these transports indicate a complex and abundant physics in such a system.

1.5.4 Applications of $LaAlO_3/SrTiO_3$ Interfaces

As mentioned in 1.5.3, the $LaAlO_3$ thickness dependence of the conductivity and

the abrupt jump in sheet conductance offer an opportunity to tune the resistance of the interface system in order to realize memory behavior. In Fig. 1.13(a), it was shown that by using a back gate voltage, a resistance switching memory function can be performed on 3 u.c. LAO/STO sample [89].

This thickness dependent conductivity also provides a new technique to pattern the interface [69, 93-95]. Using microlithography and conventional lift-off process, conducting nanostructures can be patterned by growing 6 u.c. $LaAlO_3$ in the conducting region and 2 u.c. $LaAlO_3$ in the region to be insulating [Fig. 1.13(b)]. Besides, writing and erasing conducting lines and structures with a resolution of nanometers to realize different functions at the interfaces by applying a voltage to the conductive AFM tip were also achieved [Fig. 1.13(c)]. At this point, novel conducting LAO/STO interfaces opens a new route for the promising applications in the oxide nanoelectronic platform.

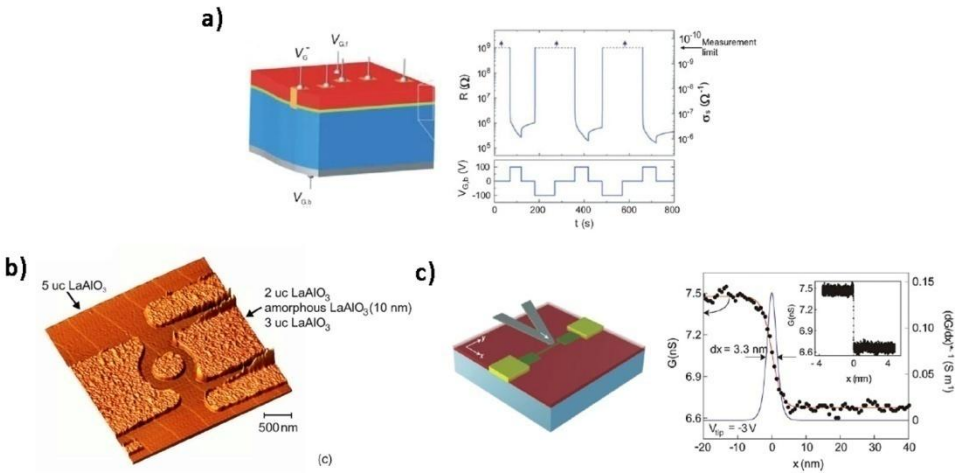

Figure 1.13 Device structures based on LAO/STO heterostructures. (a) Memory behavior: sheet resistance measured at 300 K and under applied back gate voltage, both plotted as a function of time for a $LaAlO_3$ layer with a thickness of 3 unit cells (figure adopted from Ref. [89]); (b) AFM image of a ring defining a q2-DEG fabricated through e-beam lithography (figure adopted from Ref. [93]); (c) Writing and erasing nanowires utilizing a C-AFM: conductance between the two electrodes measured as a function of the tip position across the wire (figure adopted from Ref.

[94]).

1.6 Motivations of the Project

From the literature review and overlook of what has been done on LAO/STO heterointerfaces since 2004 [6], it can be noticed that it is the theoretical and experimental interest, as well as application perspectives, that draw scientists' attention on this conducting oxide heterostructures. Many efforts have been exploited to investigate the origin of the q2-DEG and try to overcome the obstacles towards making applicable devices. However, as stated in Ref. [79], there are still many open questions regarding the mechanism for the appearance of this q2-DEG. For instance, to date, all analogues of the LAO/STO system with conducting electron gases involve STO, why? What's the function of STO in the loop? What should be responsible for the superconductivity of the LAO/STO interface? Finally, why there is no demonstration of multilayered 2DEGs?

To answer these questions, we must perform some experiments to touch the fundamental problems of the phenomena. For example, we need to figure out whether the electron gas will preserve when different material combinations are exerted, especially the role of STO. These experiments may reveal the origin of the q2-DEG gas and open new routes for other oxide interfaces and interface engineering. In this project, I followed two approaches to tackle these problems:

[1] Instead of investigating deeply to the physics behind LAO/STO interfaces, it would be worthy to fabricate other heterointerfaces using another insulating perovskite which has the same polar atomic planes as $LaAlO_3$ on top of $SrTiO_3$. By comparing with LAO/STO system, we may find some new phenomena that help to understand the oxide interfaces.

[2] Building LAO/STO interfaces on STO thin films rather than single crystal STO is another effective way to study the function of STO on generating the electron

gas. Based on this idea, we can grow STO thin films on different substrates at different growth temperatures and build LAO/STO heterointerfaces on this artificial STO layer and analyze the differences in transport properties.

1.7 Outline of the Thesis

A brief literature review is given in this chapter (Chapter 1), including an introduction to perovskite oxides, structure and transport of $SrTiO_3$, an overview of 2DEG in conventional semiconductors and finally a short summary of the reported work in novel LAO/STO interfaces.

Chapter 2 gives a short introduction to the main techniques that have been employed in this study including substrate treatment, deposition techniques, structural characterization techniques and transport measurement setups.

In Chapter 3, we chose a "polar" perovskite Dysprosium Scandate ($DyScO_3$) instead of $LaAlO_3$, and try to explore the effect of the growth conditions on the electronic properties. This chapter focuses on the fabrication of $DyScO_3/SrTiO_3$ heterostructures by Laser-MBE, and by utilizing structural characterization techniques, Hall measurements and field effect measurements, the relations between deposition condition, structural and electronic properties of the heterointerfaces have been investigated.

In order to deeply understand the role of $SrTiO_3$ in generating the q2-DEG in LAO/STO heterointerfaces, Chapter 4 focuses on the fabrication of LAO/STO/STO structures by firstly growing an artificial $SrTiO_3$ layer on top of $SrTiO_3$ single crystal. Structural, transport and dielectric characterizations were carried out to demonstrate the importance of $SrTiO_3$.

Chapter 5 gives the conclusion of this thesis and the future prospects.

CHAPTER 2

FABRICATION AND CHARACTERIZATION METHODS OF THE HETEROINTERFACES

The fabrication of the heterointerfaces and study of their transport properties include a number of experimental techniques and methods, which can be mainly categorized into five groups:

I Substrate termination control: by using buffered hydrofluoric acid (BHF) and oxygen ambient annealing process.

II Thin-film deposition: pulsed-laser deposition (PLD) and laser-molecular beam epitaxy (Laser-MBE).

III Structural characterizations: reflection high-energy electrons diffraction (RHEED), X-rays diffraction (XRD), atomic force microscopy (AFM), transmission electrons microscopy (TEM) and photoluminescence spectrum (PL).

IV Electrodes deposition and patterning: magnetron sputtering and pulsed-laser deposition for electrodes deposition; dry-etching using Ar^+ plasma and lift-off process for electrodes patterning.

V Transport measurements: Hall effect measurement setup, magnetoresistance measurement setup facilitated with superconducting magnet and cryogenic systems; dielectric tests by impedance analyzer.

This chapter gives an introduction to these techniques and the theories behind

these methods will also be discussed.

2.1 Substrate Treatments

In advanced research field of oxide heterostructures and interfaces, perovskite substrates of atomically flat surface with single termination became a crucial prerequisite for growing high quality oxide interfaces. Thus, the preparation techniques of single-terminated perovskite substrates underwent a great development [65, 96]. $SrTiO_3$ is a good example for this. As described in Chapter 1, $SrTiO_3$ has a cubic perovskite structure which consists of SrO and TiO_2 atomic planes. Therefore $SrTiO_3$ has two possible terminations, i.e., SrO termination and TiO_2 termination. Usually, as-received commercial polished $SrTiO_3$ substrates have mixed terminations. Basically, if one can find a way to remove one of the atomic layers but not the other one, an atomically smooth single terminated surface can be obtained, and steps with a single unit-cell height can be observed at the surface [Fig 2.1(a)]. In 1994, M. Kawasaki et al. [65] in their *science* paper introduced an effective method to obtain single TiO_2-terminated $SrTiO_3$ substrates by dissolving SrO on the surface using a pH-controlled NH_4-HF solution, named as buffered HF solution (BHF). Since SrO is a basic oxide and TiO_2 is an acidic oxide, by tuning the pH value of the buffered solution, one should be able to use this wet etching process to remove the residual Sr on the surface. After such an etching, step-and-terrace structure can be obtained, as shown in Fig. 2.1(b), with step height of ~0.4 nm which corresponds to the lattice constant of $SrTiO_3$ (a = 3.905 Å). This indicates that the steps are exactly single-unit-cell high.

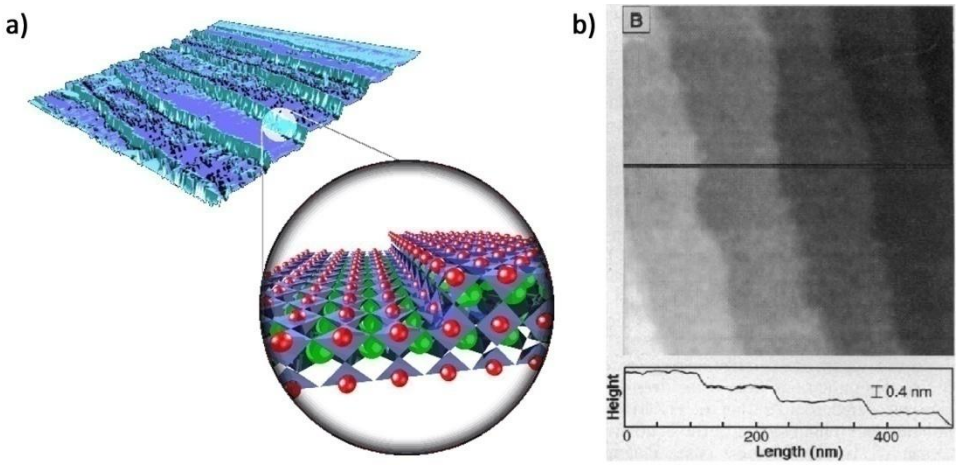

Figure 2.1 (a) Schematic sketch of $SrTiO_3$ single crystal surface with single termination; (b) AFM image of a TiO_2-terminated surface of $SrTiO_3$ substrate showing well-defined step-and-terrace structure with step height of 0.4 nm, which corresponds to a single unit cell (adopted from Ref. [65]).

As shown in the model in Fig 2.2(a), the BHF etching can dissolve Sr more efficiently than Ti, where the etchant mostly "attacks" the Sr site at the step edges, dissolving it and then removing Ti by lift-off procedure [96]. In this etching, pH value was found to be very crucial to the surface quality. Numerous etching pits will appear if the pH value is too low, while remnants remain on the surface if the pH value is too high. This often introduces unit cell deep holes in the terraces and even deep etches pits, which will hinder thin film growth. Hence, the reproducibility depends severely on the pH value and the differences in polishing before the BHF etching step.

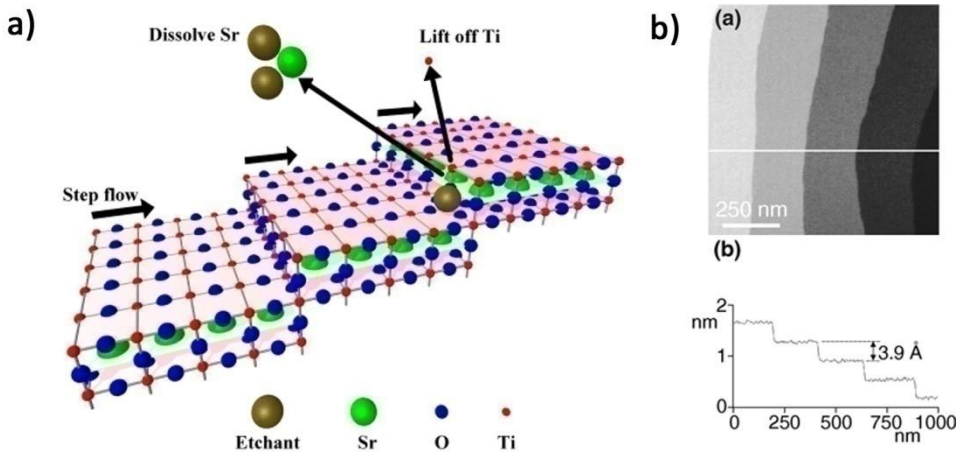

Figure 2.2 (a) Sketch showing the etching process: the etchant removes Sr more efficiently than Ti by mostly attacking the Sr at the step edges, dissolving it and then removing Ti by lift-off; (b) AFM micrograph of a nearly perfect and atomically flat surface, obtained by using the method stated in Ref. [96] (image from the same reference).

It was soon found out [96] that by inserting a step of soaking the $SrTiO_3$ substrates in deionized water prior to BHF etching, nearly perfect surfaces can be obtained. Water can firstly help SrO to form a Sr-hydroxide complex confined at the topmost layer, which can then be easily dissolved in acid. This extra process separates the whole etching process into two steps, thus enhances the selectivity in solubility of Sr and Ti, making the pH value of the BHF solution become much less crucial and less etching time is needed. The possibility of reducing the etching time prevents formation of etched pits and holes. It was also reported that after the BHF etching, an annealing for the substrates in oxygen at high temperature above 850 ℃ can remove residuals and help recrystallization. Finally, a quasi-ideal surface with well defined step-and-terrace structures, as well as straight edge lines, is revealed [Fig. 2.2(b)].

Other means such as re-etching steps [97, 98] and using HCLNO ($HCL:HNO_3$ = 3:1) [99, 100] were also reported. A large number of characterizations were implemented illustrating the TiO_2 termination nature of such surfaces [97-100]. Such research is still undergoing, but in this work, we only use the standard procedures described above to obtain TiO_2 terminated $SrTiO_3$ single crystal substrates.

2.2 Thin Film Deposition

In this study, in order to fabricate high quality epitaxial heterointerfaces, pulsed-laser deposition technique was used to grow perovskite oxide thin films. Pulsed-laser deposition technique is one of the physical vapor deposition techniques, which has big advantages over competing techniques including: (1) a large variety of materials can be ablated; (2) the growth rate can be well controlled; (3) growing in

different ambient gases can be realized; and (4) the stoichiometry of the thin films can be preserved from the target materials even for the complex oxides, if the growth parameters are optimized. But disadvantages of such "effective" technique are also clear: small deposition area, space distribution effect, large costs, higher growth temperatures and low production, all of which make pulsed-laser deposition technique only suitable for laboratory research but limit its application in industries.

Pulsed-laser deposition is a very simple yet useful technique often used for growing oxides, nitrides and other materials as well as nanostructures [101]. Its large development in fabrication of complex oxide thin films was stimulated by the study and growth of perovskite-type high-T_c superconductors [66, 102]. By adjusting the growth parameters, even the cuprate superconductors which have long *c*-axis and relatively complex lattice structures can be epitaxially grown on different perovskite substrates. While in semiconductor technologies, another powerful deposition technique, molecular beam epitaxy (MBE), combining an ultra-high vacuum chamber, load-lock chamber and some surface characterization techniques such as reflection high-energy electrons diffraction (RHEED), enables to grow atomic-level controlled surfaces, interfaces and superlattices of semiconductor heterostructures. But even in today, MBE still remains not a simple technique easy to handle. By taking advantages of these two techniques, people attempted to develop new technology combing MBE and PLD together [103] by "arming" traditional PLDs with ultra-high vacuum techniques using complex pumping systems and especially RHEED system to in-situ monitor the growth process in PLD. This is thus called laser-molecular beam epitaxy (Laser-MBE) or ultra-high vacuum PLD. The large development in high-vacuum PLD has provided the opportunities to manipulate oxide heterostructures, just as in semiconductors, and already produced fruitful fascinating output in oxides during past decades. In this study, we use Laser-MBE to fabricate high quality perovskite heterointerfaces and this is the first key prerequisite for investigating the interface phenomena.

A schematic diagram of working principles of the Laser-MBE systems is shown

in Fig. 2.3(a). Figure 2.3(b) shows a photograph of the Laser-MBE system used in our lab. From the picture, we can see that the Laser-MBE includes these basic components: (1) Ultra-high vacuum chamber (main chamber) for deposition of thin films; (2) load-lock chamber for samples in-and-out without breaking the vacuum in main chamber; (3) RHEED system; (4) target rotating system; (5) substrate holder and heating system.

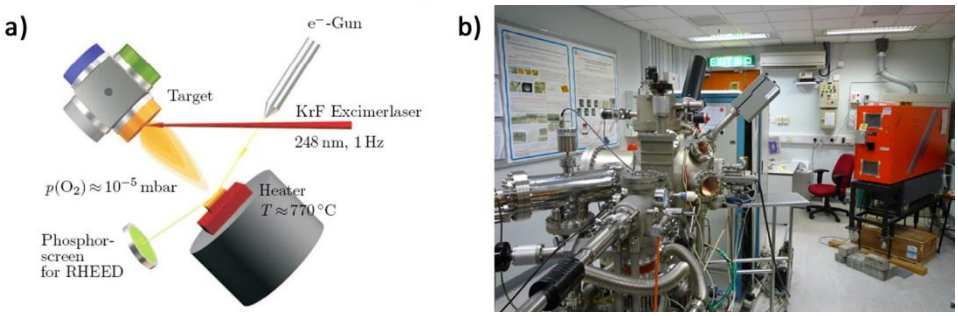

Figure 2.3 (a) Sketch of deposition principle of Laser-MBE, showing some example deposition parameters in the picture (sketch from Ref. [104]); (b) Photo of the Laser-MBE with attached RHEED system and excimer laser in our lab.

2.3 Structural Characterizations

2.3.1 Reflection High-Energy Electron Diffraction (RHEED)

RHEED is a versatile technique which utilizes diffraction of electrons by surface atoms thus can provide information of the periodic arrangement of the surface atoms. Due to the compatibility with the ultra high vacuum chambers and techniques, it is widely used as a powerful in-situ tool to monitor the film growth. But before the introduction of basic geometry of RHEED, some preliminary thermodynamic knowledge of film growth mode should be mentioned here. Especially, the work of this thesis relies on smooth film surfaces and interfaces. Therefore, understanding of the different mechanisms affecting the growth mode is necessary for controlling the surface morphology and interfaces quality.

Four different growth modes are distinguished shown in Fig. 2.4, depending on the free energies of the substrate surface (γ_S), film surface (γ_F), and film-substrate interface (γ_I). Significant wetting will appear if $\gamma_F+\gamma_I<\gamma_S$ (strong bonding between the film and the substrate). In this situation, 2D layer-by-layer growth (Frank-Van der Merwe growth) [105] occurs. On the other hand, if bonding between substrate and film is weak, separated 3D islands will grow and finally coalesce (Volmer-Weber growth) [106]. When the lattice mismatch between the substrate and the film gives rise to biaxial strain, resulting in an elastic energy increasing with increasing layer thickness, Stranski-Krastanov growth will appear [107]. This growth mode describes the intermediate case when strong substrate-film interactions at first lead to some complete monolayers, followed by appearance of islands. Another important growth mode (step-flow) is found if the diffusion time (relaxation time) of adatoms is shorter than the laser rest time. The adatoms move to the step edges and nucleation on a terrace is prevented. No island growth is observed in this case. This growth mode is the main subject of Chapter 4 and will be discussed more in details then.

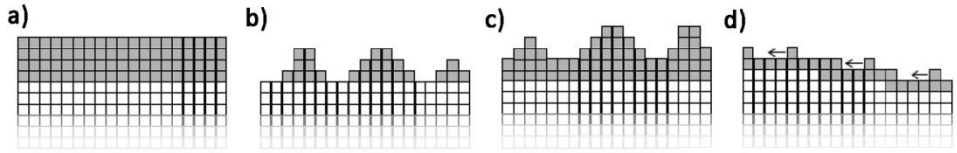

Figure 2.4 Sketch of different film growth modes: (a) Frank-Van der Merwe, or layer-by-layer; (b) Volmer-Weber; (c) Stranski-Krastanov; (d) step-flow growth modes.

A typical RHEED is composed of an electron gun, a phosphor screen and image detector (CCD camera) and processor. The screen is usually shielded from the laser ablation plume by a metal grid. Generally, double pumping system combined with RHEED maintains the high vacuum environment at the front side and back side of the electron gun which links the main chamber of a Laser-MBE. Complex oxides can be grown under high oxygen pressure (up to 15 Pa) by modifying this double pumping system [66]. This even makes RHEED more functional in oxide thin film fabrication.

RHEED is very surface-sensitive in that it only senses a few top atomic layers of the surface. Because the low incidence angles used in RHEED, experimentally the sensing depth of RHEED is very small. In the construction of the reciprocal lattice we can therefore approximate the sampled volume by a two-dimensional layer. The reciprocal lattice then degenerates into a set of one-dimensional rods along the z direction perpendicular to the sample surface. Using this reciprocal lattice, we get the Ewald sphere construction used in RHEED as shown in Fig. 2.5(a). Since the reciprocal lattice consists of continuous rods, every rod produces a reflection in the diffraction pattern [see Fig. 2.5(b), a typical RHEED pattern of $SrTiO_3$ single-crystal substrate]. The reflections occur on so-called Lane circles of radius L_n centered at H, the projection of the component parallel to the surface of k_0 onto the screen. The specular spot S is located at the intersection of the zeroth-order Laue circle with the (00) rod. The origin of the reciprocal lattice is projected onto I, also labeled (000), where for some sample geometries the part of the incident beam that misses the sample becomes visible. Owing to the simple geometry of RHEED, other spots or patterns generated by other reciprocal rods can be determined. (For a detailed introduction of RHEED working principle, please refer to Ref. [108])

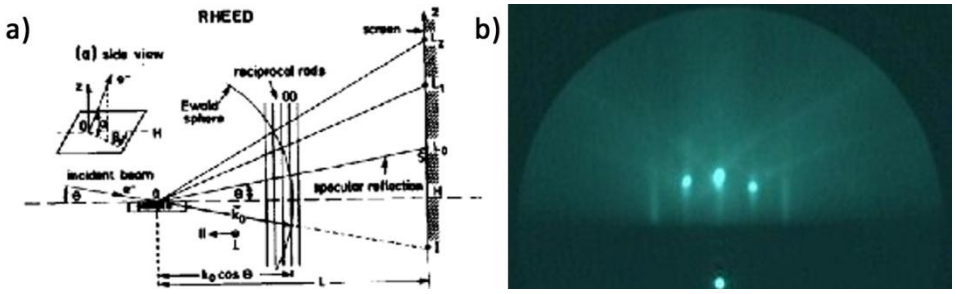

Figure 2.5 (a) Ewald sphere construction and diffraction geometry of RHEED. Intensity maxima on the screen correspond to projected intersections of the Ewald sphere with the reciprocal lattice (adopted from Ref. [108]); (b) RHEED pattern of $SrTiO_3$ substrate at deposition temperature (750 ℃).

For growth mode monitoring, the intensity of the specular reflection is monitored. The intensity of the reflected beam is proportional to the surface

roughness. Smooth surfaces give a high reflected intensity, while rough surfaces don't reflect well and give a lower intensity. Figure 2.6 illustrates evolution of surface roughness and corresponding RHEED intensity.

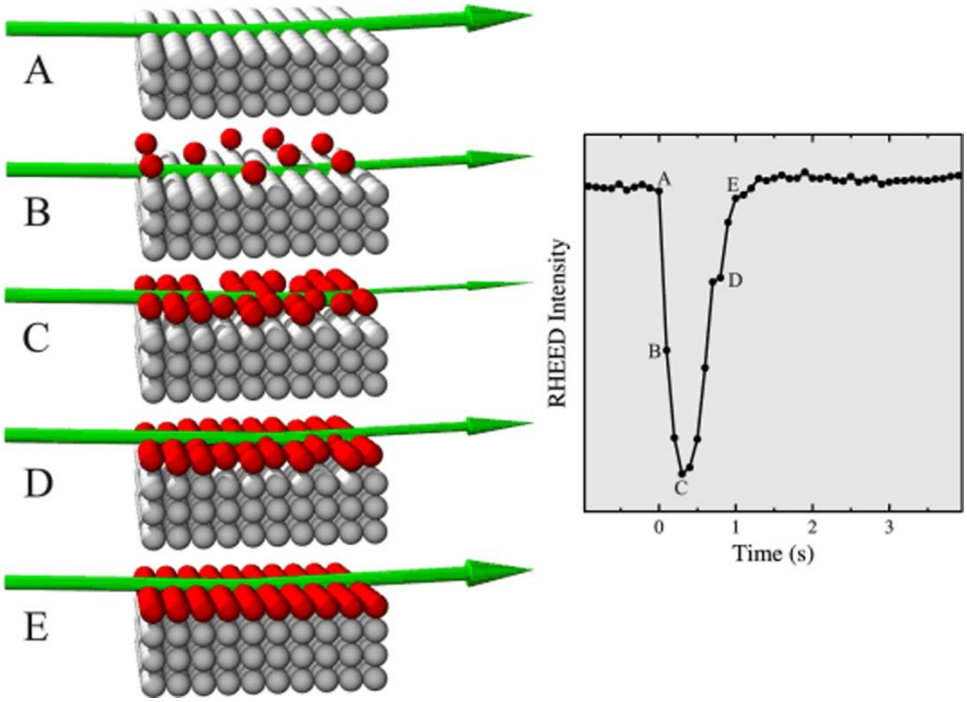

Figure 2.6 Surface models illustrating the growth of a single monolayer of film on a flat surface in layer by layer mode and the graph of measured RHEED intensity during homoepitaxial growth of a single unit cell layer of $SrTiO_3$.

2.3.2 Atomic Force Microscopy (AFM)

Atomic force microscopy (AFM) is a very high-resolution type of scanning probe microscopy (SPM) to collect the surface information, with demonstrated resolution on the order of nanometer. AFM is one of the foremost tools for imaging, measuring, and manipulating matter at the nanoscale. The information is gathered by "feeling" the surface with a mechanical probe. Piezoelectric elements that facilitate tiny but accurate and precise movements on (electronic) command enable the very precise scanning. In some variations, electric potentials can also be scanned using conducting cantilevers. In newer more advanced versions, currents can even be

passed through the tip to probe the electrical conductivity or transport of the underlying surface. Figure 2.7(a) shows the working diagram of a typical AFM.

The AFM consists of a cantilever with a sharp tip at its end which is used to scan the sample surface. When the tip is brought into proximity of a sample surface, forces between the tip and the sample lead to a deflection of the cantilever. Depending on the situation, forces that are measured in AFM include mechanical contact force, van der Waals forces, capillary forces, chemical bonding, electrostatic forces, magnetic forces (for MFM), Casimir forces, solvation forces, etc. Along with the force, additional quantities may simultaneously be measured through the use of specialized types of probe. Typically, the deflection is measured using a laser spot reflected from the top surface of the cantilever into an array of photodiodes. Other methods include optical interferometry, capacitive sensing or piezoresistive AFM cantilevers. Using a Wheatstone bridge, strain in the AFM cantilever due to deflection can be measured, but this method is not as sensitive as laser deflection or interferometry.

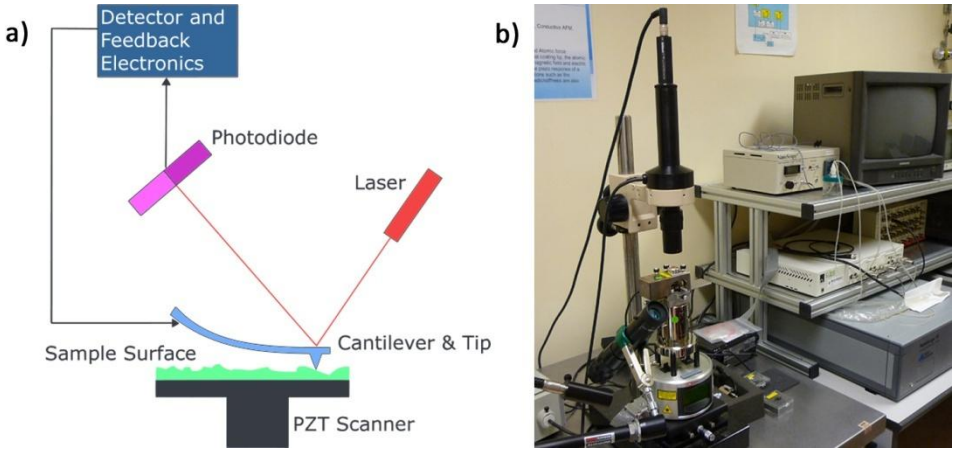

Figure 2.7 (a) Block diagram of working principle of AFM (image from Ref. [109]); (b) AFM facility in our lab.

The AFM can be operated in a number of modes. In general, possible imaging modes are divided into static (also called contact) mode and a variety of dynamic (or non-contact) modes where the cantilever is vibrated. Table 2.1 lists comparison of different modes that often used in AFM.

Table 2.1 Comparison of different AFM working modes (adopted from Ref. [27])

Modes	Advantages	Disadvantages
Contact mode	✓ High scan speeds. ✓ Only technique can obtain "atomic resolution" images. ✓ More easy to scan the sample with extreme changes in vertical topography.	✓ Lateral forces can distort features in the image. ✓ The combination of lateral forces and high normal forces can result in resulted spatial resolution and may damage soft samples
Non-contact mode	✓ No force exerted on the sample surface.	✓ Lower lateral resolution. ✓ Lower scan speed. ✓ Only works on extremely hydrophobic samples.
Tapping mode	✓ Higher lateral resolution. ✓ Lower forces and less damage to soft samples in ambient conditions. ✓ Lateral forces are virtually eliminated, so there is no scraping.	✓ Slow scan speed.

In this project, AFM setup of Veeco digital instrument Ⅳ (di4) in our lab [see Fig. 2.7(b)], and digital instrument Ⅲ (di3) at DPMC in University of Geneva, were facilitated. Moreover, contact mode and tapping mode are mainly used to obtain the topography of the substrates and thin films surfaces.

2.3.3 Transmission Electron Microscopy (TEM)

Transmission Electron Microscopy (TEM) is a powerful microscopic tool to "look into" the structures and micro-structures of materials. TEM uses electrons as a source which has the same function as the lighting source in optical microscopy. The electrons will interact with the matters when transmitting through the ultra-thin specimen, resulting in a variety of beams carrying different information of the matter. These information can be obtained by processing and analyzing the different beam sources and due to the imaging contrast caused by a lot of factors such as mass, crystal orientation, thickness, atomic number, etc., the imaging and diffraction techniques can be categorized as: (1) Conventional imaging including bright-field and dark-field TEM imaging; (2) Selected area electrons diffraction (SAD); (3) Convergent-beam electrons diffraction (CBED); (4) Phase-contrast imaging (high-resolution TEM, HR-TEM); (5) Atomic number contrast imaging (Z-contrast). In this work, the HR-TEM (JEOL JEM-2010 TEM operated at 200kV) equipped with EDX and other functions was utilized.

2.3.4 Photoluminescence Spectrum (PL)

Photoluminescence (PL) is a process in which a substance absorbs photons and then re-radiates photons. Quantum mechanically, this can be described as an excitation to a higher energy state and then a return to a lower energy state accompanied by the emission of a photon. This is one of many forms of luminescence and is distinguished by photo-excitation. The period between absorption and emission is typically extremely short, which is in the order of 10 nanoseconds. Under special circumstances, however, this period can be extended into minutes or hours.

Ultimately, available energy states and allowed transitions between states are determined by the rules of quantum mechanics. A basic understanding of the principles involved can be gained by studying the electron configurations and molecular orbitals of simple atoms and molecules.

2.4 Electrodes Deposition and Patterning

After the samples were fabricated, one problem is how to contact the interfaces to probe the interfacial transport properties. Up to now, several methods have been used in literatures. For example, A. Ohtomo et al. in their first report [6] used laser-annealed ohmic contacts through contact shadow masks to reach the buried interfaces. M. Huijben et al. [110] used wire bonder to contact the samples. A. Kalabukhov et al. [111] used gold pads which were sputtered on a Ti adhesion layer on the samples. In this thesis, to avoid micro cracks and unknown Ti diffusion probably induced by other methods, a method which utilizes photolithography and Ar-ion etching technique as well as a gold lift-off process, was chosen for patterning the electrodes and the interface structures. The process is characterized with four steps, as shown in Fig. 2.8: (1) photolithography gave well defined holes and structures with hundreds of micrometers; (2) with photoresist (PR) as a soft mask, the samples were moved to a dry etching chamber for Ar-ion etching and this will lead to the exposure of buried interfaces; (3) deposition of gold or platinum on top of etched samples; (4) use acetone to remove PR and Au or Pt were lifted-off. The Au or Pt pads were then contacted with wires using silver paint or wire-bonding.

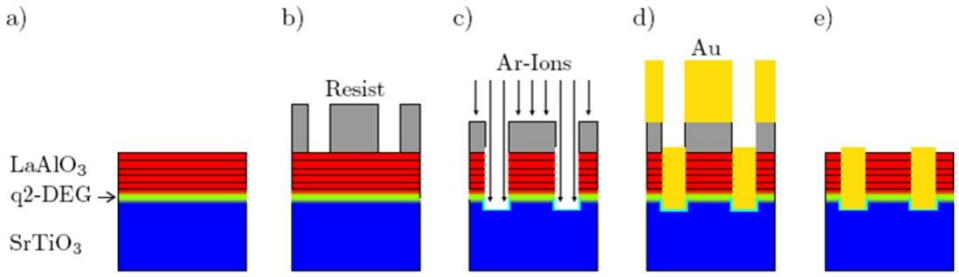

Figure 2.8 Typical process of etching and electrode patterning utilized in this work.

(Original sketch adopted from Ref. [104])

Another simpler and more stable approach to obtain well defined contacts with interfaces is developed by using growth of amorphous layer of $SrTiO_3$ as soft mask. The details will be discussed in Chapter 4.

2.5 Transport Measurements

In this work, all the electrodes were patterned into a van der Pauw geometry or a Hall bar geometry. After all the contacts to the interfaces were made, the samples were mounted onto connector boards and all the contacts were connected to the pads on the boards by wire-boding or gluing using silver paint. Electronic transport measurements were performed by using Keithley 2400 and 2410 source meters combined with a cryogenic stage (controller: Lakeshore 350) using a compressor as refrigeration system. In the resistance measurements performed at University of Geneva, different experimental setup was built up by including a dewar with liquid helium, whose skematic is drawn in Fig. 2.9(a). Hall measurements were carried out by vibrating sample magnetometer (VSM) system (Lakeshore 7400). A picture of a VSM facility in our lab is shown in Fig. 2.9(b).

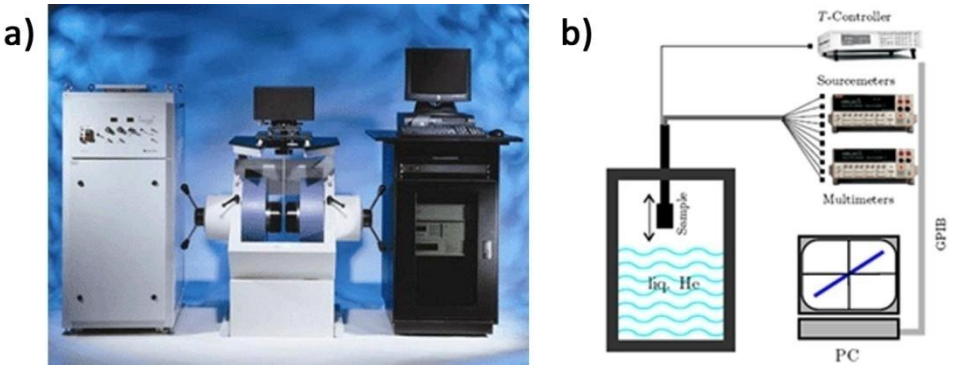

Figure 2.9 (a) Photo of the VSM system in the lab; (b) Sketch of experimental setup used for the transport measurement using liquid helium in University of Geneva (sketch adopted from Ref.[104]).

2.5.1 Resistance Measurement

In thin film characterizations, a specific definition of resistance named as sheet resistance (R_S) is often used to probe the resistivity properties of the subject. By utilizing appropriate electrode geometries, sheet resistance, which is applicable to two-dimensional systems and analogous to resistivity used in three-dimensional systems, can be obtained from electronic transport measurements. From fundamental physics, we know that in a regular three-dimensional resistor, the resistance can be written as:

$$R = \rho \frac{L}{A} = \rho \frac{L}{Wt}$$

where ρ is the resistivity. A is the cross-sectional area of the resistor and L is the length. A can be written as a production of width W and the sheet thickness t. By grouping ρ with t, the resistance can be further written as:

$$R = \frac{\rho}{t} \frac{L}{A} = R_S \frac{L}{W}$$

R_S is then the sheet resistance. The unit of RS is specially termed as "ohm per square" or "Ω/□", which is dimensionally equal to an ohm but is exclusively for sheet resistance.

From the equation above, one can thus obtain R_S by measuring the resistance of the materials using a certain sample configuration (which gives L and W or the ratio of L and W). In this work, two commonly used geometries, van der Pauw (VDP) geometry and Hall bar geometry were utilized. The former one is specifically introduced here and the latter one will be mentioned in Chapter 4.

The van der Pauw method is commonly used to measure the sheet resistance of a material and it is also quite often used to measure the Hall effect. The method was firstly proposed by Leo J. van der Pauw in 1958 [112]. Some typical contact configurations are presented in Fig. 2.10(a). If all the contacts are numbered from 1 to 4 in a counter-clockwise manner, beginning from the top-left contact [see Fig. 2.10(a)], one can consider 1,3 or 2,4 for the voltage leaving the other pair of contacts

for the current respectively using four-points resistance measurement. For example, current (I) can be induced between contacts 1 and 3 and the voltage across 2 and 4 (V) will be measured using a voltage meter. The general four-points resistance can be deducted as $R = V/I$. The sheet resistance (R_S) can then obtained by considering the dimensions.

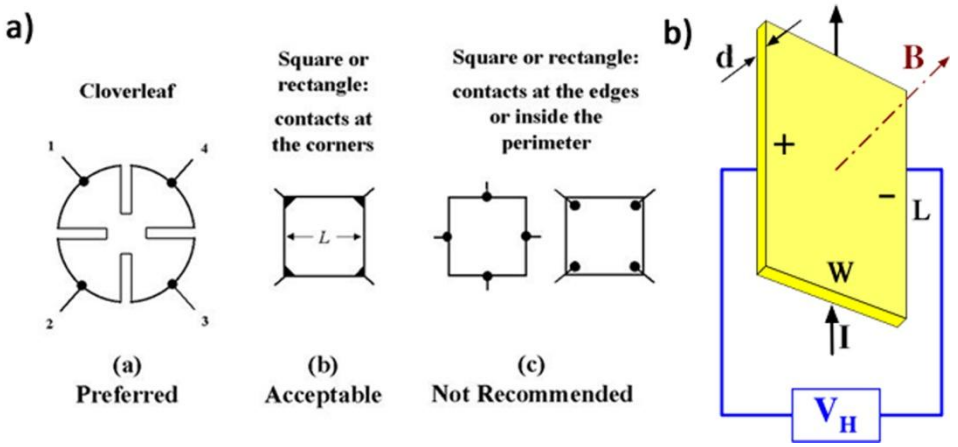

Figure 2.10 (a) Electrode configuration adopted in resistance measurement using van der Pauw method (picture from Ref. [113]); (b) sketch of Hall effect in a conductor (picture from Ref. [114]).

2.5.2 Hall Measurement

As shown in Fig. 2.10(b), when a current flows in a conventional conductor, Hall effect can be observed in the presence of a magnetic field perpendicular to the current. The current consists of the movement of many small charge carriers, typically electrons, holes, or both. Usually, the charges follow approximately straight, 'line of sight' paths between collisions with impurities, phonons, etc. However, when a perpendicular magnetic field is applied, moving charges experience a force, which is called the Lorentz force. And their paths between collisions are curved so that moving charges accumulate on one side of the material. This leaves equal but opposite charges located on the other side, where there is a scarcity of mobile charges. This results in an asymmetric distribution of charge density across the conductor that is perpendicular to both the 'line of sight' path and the applied magnetic field. The

separation of charges establishes an electric field that opposes the migration of further charges, so a steady electrical potential builds up for as long as the charge is flowing. From the establishment of this balance (Lorentz force F_L equals electrostatic force F_E), the built-up potential written as V_H can be obtained as:

$$V_H = \frac{-IB}{dne}$$

where I is the current across the conductor length, B is the magnetic flux density, d is the thickness of the conductor [Fig. 2.10(b)], and n is the charge carrier density of the electrons. The Hall coefficient is defined as:

$$R_H = \frac{E}{jB}$$

where E is the electric field established from electric potential, and j is the current density. And this becomes:

$$R = \frac{E}{jB} = \frac{dV_H}{IB} = -\frac{1}{ne}$$

So charge carrier density can be obtained from Hall effect. Furthermore, if the conductor is a two-dimensional conductor, by using the equation:

$$R_S = -\frac{1}{n\mu_B e}$$

where R_S is sheet resistance of the two-dimensional conductor, carrier mobility can be further determined from Hall measurement. Therefore, Hall measurement is regarded as a very important means to probe both the intrinsic microcosmic characteristics of the charge carriers within the matters and the macroscopic electronic transport properties of the matters.

CHAPTER 3

TRANSPORT PROPERTIES OF $DyScO_3/SrTiO_3$ HETEROSTRUCTURES

3.1 Introduction

A still ongoing debate concerns the origin of the conducting interface formed between LAO and STO. The doping mechanism was firstly proposed to be an electronic reconstruction which avoids the "polarization catastrophe" due to the polar discontinuity [6, 115]. Quite soon, it was proved that the original explanation should be extended to include the formation of oxygen vacancies in $SrTiO_{3-\delta}$ [68, 81]. Moreover, even in an ideal atomically sharp interface, lattice distortions caused by epitaxial strain will occur and such distortions have great impact on the electronic structures.

Basically, according to the general view of the "polar discontinuity" model, instead of LAO, other perovskites which has the similar lattice constants and consist of polar atomic planes, like $LaTiO_3$, $KTaO_3$, $KNbO_3$, $LaGaO_3$, etc., should also give such conducting interfaces with high mobility electron gases. In fact, some of them have already been reported or claimed to possess similar electronic properties to LAO in both experimental and theoretical ways [80, 116-119]. In this chapter, we choose the perovskite $DyScO_3$ (DSO), which also hosts polar atomic planes, to fabricate DSO/STO heterostructure and we present electronic properties of such heterointerface grown at different oxygen pressures.

Some research has been done on the investigation of the interfacial intermixing and charge accommodation at the interfaces by using an aberration-corrected scanning transmission electron microscopy (STEM) and electron energy-loss

spectroscopy (EELS) [120]. They claimed that in form of cation intermixing at the interfacial region, charge compensation and neutrality are established at DSO/STO interfaces, as shown in Fig. 3.1, which is in contrast to the LAO/STO system. However, one should notice that the substrates they used in their work are silicon wafer covered with a 40-nm thick epitaxial STO, which can be completely different to the situation of generation of q2-DEG between LAO films and STO single crystals. Considering the vital role that single crystal STO may play in, as mentioned in Chapter 1, their work may focus on a different system.

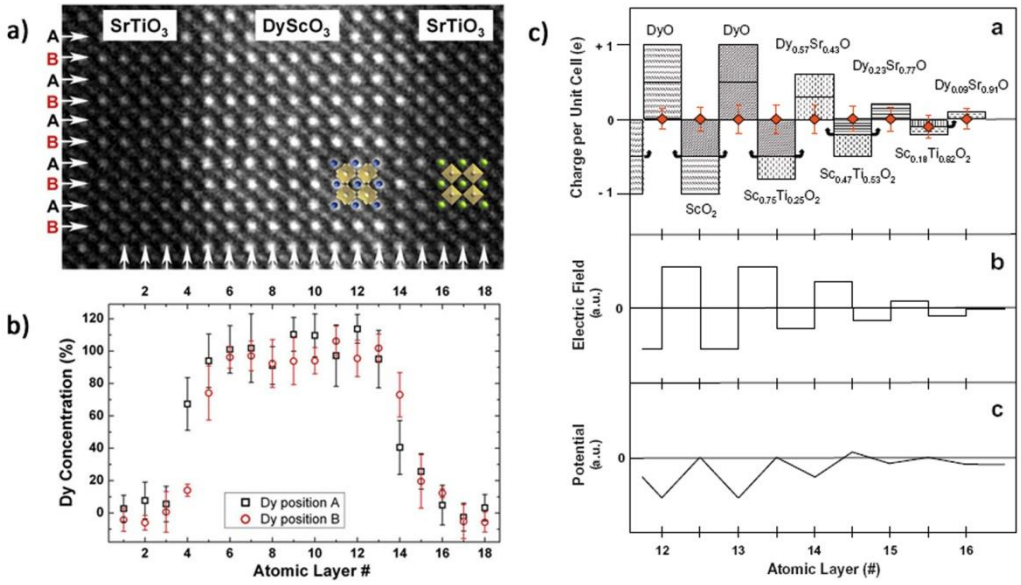

Figure 3.1 (a) HAADF image of $DyScO_3/SrTiO_3$ multilayers; (b) The Dy concentration evaluated from (a); (c) Summary of charges, electric filed and potential according to the composition for layers 12-16 shown in (a). (Adopted from Ref. [120])

$DyScO_3$ has an orthorhombic structure ($GaFeO_3$ type, lattice constants a = 5.440 Å, b = 5.713 Å, c = 7.887 Å) and the perovskite pseudo-cubic lattice constant is 3.944 Å. We choose DSO because it holds the same polarity as LAO, but has a lattice mismatch with STO of less than 1%, resulting in larger critical thickness for strain relaxation. This gives the possibility to fabricate nearly defect-free epitaxial DSO thin films with high quality interfaces. As presented in Fig. 3.2, DSO consists of

monovalent cations Dy^{3+} and Sc^{3+}, and therefore, the DSO lattice along the [001] pseudo-cubic direction is composed of stacks of alternating $(DyO)^+$ and $(ScO_2)^-$ layers, which carry a charge of $+e$ and $-e$, respectively, per two-dimension unit cell. Thus a polar discontinuity arises when $(DyO)^+$ layer joins charge-neutral $(TiO_2)^0$ layer which is on the top surface of STO substrate. Since Ti ion allows for mixed valence charges, polar discontinuity will conceivably result in a net electron transfer across the interface, which produces electron doped "n-type" interface. This electronic reconstruction at such interface will accommodate electrons in initially unoccupied *d*-shells of interfacial Ti atoms, making the interface conducting. Besides that, similar to LAO/STO interface [116], charge compensation by cation intermixing can be established at DSO/STO interface [80]. This phenomenon may have great impact on the transport properties of such interface.

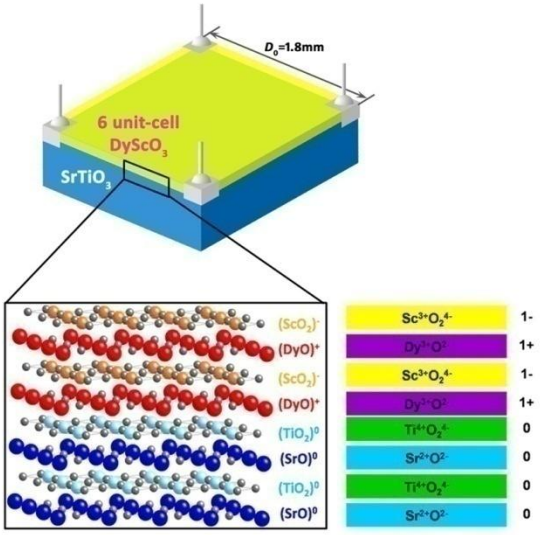

Figure 3.2 Schematic diagram of a 6 unit-cell DSO on STO heterostructure used in this work and the electronic structure at interfaces which can build up polarization continuity.

3.2 Experimental Details

$DyScO_3$ films were deposited in a ultrahigh vacuum chamber by Laser-MBE

with an KrF excimer laser (λ=248 nm) using a polycrystalline $DyScO_3$ target on TiO_2-terminated single crystal $SrTiO_3$ (001) substrate [96]. The $DyScO_3$ target was prepared by a conventional solid-state reaction method. Prior to the depostion, the substrate was pre-cleaned by acetone and ethanol to remove any organic reminants on the surface. During film growth, the substrates were kept at 750 ℃ as measured by a pyrometer and the oxygen partial pressure was dynamically controlled at 10^{-6} -10^{-3} mbar. The laser pulse repetition rate is 1 Hz and the fluence is about 2 J cm^{-2}. Reflection high-energy electron diffraction (RHEED) was utilized to monitor the growth process. After the deposition, the samples were *in-situ* annealed under 10 mbar O_2 pressure for 1 hour at 400 ℃ in order to compensate the oxygen vacancies but avoid the possible intermixing of cations at interfaces. The samples were then mechanically polished or patterned using photolithography conbined with reactive ion etch into van der Pauw geometry or Hall bar geometry. The interfaces are all ohmic contacted by aluminim wires using wide-temperature-range silver paint.

Room-temerature atomic force microscopy (AFM) (Veeco Digital Instrument Multimode IV) was carried out to investigate the topography of the Buffered-HF etched $SrTiO_3$ substrate and to determine the surface quality of $DyScO_3/SrTiO_3$ heterointerfaces. The scan speed is maintained at 0.5 Hz. High-resolution transmission electron microscopy (HR-TEM) (JEOL JEM 2010, 200kV) was used to examine the interface quality and to confirm the results obtained from RHEED intensity oscillations. For the photoluminescence (PL) measurement to charactorize the states of oxygen defects, the system utilized is an FLS920P Edinburgh Analytical Instruments apparatus equipped with a μF900H high energy microsecond flash lamp and a 450W xenon lamp.

Electric transport measurements were performed by using Keithley 2400 and 2410 source meters combined with a cryogenic stage (controller: Lakeshore 350) using a compressor as refrigeration system. Hall measurements were carried out by vibrating sample magnetometer (VSM) system (Lakeshore 7400). For careful analysis of the intrinsic properties of the interfaces, all the samples were shielded

from any light for 24 hours before the measurements in order to suppress the effects of possible photocarrier injection. Gate electrode configuration for semiconductors was utilized in electric field effect measurement. A copper plate was used as back gate electrode adhered at backside of the samples by wide-temperature-range silver paint and a Keithley 2400 was used as a voltage source.

3.3 Surface Quality of Treated Substrates

3.3.1 Treatment Process

As-received commercialized STO single crystal substrates usually have surfaces of mixed terminations. Through suitable treatment steps, TiO_2-terminated surface can be uniformly obtained. The treatment used in this project include: (1) the as-received substrates were bathed ultrasonically in deionized water (55 ℃-60 ℃) for 15-20 minutes; (2) the substrates were then dried in compressed air stream (CAS) or compressed nitrogen (CN); (3) after that, they were immersed into buffered-HF (BHF, commercially available at Merck company with NH_4F:HF=87.5:12.5) for a certain time period; (4) sequentially, the etched substrates were ultrasonically cleaned in deionized water and ethanol for 10 minutes, respectively; (5) then dried in CAS or CN; (6) finally they were moved into an oven to be annealed in atmosphere or pure oxygen ambient at 950 ℃-1000 ℃ for 2 hours.

3.3.2 Topography of Substrate Surfaces

Figures 3.3(a)-(c) display topography of different substrates after immersed into BHF for different time intervals (before annealing). We can clearly identify the steps and terraces from all these three images, although for Figs. 3.3(a) and (b) the surfaces are a little “blurry”. However, it is obvious that large peaks and holes as well as rough terrace edges are easy to form under longer etching time. In contrast, 1 minute of immersion in BHF leads to a cleaner and more flat surface.

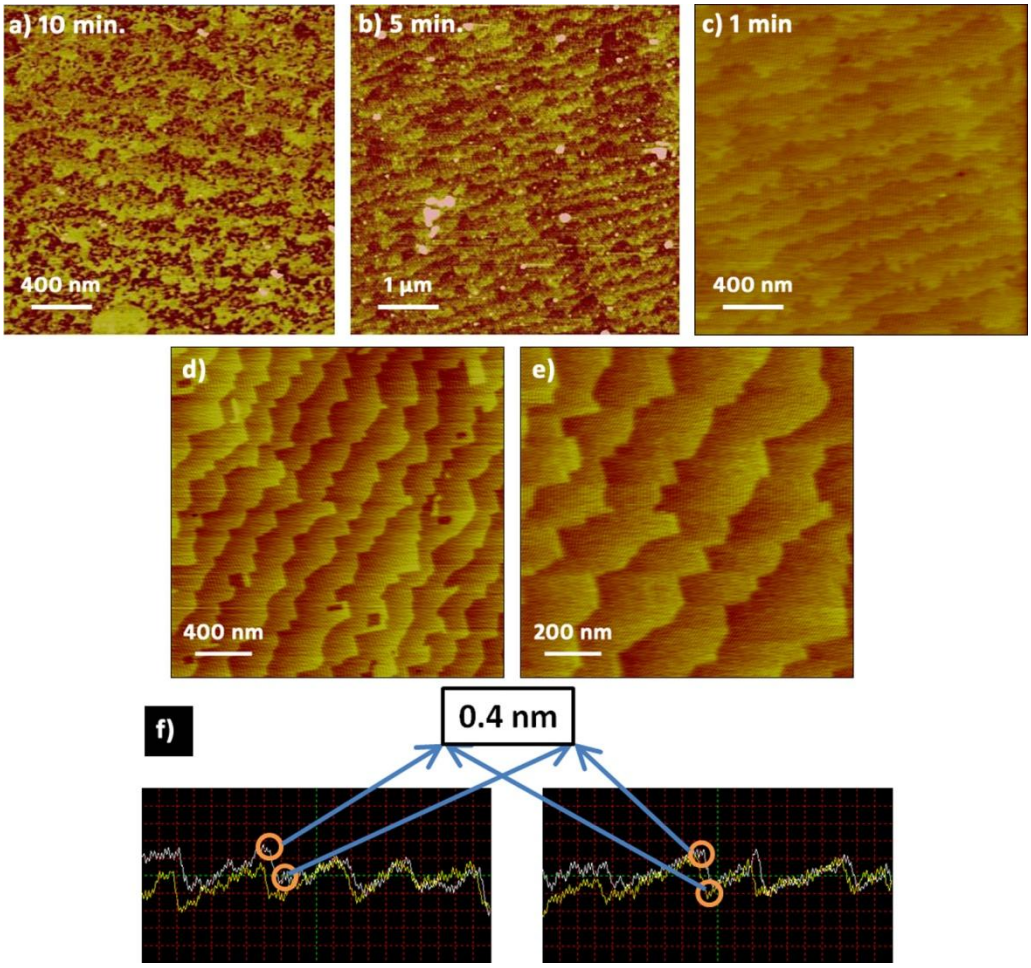

Figure 3.3 AFM images and signals of STO substrates taken immediately after the etching and after an annealing step: (a) after 10 minutes' etching in BHF; (b) after 5 minutes' etching; (c) after 1 minute's etching; (d), (e) after annealing in atmosphere at 1000 ℃ for 2 hours (2 μm and 1 μm images, respectively); (f) AFM tapping mode topographical signal during measurement in (e).

By means of a sequential annealing step [96] at 1000 ℃ for 2 hours after the BHF etching, surface quality can be much improved, as shown in Figs. 3.3(d)-(f). From the images, we can observe sharper terrace edges and more flat terraces due to the recrystallization of the surface of STO at high temperatures. At temperature above 850 ℃, the atoms attached to the terrace edges start to be mobile and they can thermodynamically migrate to fill those surface vacancies caused by HF etching. As a result, the edges become smooth. Moreover, from the AFM signals, a step height of

0.4 nm corresponding to single unit cell is well confirmed. But still, some holes with depth of single unit cell and some sharp corners with 90° can be observed on the substrate surface even after annealing. Optimization of all the parameters in the whole treatment process can give high quality of TiO_2 terminated STO substrate surfaces, as in Fig. 3.4.

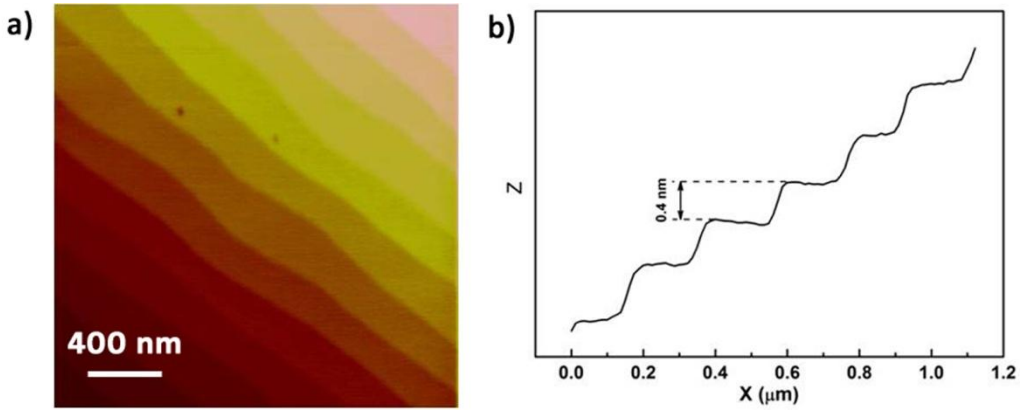

Figure 3.4 (a) Topography of treated STO substrate surface after plane fitting; (b) surface profile of image (a) confirms single-unit-cell height steps.

3.4 Structural Properties of $DyScO_3/SrTiO_3$ Heterostructures

3.4.1 Growth Process Monitored by RHEED

The deposition was *in-situ* monitored by RHEED. The RHEED pattern prior to the growth at deposition temperature contains streaky spots on the 0^{th}-order Laue circle [see Fig. 3.5(a)] corresponding to intersection of Ewald sphere and the STO reciprocal lattice. It indicates a perfect crystalline surface [66]. Figure 3.5(b) is the RHEED pattern during sample annealing after 150 seconds DSO deposition. The shape of spots is blurred into clear streaky lines, indicating a two-dimensional layer-by-layer growth. The layer-by-layer growth behavior is further confirmed by the RHEED intensity oscillation of specula reflection during growth of DSO [see Fig. 3.5(c)]. The oscillation of peak-to-peak RHEED intensity demonstrates the completion of a unit-cell layer formation. In this case, the total thickness of this DSO

sample is determined to be about six unit cells.

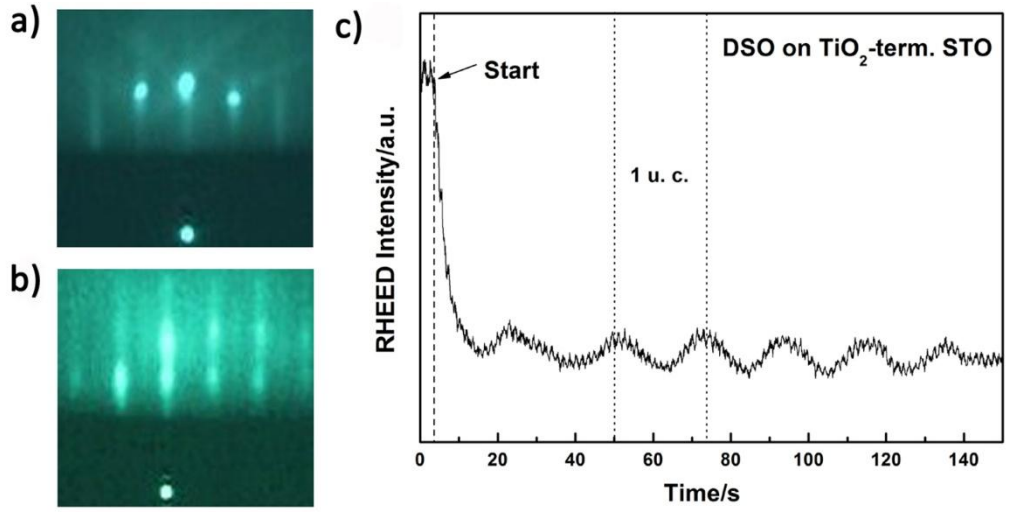

Figure 3.5 RHEED patterns and intensity oscillation: (a) RHEED patterns of STO substrate prior to deposition at 750 ℃; (b) RHEED patterns after 150 seconds deposition of DSO; (c) RHEED intensity oscillation of DSO deposition, indicating a layer-by-layer growth (the arrow indicates when laser pulse starts).

3.4.2 Structure of Thin Films and Interfaces

After film deposition, *Ex-situ* atomic force microscopy study revealed that the step and terrace structure of the STO surface is preserved, confirming a well 2D layer-by-layer growth of the DSO films (see Fig. 3.6). One of the six-unit-cell samples was imaged by a high-resolution transmission electron microscope (HR-TEM) confirming the high-quality interface and the thickness estimation from RHEED (see Fig. 3.7).

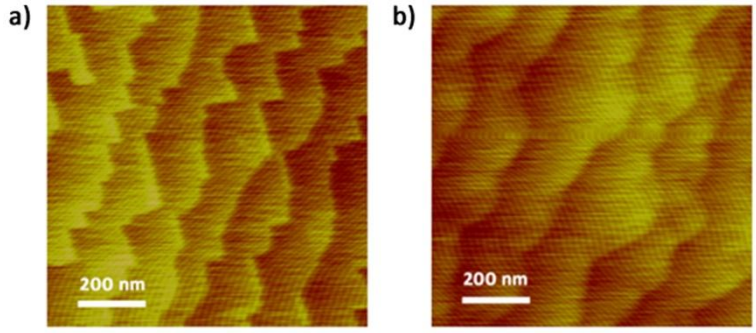

Figure 3.6 (a) Topography of BHF-etched STO substrate surface; (b) Steps were well maintained after deposition of DSO.

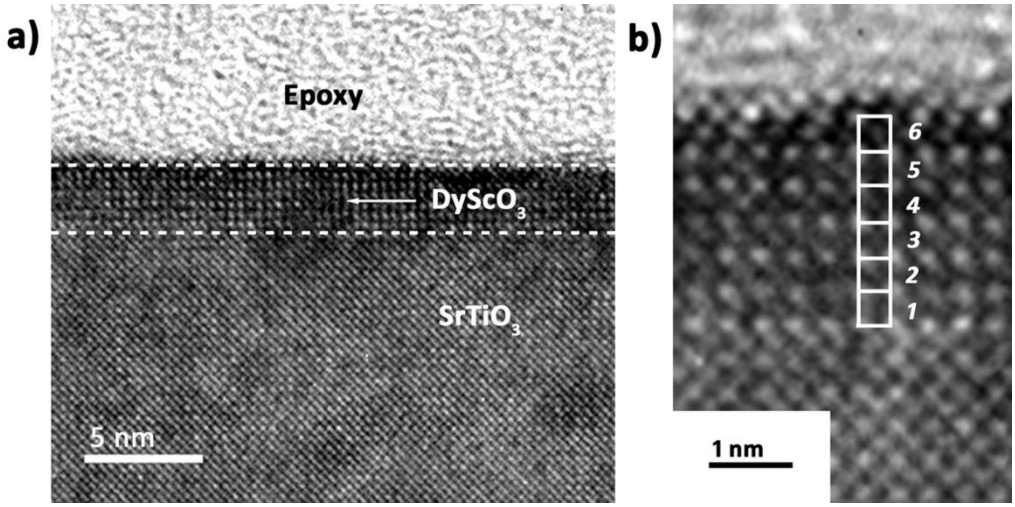

Figure 3.7 (a) High-resolution TEM image of DSO/STO interface; (b) Magnified picture of (a).

From Fig. 3.7(b), it can be seen that the interface is very sharp implying that the surface of STO substrate is atomic-scale flat and the quality of the heterointerface is good. Clear bright atoms representing Dy ions in DSO unit cells can be clearly identified and we count the number of layers the same as the number of RHEED oscillations. Although a sub-unit layer can be found at the film surface after a complete growth of exact six unit cells, virtually indicating 6.5-unit-cell in thickness at some places, we name these samples as six-unit-cell samples in the following context.

3.4.3 Defect States Characterization

We performed room-temperature photoluminescence (PL) experiments on DSO/STO samples grown under different oxygen pressures (10^{-6}-10^{-4} mbar) to characterize the oxygen vacancy states within STO substrates because oxygen-vacancy-doped STO can be conducting. The results of the PL measurements are presented in Fig. 3.8. The wavelength of the emitted light (around 450 nm) from all the samples is the same within the precision of the experiment. From Fig. 3.8, one can see that when the deposition oxygen pressure is low (10^{-6} mbar and 10^{-5} mbar), the samples display the characteristic peak, which agrees well with the wavelength of light emitted from reduced STO reported in Ref. [111, 121, 122]. This is ascribed to trapped states within the band gap created by oxygen vacancies. Light emitted from samples grown at higher oxygen pressure (10^{-4} mbar) is too weak to be detected using PL equipment indicating bare or low concentration of oxygen vacancies.

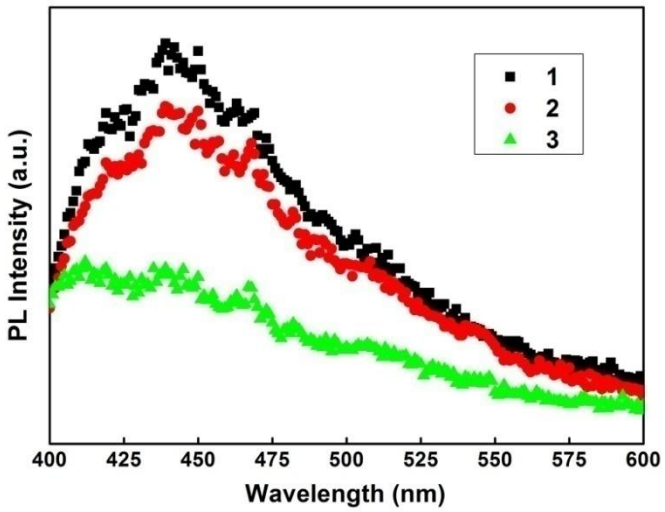

Figure 3.8 PL intensities of different DSO/STO samples grown under different oxygen pressure (P_{O_2}): (1) $P_{O_2}=10^{-6}$ mbar; (2) $P_{O_2}=10^{-5}$ mbar; (3) $P_{O_2}=10^{-4}$ mbar. The characteristic peaks in 1 and 2 correspond to luminescence by oxygen vacancies.

3.5 Electronic Transports of $DyScO_3/SrTiO_3$ Heterostructures

3.5.1 Electrode Patterning

As mentioned in Chapter 2, generally in order to study the transport properties of the DSO/STO interface, contacts need to be etched into the DSO layer and filled with gold in a van der Pauw (see Fig. 3.2) or Hall geometry in all samples following the process showed in Fig. 2.7. Before the etching and the electrode patterning for the samples, the etching rate in STO needs to be calculated. Ar^+/CF_4 plasma was used for dry etching and the etching conditions are listed in Table 3.1. STO substrates were used for the calibration.

Table 3.1 Etching parameters

Parameters	Value
Plasma power	400 W
Bias power	150 W
Ar^+ rate	80 ccm
CF_4 rate	20 ccm

After an etching trial for 12 minutes, an etching depth of ~25 nm can be observed and measured by AFM, as shown in Fig. 3.9. Thus the etching rate under such condition is estimated to be 2 nm/min. This etching rate can be used to estimate the etching depth for the electrodes.

This electrode patterning technique is a typical effective means, which has been utilized for efficiently measuring the interfaces and in-plane physical properties of ultra-thin films. Many groups use this technique to probe the buried interface between LAO and STO. Besides, predictably, it will crucially function for future multilayer structures and devices based on LAO/STO interfaces, such as LAO/STO-based spin-FET (see details in Chapter 5). Thus this technique is mentioned here.

However, the solidification of the photoresist can be a stubborn problem because it makes the photoresist hard to remove. In this work, in order to minimize this harmful effect and maintain the unity of measurement conditions for all the prepared

samples, all the samples were cut into small squared pieces (dimension: 1.8 mm). After the corners of the samples were mechanically whetted and polished, platinum electrodes were deposited according to van der Pauw configuration to have high-quality ohmic contact with the heterointerface.

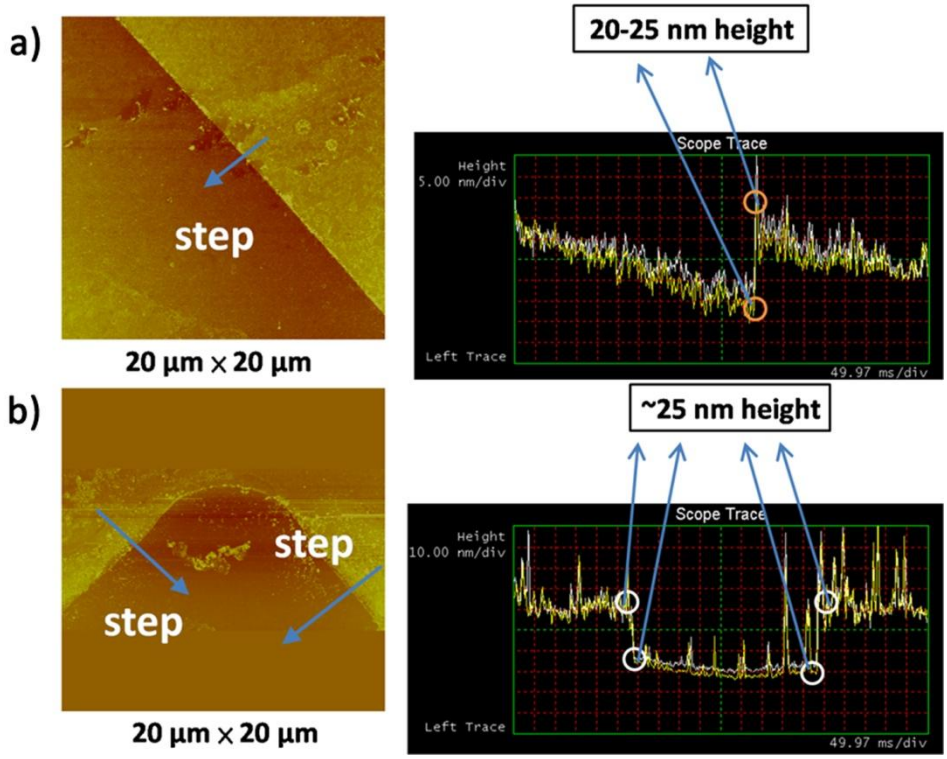

Figure 3.9 Topography of the etched STO substrate showing etching depth of ~25 nm: (a) across a pattern edge (line); (b) a corner of a square pattern.

3.5.2 Electronic Transport Properties

We examined the interface conductivity by using Keithley source meters combined with a cryogenic stage and Lakeshore Hall measurement system. Fig. 3.10 shows the PO_2 dependence of the transport properties of these DSO/STO samples. The temperature dependence of sheet resistance R_S is given in Fig. 3.10(a) for the six-unit-cell sample grown at different oxygen pressures. It can be seen that the resistivity increases significantly as the growth oxygen pressure increases. For the samples grown at $PO_2 = 10^{-6}$ mbar or 10^{-5} mbar, metallic behavior can be observed

down to low temperatures; this is similar to the results reported by other groups on LAO/STO interfaces [68, 81]. For the sample grown at $PO_2 = 10^{-4}$ mbar, one can see the presence of a resistance upturn for temperatures below about 90 K. To analyze this metal-to-semiconductor (M-S) transition, we measured temperature-dependent mobility μ_H from Hall effect [see Fig. 3.10(b)]. We observed that at the M-S transition temperature, which is about 90 K, μ_H becomes temperature independent suggesting a drop in the mobile carrier density. (Further details of this M-S transition is discussed in Section 3.5.3) When PO_2 increases to 10^{-3} mbar, the sample shows obvious insulating behavior. The set of data demonstrates that oxygen pressure PO_2, and thus oxygen vacancies formed during deposition process, plays an important role in generating this metallic high-mobility electron gas.

Since the origin of the conductivity and the free carriers at DSO/STO heterointerface are of interest, from the Hall measurement of the samples grown under different PO_2, we obtain the temperature dependence of *n*-type sheet carrier density n_s and we calculate the corresponding carrier mobility μ_H shown in Fig. 3.10(b). It is noted that in some oxides under magnetic field, the Hall resistivity includes an additional contribution, known as the Extraordinary Hall effect (or anomalous Hall effect) and is often much larger than the ordinary Hall effect. This effect can be either an intrinsic effect which relates to the Berry phase effect in the crystal momentum space (k-space) or an extrinsic effect (disorder-related) due to spin-dependent scattering of the charge carriers. The anomalous Hall effect leads to a nonlinear contribution to the relation of Hall resistivity as a function of the magnetic field, which will complicate the calculation of the charge mobility. However, in this DSO/STO heterostructure, since the main charge carriers responsible for transport are free electrons, showing a metallic transport behavior, which give rise to the linear feature in the magnetic field dependent Hall resistivity. Hence, the Hall mobility can be calculated from the equation:

$$\mu_H = -\frac{1}{n_S R_S e}$$

where e is the electron charge. The curves in Fig. 3.10(b) demonstrate extremely high

carrier mobility at low temperatures, around 10^4 cm^2 V^{-1} s^{-1} below 20 K, for samples grown under low PO_2 (10^{-6} mbar and 10^{-5} mbar), and these samples display a residual resistivity ratio (RRR) as high as 10^3. Besides, very high sheet carrier density can be determined to be about 10^{17} cm^{-2}. These two results can be explained by a simple model including the possible role of defects/oxygen vacancies in the top layer of STO, where charge carriers originate from but move into pristine STO crystal, and as a result, these carriers tolerate much less scattering, and thus, appear as a very high charge carrier density as well as high mobility [81, 123].

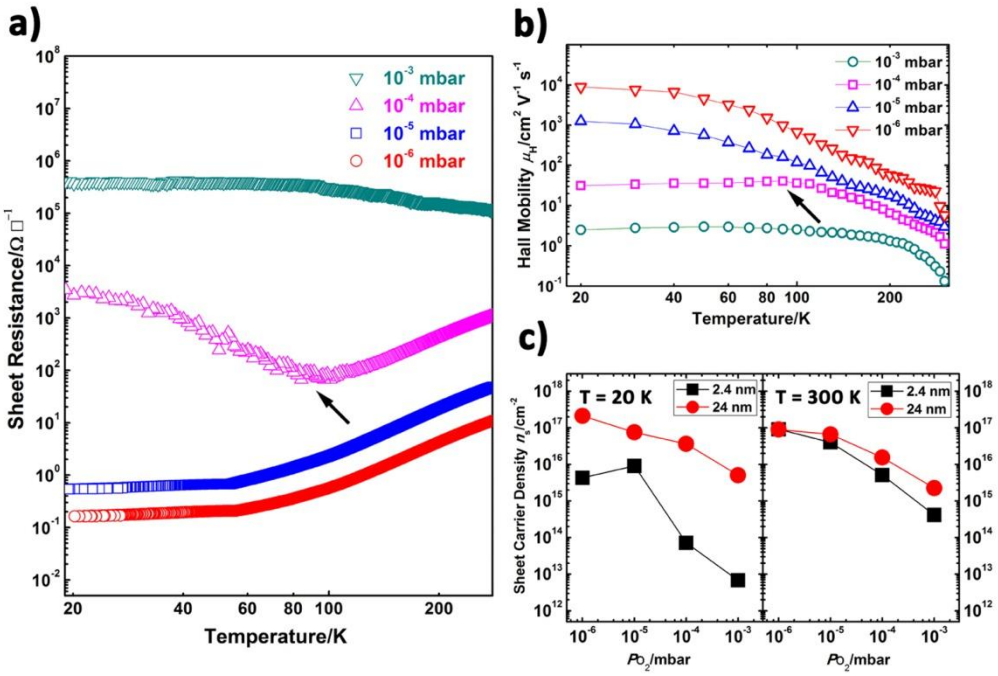

Figure 3.10 (a) Temperature-dependent sheet resistance and (b) Hall mobility vs. temperature for DSO/STO interface in the 6 unit-cell film under different PO_2 during growth; (c) Temperature and PO_2-dependent sheet carrier densities for samples with different thicknesses. The arrow indicates the metal-to-semiconductor transition occurs in the sample grown at $PO_2 = 10^{-4}$ mbar.

For the samples grown at higher oxygen pressure (10^{-4} mbar), the sheet carrier density drops off to approximately 10^{14} cm^{-2} [see Fig. 3.10(c)] which approaches the calculated value from the "polar discontinuity" model (about 3.28×10^{14} cm^{-2}). This

could indicate that the high conductivity in the samples grown under high PO_2 is due to the electron gas induced by the polar discontinuity.

Besides that, as shown in Fig. 3.10(c), temperature-dependent sheet carrier density obtained from the thinner film (2.4 nm corresponding to approximate 6 u. c.) changes dramatically; whereas in the thicker film (24 nm corresponding to approximate 60 u. c.), no obvious change occurs. This phenomenon can be rationally interpreted by the competition between defect-layer generated carriers and polar interface induced band bending. On one hand, a thicker DSO capped layer prevents absorption of atomic oxygen in the topmost layer of $SrTiO_{3-\delta}$ during annealing. Hence the oxygen defects dominate the conductivity in the whole cooling process, and therefore, result in a relatively high sheet carrier density (~10^{16} - 10^{17} cm^{-2}), and there is only a little difference between the curves at T=20 K and T=300 K. On the other hand, for the thinner film, oxygen vacancies are compensated during annealing. So when temperature drops to cryogenic regime, small quantity of residual oxygen vacancies induced charge carriers are restrained due to the subdued thermal activation, and as a result, free electrons in the conduction band of STO injected from valence band of DSO (due to polar catastrophe induced band bending [124]) become a dominant factor. Therefore, a dramatic difference between the curves at T=20 K and T=300 K for the 6-unit-cell film can be seen. These intriguing results imply that at least two kinds of charge carriers coexist at such a polar heterointerface, in consistent with earlier results obtained from optical experiment and dc measurement in LAO/STO system [70].

3.5.3 Metal-to-Semiconductor (M-S) Transition

In the sample grown under PO_2 = 10^{-4} mbar condition, as mentioned above, an interesting upturn behavior can be observed around 90 K in sheet resistance [see Fig. 3.10(a)], and correspondingly, a maximum appears in the temperature-dependent Hall mobility [see Fig. 3.10(b)] at the same temperature; both of which strongly suggest a metal-to-semiconductor (M-S) transition in this system.

This kind of phenomenon probably indicates charge localization when the temperature is below 90 K. We propose a simple model to interpret this M-S transition when temperature drops to around 90 K. Basically, at this level of oxygen partial pressure (PO_2 = 10^{-4} mbar), the DSO/STO system contains two competitive conducting mechanisms: one is the oxygen vacancy induced conductivity in the film which is semiconducting and the conductivity is exponentially decreased when temperature decreases; while the other mechanism is electron-doped interface showing metallic behavior whose conductivity increases when temperature drops (but not as fast as the decrease of conductivity of semiconductor at low temperature). Consequently, the total conductivity is contributed by these two mechanisms and an M-S transition can be expected for a certain density ratio of free electrons at the interface and n-type carries in the film.

When temperature decreases at the beginning, significant decrease of sheet resistance due to the less phonon scattering for the free electrons results in a considerable reduction in the temperature-dependent sheet resistance; but when temperature decreases below 90 K, the fact that abundant carriers in semiconductors are restrained and localized in the cryogenic regime should be responsible for the rapid increase in the resistivity of the whole system. As a result, pronounced M-S transition occurs.

The simulated work based on this consideration fits well with our experimental data, as shown in Fig. 3.11. As discussed before, we propose that the conductivity at the heterostructure is related to two mechanisms, one of which is n-type semiconducting behavior due to the oxygen deficiency induced electrons and the other obeys metallic temperature dependent rule caused by free electrons at the interface. For a metallic system, according to Matthiessen's Rule, the resistance as a function of temperature can be written as:

$$R_M(T) = R_1 + aT^2 + bT^5 + cT$$

where T^2 and T^5 terms are suggestive of electron-electron and electron-phonon

scattering, relevant at high temperatures. And for an intrinsic semiconductor, the resistance decreases as temperature increases because of the electrons bumped into the conduction band (CB) due to thermal activation, therefore obeys the exponential relation:

$$R_S(T) = R_2 e^{-aT}$$

By considering these two factors in contribution to the $R_S(T)$, the temperature dependent resistance of the 6-unit-cell DSO sample grown at 10^{-4} mbar can be fitted by the sum of $R_M(T)$ and $R_S(T)$, as shown in Fig. 3.11(a). At temperature region below 90 K, the temperature dependence of the sheet resistance is found to be logarithmic over one decade (30-90 K) and an activation energy of 14.9 meV can be obtained from $\ln\sigma \sim 1/T$ relation, suggesting the carrier thermal "hopping" at low temperature region, as shown in Fig. 3.11(b).

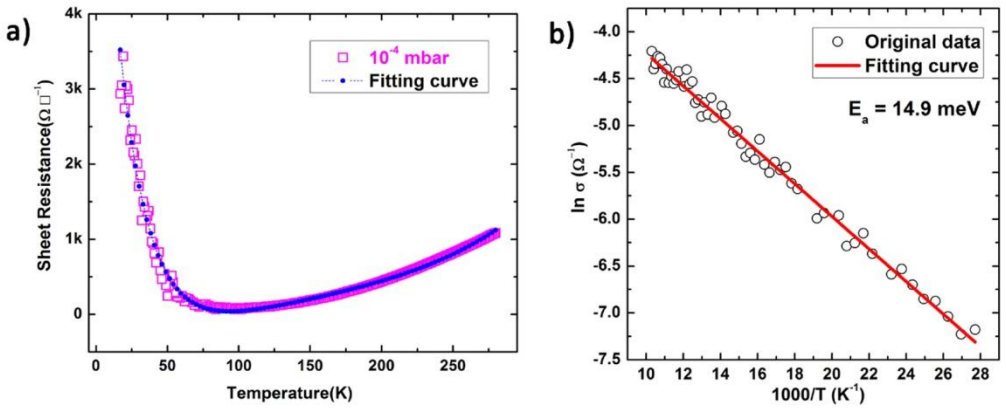

Figure 3.11 (a) Sheet resistance as a function of temperature of the 6-unit-cell DSO sample grown at 10^{-4} mbar oxygen pressure (open square) and the fitting curve using equations above; (b) Linear relationship of logarithmic conductance as a function of reciprocal temperature ($\ln\sigma \sim 1/T$).

3.5.4 Field-Effect Measurements

It is also believed that STO itself plays a significant role in the M-S transition mentioned above for the reason that at low temperature the dielectric constant of STO

diverges as it approaches incipient-ferroelectric transition [18], though the mechanism underlying this transition is still unclear. Nevertheless, if the interface is dominantly doped by electrons, one should be able to modulate these dopants and investigate the nature of the carriers through a field effect by applying a bias voltage across the substrate. This is well known as electric field doping for the interfaces. To testify our assumption here, we apply a gate voltage across the STO substrate to the conducting channel by using back gate electrode geometry (see Fig. 3.12). The large thickness of the STO (0.5mm) substrate compared to the small width of the conducting channel (typically a few nanometers) allows a further enhancement of the charge modulation due to the fringing field effect.

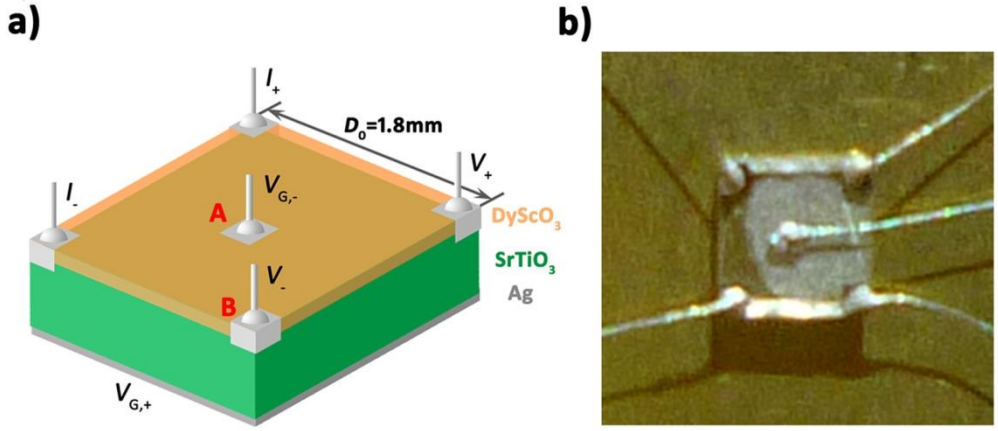

Figure 3.12 (a) Schematic diagram of the configuration for field effect measurement. V_+, V_-, I_+, I_- are for sheet resistance R_S measurement and Gate voltage was applied between $V_{G,+}$ and $V_{G,-}$. We short electrode A ($V_{G,-}$) and electrode B (V_-) to obtain the same ground in this configuration; and (b) picture of the sample by using the configuration in (a).

Figure 3.13 displays the temperature-dependent sheet resistance of different samples applied with different gate voltages. The samples grown under 10^{-6} mbar oxygen partial pressure shows tiny change in sheet resistance under large electric field, indicating a defect-layer originated carrier domination, which is in consistent with previous analysis. However, the sample grown under 10^{-5} mbar oxygen partial

pressure shows significant change of resistance in one order, implying the existence of field effect.

Very surprising results came out when we measured the sample presenting M-S transition, where with an applied gate voltage as low as 80 V, the M-S transition disappeared and a clear metallic behavior with R_S (280 K)/R_S (20 K) ~ 10^3 presented. The enormous field effect indicates successful modulation of the carriers and even quantum phase transition at the interface by field effect. We attribute this field effect modulation of sheet resistance to the change of ratio of free electrons at the interface and n-type carries in the film. And also, in the process, the polar catastrophe caused band bending can be drastically affected by the electric field, where relatively large electric field provokes large band bending resulting in more free electrons injected to STO conduction band and dominate the conductivity at the interface. The fact, that the free electrons at the interfaces are extremely sensitive to electric field, enables us to modulate metal-to-semiconductor transition by applying an external electric field.

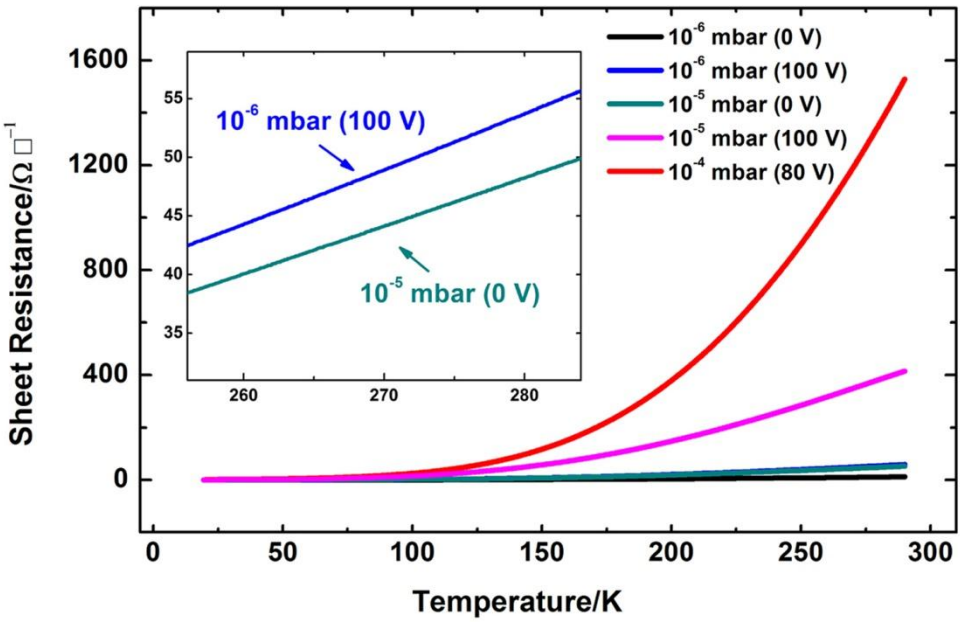

Figure 3.13 Temperature-dependent sheet resistance for samples applied with different gate voltages (V_G = 0, 80 and 100 V). Inset shows details of R_S of two very close curves between 255 ℃-285 ℃.

This result is significant because, analogous but not restrained to FETs built from conventional semiconductors, not only can we successfully control the doping level originated from the electronic reconstruction but also change the interface quantum state through the electrical means. In principle, this could also be realized in other compounds of strongly correlated electron systems. Interaction between gate voltage and quantum state of electrons may therefore produce novel electronic structures with unique properties.

3.6 Summary

In this chapter, the treatment technique on STO substrate to obtain TiO_2 terminated surface is discussed. Electronic transport properties of DSO/STO polar heterointerface grown at different oxygen pressure are successfully demonstrated with high mobility and carrier density. This system holds some similarities such as metallic behavior, high mobility and high carrier density compared to LAO/STO system but also presents new phenomena related the interface quantum states and metal-to-semiconductor (M-S) transition. The electric field effect characterization helps us to find out what happened at such a complex but interesting interface and has displayed the pronounced modulation of electric doping level and quantum phase transition. This heterostructure promises the potential interest for understanding quasi-two-dimensional electron gases (q2-DEG) as well as its applications in all-oxide device, thus opens new routes to complex oxide physics and ultimately for the design of devices in oxide electronics.

CHAPTER 4

EFFECT OF ARTIFICIAL $SrTiO_3$ ON $LaAlO_3/SrTiO_3$ HETEROINTERFACES

4.1 Introduction

STO is a kind of "magic" material, whose paraelectricity, induced ferroelectricity, quantum fluctuation, transport and structure related phase transition have been widely explored. As mentioned in Chapter 1 and discussed in last chapter, it is broadly believed that STO itself plays a vital role in generating q2-DEG at LAO/STO heterointerfaces. Moreover, although theoretically many calculations indicate no specifications of STO, practically all the systems so far reported and comprehensively accepted as q2-DEG systems have had to involve STO with no exceptions. Their calculations basically use $ATiO_3$, where *A* can denote different cations given non-polar atomic planes (in this case, the valence of *A* ion should be +2), and predict the presence of q2-DEG [118]. But to my best knowledge, some attempts have been made to replace STO by $CaTiO_3$ or $BaTiO_3$ (Ca, Ba both have bivalence) yet not successful. Apparently, these available "experimental truths" cannot be solely reconciled by "polar discontinuity" model, and can be suggestive of importance of STO. The reason of the necessity to keep STO "in the loop" in generating this q2-DEG is unclear.

Recently, it has been demonstrated by using appropriate annealing that the electron gas locates in the single crystal of STO but is confined near the interface [73, 123]. But there are still many questions are open for discussion. For example, what's the origin of the generation of the gas? Why can the transport in STO single crystal shows metallic behavior? Why is the gas confined at the interface? To try to answer these questions either theoretically or experimentally, one should consider a few

factors about STO, such as the dielectric behavior of STO, oxygen vacancies in STO and crystalline of STO, etc. (see Chapter 1 for reference). For example, regarding dielectric constant, Siemons et al. claimed that due to the large variation in dielectric properties of STO as a function of the temperature (approximately 24000 at 4 K, compared to about 300 at room temperature), the electron screening is enhanced and electrons can spread out over large distances, deeply inside STO crystal [125, 126]. On the contrary, by taking into account of the large electric-field dependence of the dielectric permittivity, Copie et al. showed that the gas actually remains confined even at low temperature, in agreement with their cross-sectional AFM results [73]. Other factors also have great impact on the q2-DEG, as will be partially discussed in this chapter.

Even though scientists are trying to capture the fundamental influences that STO has on generating the gas and to fabricate the gas by involving artificial STO (for example, growing STO films by PLD), so far all the q2-DEGs still need STO crystal, suggesting that without the STO substrate, the conductivity is lost. That is why it has not yet been possible to demonstrate multilayers with several q2-DEGs despite that numerous LAO/STO superlattices have been made and investigated [110], as shown in Fig. 4.1(a). Imagine that, if the q2-DEG can be formed between LAO layer and fabricated STO thin film by growing epitaxial STO directly on silicon [127], it will be able to create new electronic devices combining the q2-DEG in oxides with conventional semiconductor technologies.

On the other hand, upon the successful fabrication of q2-DEG on artificial STO, it is possible to have several conducting interfaces in superlattice or multilayers of LAO and STO. Since the interfaces are superconducting, one can probably observe the coupling effect between adjacent superconducting interfaces. Thus, the transition temperature of the system can be tuned and vortex dynamic can be studied through the superconducting coupling effect [128, 129]. Figs. 4.1(b) and (c) illustrate the reported work on superlattices composed of high-T_C superconductors.

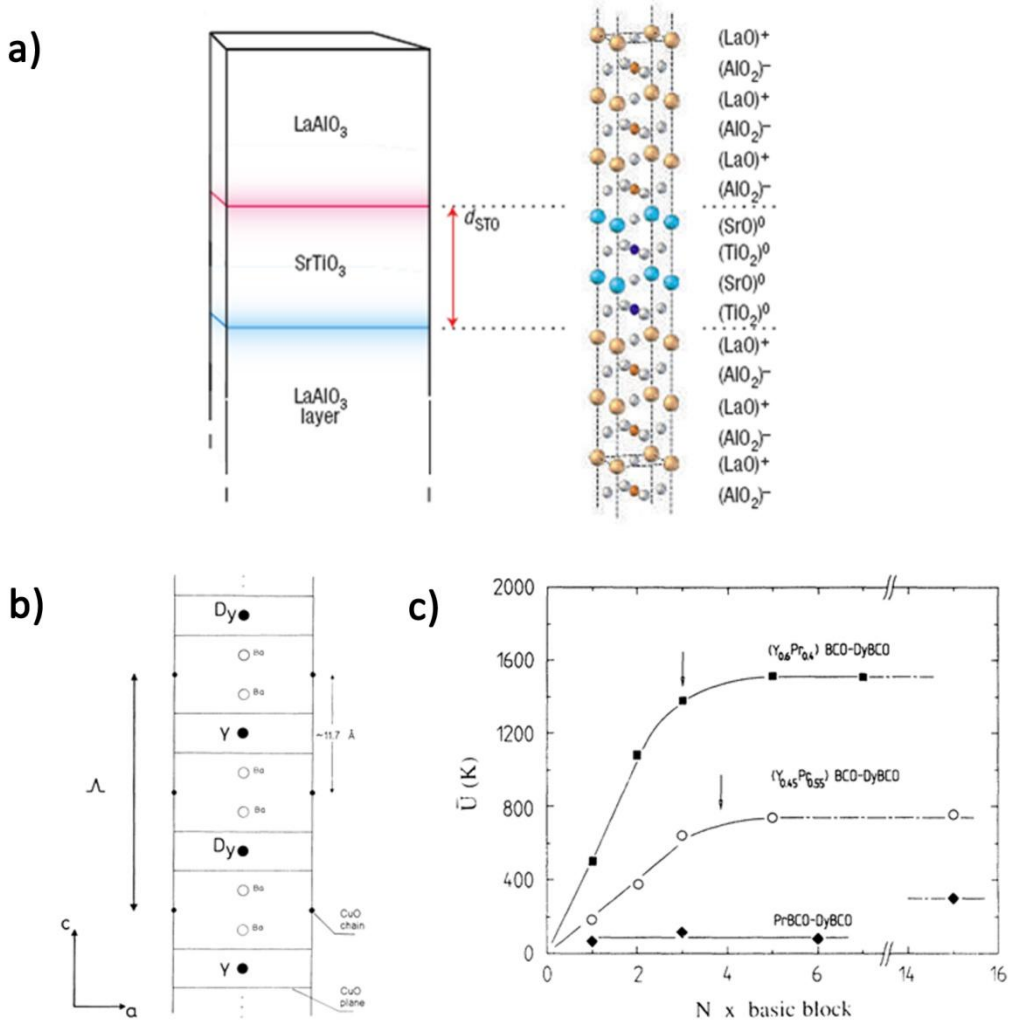

Figure 4.1 (a) Schematic view of a STO/LAO/STO heterostructure in a multilayer structure of LAO/STO (adopted from Ref. [110]); (b) Schematic representation of an ideal 24-Å-wavelength $Yba_2Cu_3O_7/DyBa_2Cu_3O_7$ multilayer (for details see Ref. [131]); (c) DyBCO-$(Y_{1-x}Pr_x)$BCO (x= 0.4, 0.55, and 1) activation energies as a function of N and for a field of 1 T (for details see Ref. [129]).

The work in this chapter was accomplished at Condensed Matter Physics Department, University of Geneva, under PolyU Oversea Research Student Attachment Program. By growing LAO on an artificial STO layer, which is grown by PLD on STO substrate at different growth temperatures, the influence of this STO interlayer to the conductivity of the interface has been studied. The phenomena found in the LAO/STO/STO structure may shed light on revealing the functions STO

possesses in LAO/STO heterointerfaces and possible of the origin of the phenomena will also be discussed. In addition, one should note that basically in all considerations from the available calculations for LAO/STO, fully oxidized artificial homoepitaxial STO layers have no particular difference from the STO single crystal substrates, which obviously cannot sufficiently interpret our results. In addition, the structural and transport properties of the LAO/artificial STO interfaces were also studied.

4.2 Experimental Details

4.2.1 General Procedures

Generally, the experiments undertaken in this work follow these procedures: (1) Grow STO on different single crystal substrates; (2) Take out the sample and treat the sample surface with BHF and annealing to obtain TiO_2 surface again; (3) Pattern the sample (see 4.2.3 for details); (4) Grow LAO on top of the patterned substrate; (5) Electrical characterization and topographic imaging by AFM (Digital Instrument Ⅲ).

4.2.2 Deposition

STO films were grown at different conditions (650 ℃ and 800 ℃ under 8×10^{-5} torr; and 1100 ℃ under 1×10^{-6} torr) and the thickness of STO films varied from 2 u.c. to 40 u.c. LAO films were grown at 800 ℃ under 8×10^{-5} torr and thickness of LAO films was kept as 5 u.c.. All films were grown by PLD, and Fig. 4.2 illustrates the designed structure.

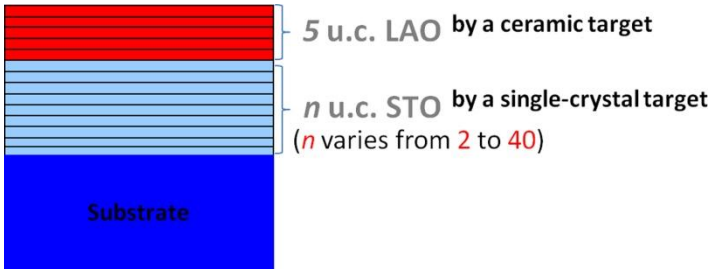

Figure 4.2 Sketch of the studied structure. STO was deposited from a single-crystal target, while LAO was deposited from a condensed ceramic target.

The laser repetition rate was kept at 1 Hz and the fluence of the laser pulses was 0.6 J cm^{-2}. The film growth was monitored *in-situ* using RHEED. After each deposition (for both STO and LAO), samples were annealed in 200 mbar of O_2 at about 540 ℃ for one hour and cooled down to room temperature in the same oxygen pressure. The samples were examined *ex-situ* by atomic force microscope to characterize the surface quality. All the as prepared STO/Substrate samples were treated by Buffered-HF solution and annealed in oxygen at 1000 ℃ to obtain precisely controlled TiO_2-terminated surfaces.

4.2.3 Sample Patterning Process and Measurements

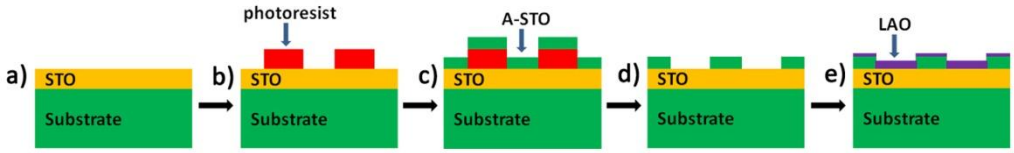

Figure 4.3 Representation of patterning process: (a) STO/Substrate sample; (b) photolithography; (c) deposition of amorphous STO; (d) lift-off; (e) deposition of LAO at deposition temperature.

A different sample patterning method to electrically contact the interface was exerted in this work. As illustrated in Fig. 4.3, the patterning process is basically accomplished before the final deposition of LAO layer. The soft mask with certain pattern [see Fig. 4.4(a)] was firstly made onto the as-treated STO/Substrate samples by photolithography. The pattern used here is a typical Hall bar geometry with terminals connected to pads for the convenience. Sequentially, amorphous STO was deposited onto the patterned sample (by PLD, 5 Hz, 6 minutes, 0.6 J cm^{-2}, at room temperature). After lift-off by acetone, the remnant amorphous STO with opposite patterns acted as the hard mask. Finally, LAO layer was deposited and the patterns can be clearly identified by eyes [see Fig. 4.4(b)] so that wire-bonding can be

performed to bond the pads in the pattern on the samples penetrating the thin LAO films to contact the interface [see Fig. 4.4(c)]. Since the LAO on top of bare crystalline STO is crystalline thus is conducting, while the LAO deposited onto the surface of amorphous STO is not conducting [see Fig. 4.4(d)], the contact interfaces can be patterned and contacted using wire-bonding in this manner.

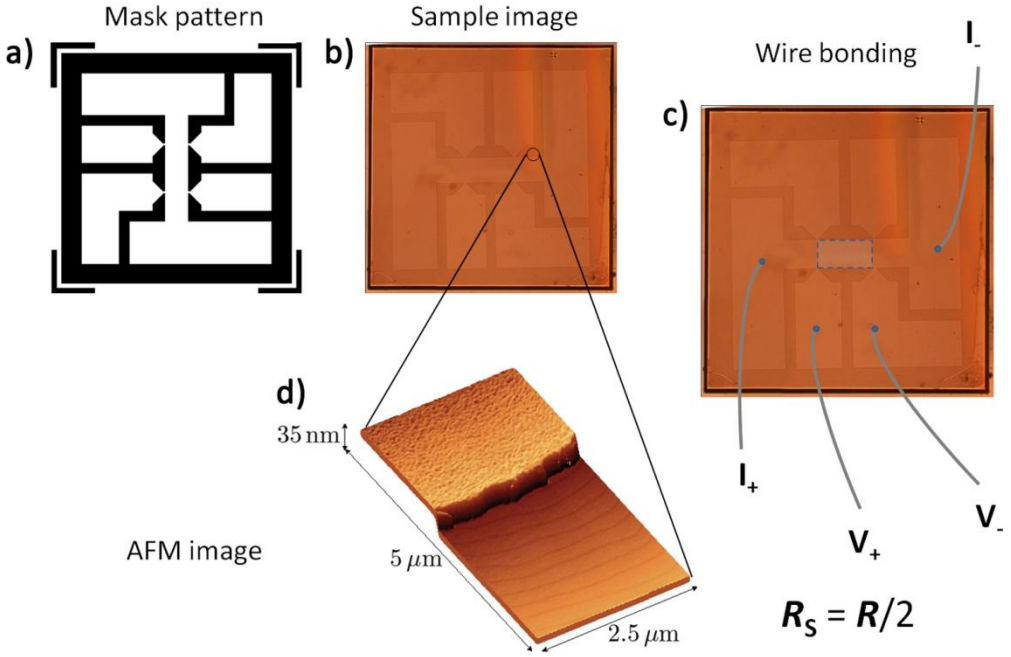

Figure 4.4 (a) Design of the mask pattern; (b) optical microscopic image of the sample after growth of LAO, from which the pattern can be clearly identified; (c) wire-bonding positions and configuration of sheet resistance measurement; (d) AFM 3D topography of the patterned sample, where the crystalline LAO shows clear steps and terraces structure. Amorphous and crystalline areas can be distinguished (image from C. Cancellieri).

As shown in Fig. 4.4(c), the length of the measured conducting area, which lies between the two measuring voltage terminals, is exactly two times of the width which is the width of the conducting channel. Therefore, according to the definition of sheet resistance introduced in Chapter 2, the sheet resistance can be obtained from the measurement using Hall bar geometry as below:

$$R_S = \frac{1}{2}R$$

where R_S is sheet resistance and R is the measured four-point measurement.

After the wire-bonding, the sheet resistance of the samples as a function of temperature was measured utilizing the setup demonstrated in Fig. 2.8(b) down to 4 K. The magnetotransport measurements versus temperature were performed in Oxford experimental facility or Janis system equipped with superconducting magnets (up to 8 T) and other current sources and nano-voltage meters down to 1.5 K.

4.3 Results and Discussion

In order to uncover the difference between the artificial STO layer and the single crystal STO of the effect on the electronic properties of the LAO/STO conducting interface, we firstly started with building up the LAO/STO interface on STO single crystal substrates.

4.3.1 In-situ Fabricated LAO/STO/STO Structure

Apparently, a straight forward way is to sequentially grow STO and LAO on STO substrates. This is represented as *in-situ* growth of LAO/STO/STO structure. During fabrication, the deposition temperature and oxygen pressure were maintained at 800 ℃ and 8×10^{-5} torr, respectively. STO was firstly grown on the substrate, and then 5-unit-cell LAO was grown on top. Figure 4.5 shows transport properties of this framework. It was found that the LAO/STO interface is *non*-conducting when the thickness of the STO interlayer is above 5 unit cells thick.

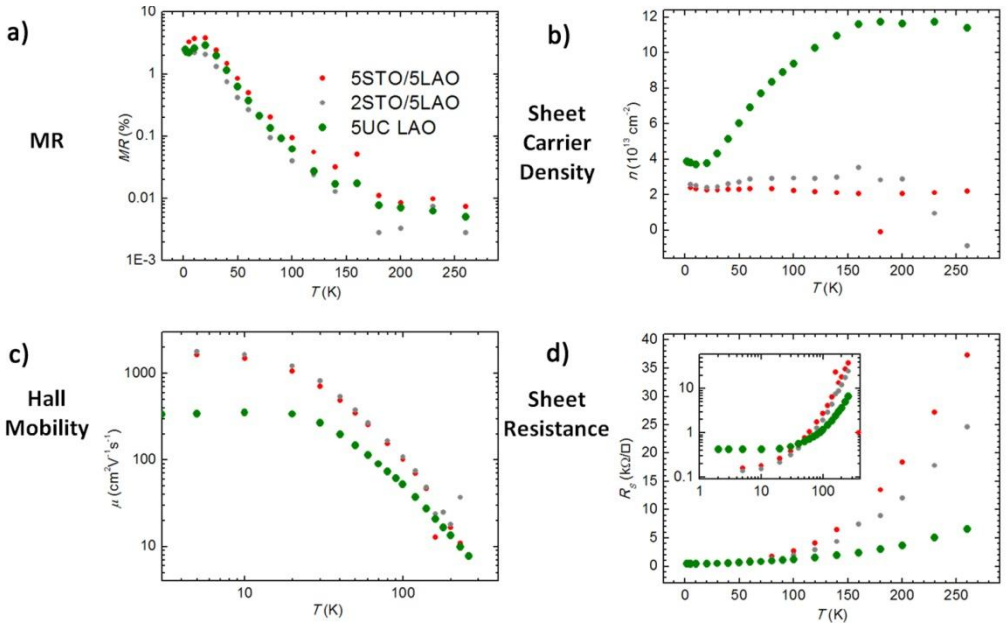

Figure 4.5 Transport properties versus temperature of in-situ fabricated LAO/STO/STO structure for different thickness of STO interlayer (red dots: 5 u.c., grey dots: 2 u.c. and green dots: only LAO): (a) magnetoresistance; (b) sheet carrier density; (c) carrier mobility; (d) sheet resistance. (Measurements conducted by N. Reyren and C. Cancellieri)

From the figure above, one should note that as the thickness of STO increases (below 5 u.c.) the carrier density drops, which means we lose some part of the mobile carriers when more artificial STO is added. But the question is that, is it due to the intrinsic factors of STO thin film? Or is it because of the non-perfect surface of STO thin film? Do mixed terminations have great impact on the conductivity of the LAO/artificial STO interfaces? What if we treat the surface of the STO interlayer? Since generally the quality of the STO thin films grown at typical temperatures is not very high and the dielectric constant of typical STO films is low, what if we deposit STO in step-flow mode at 1100 ℃?

In order to answer these questions, in the work reported below, we grow STO at different temperatures, then grow LAO on the treated artificial STO interlayer, and explore the transport properties of this so called ex-situ fabricated LAO/STO/STO

structure.

4.3.2 Ex-situ Fabricated LAO/STO/STO Structure

The deposition and treatment conditions are described 4.2. Note in this work, STO were grown at 800 ℃, 1100 ℃ and 650 ℃.

4.3.2.1 RHEED Monitoring of STO Growth

At 800 ℃, STO thin films grow on STO substrate homoepitaxially in 2D layer-by-layer mode, as introduced in Chapter 2. Figure 4.6 illustrates the specula spot RHEED intensity oscillations for monitoring the growth of STO with different thickness (10 u.c., 20 u.c. and 30 u.c. are shown here). From the RHEED intensity oscillations, we can count the exact number of unit cells.

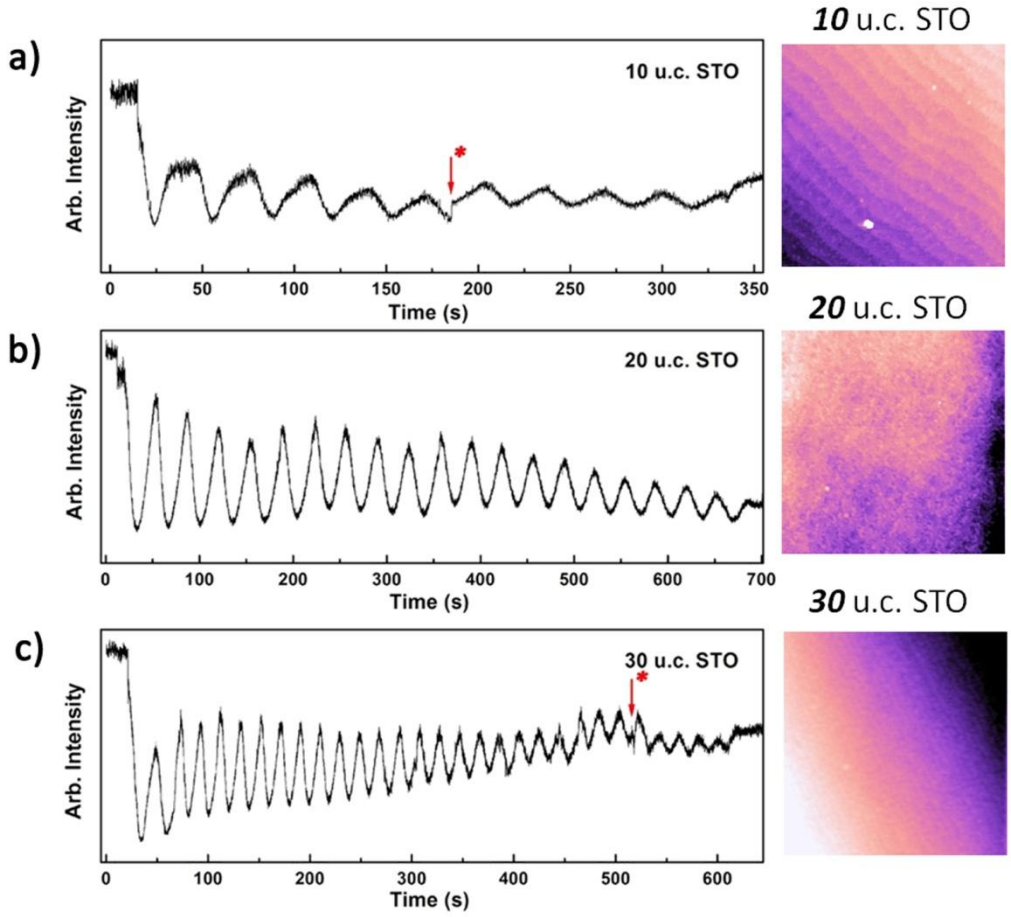

Figure 4.6 RHEED specula spot intensity oscillations and topography of the corresponding samples: (a) 10 u.c. STO/STO; (b) 20 u.c. STO/STO; (c) 30 u.c. STO/STO. (Red asterisks and the arrows indicate where the electron beam intensity is increased, and the dimension of all AFM images are 2μm.)

Figure 4.6 also shows AFM topographic images of the corresponding STO/STO samples, from which we can observe the surface morphology varies from sample to sample depending on the miscut angle of original STO substrate. In the sample of 10 u.c. STO, step-and-terrace structure is well preserved but some remnant hillock, which is believed to be SrO islands, can be observed. In contrast, for the sample of 20 u.c. STO, steps can hardly be seen, indicating that mixed termination dominates in this situation.

At 1100 ℃, typical laser parameters (1 Hz, 0.6 J cm^{-2}) and 1×10^{-6} torr growth ambient give rise to a step-flow growth for STO. After every laser pulse hit the target, the flux of atoms and ions is bombarded to form a plume. When the flux reaches the heated substrate, the atoms and ions are deposited to become adatoms, which are randomly distributed on the surface. This will increase the chaos of the surface thus the specula intensity decreases accordingly. However, due to the very high temperature, the adatoms can migrate to the edge of the terraces which is the thermodynamically stable status, therefore in this way the crystal is growing as steps are “flowing”. The diffusion time (relaxation time) of adatoms is shorter than the laser rest time. After the adatoms are bonded at the step edges and before next flux comes, the surface is in order as a well crystalline surface and the RHEED intensity fully recovers within one laser interval. In the step-flow growth, nucleation on the terraces is prevented. On the other hand, if the laser repetition rate is increased, for example, from 1 Hz to 5 Hz. Because of the shorted laser interval, there is not enough time for the adatoms to relax on the surface and they will nucleate on the terraces. As a result, layer-by-layer growth can recur. Figure 4.7 shows a typical step-flow growth of STO at 1100 ℃ and a layer-by-layer growth at the same temperature if the laser repetition rate is increased to 5 Hz.

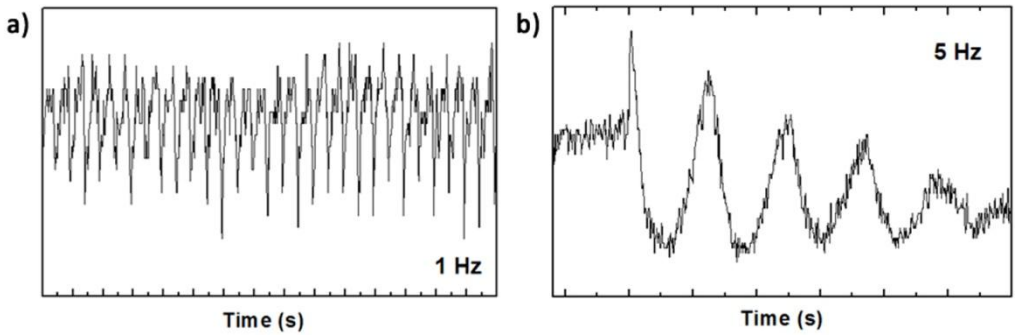

Figure 4.7 RHEED intensity oscillation of homoepitaxial STO grown at 1100 ℃; (a) at laser repetition of 1 Hz; (b) at laser repetition of 5 Hz.

4.3.2.2 Surface Morphology of STO/STO and LAO/STO/STO

Figure 4.8 displays the general overview of AFM topographic images of LAO/STO/STO samples for different thickness of STO interlayer grown at 800 ℃. The images were taken after the deposition of STO interlayer, after the BHF treatment on STO interlayer surfaces and after the growth of LAO.

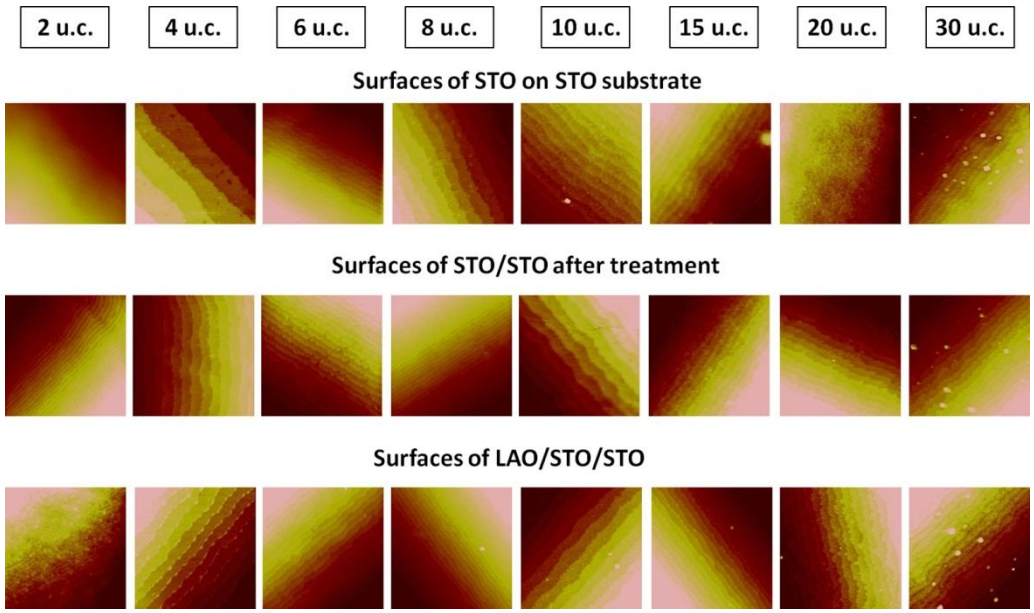

Figure 4.8 Overview of AFM topographic images of LAO/STO/STO samples for different thickness of STO interlayer grown at 800 ℃. Each column represents the images taken at different stages from the same sample with the same thickness of

STO interlayer.

The step-and-terrace structures can be seen for all the LAO/STO/STO samples listed in Fig. 4.8 for different STO interlayer thickness. However, the terrace width and surface roughness are varied from sample to sample, mainly depending on the substrate miscut angle. Note that after BHF treatment, SrO remnant are predominantly removed from the STO/STO surface.

Figure 4.9 shows topography of STO/STO samples with STO layers grown at 1100 ℃ and 1×10^{-6} torr. From the figure, one can see that the surface morphology is not always very smooth. In some samples [see Fig. 4.9(c)], the surface roughness is tremendously high and step-and-terrace structures are wrecked; while in some samples [see Figs. 4.9(b), (d) and (e)], the intended steps and terraces are well preserved. This is in accordance with the step-flow growth theory. Furthermore, in some samples, as shown in Fig. 4.9(a), steps can be observed, yet the step edges are extraordinarily rough filled with numerous pits and holes with one unit cell depth.

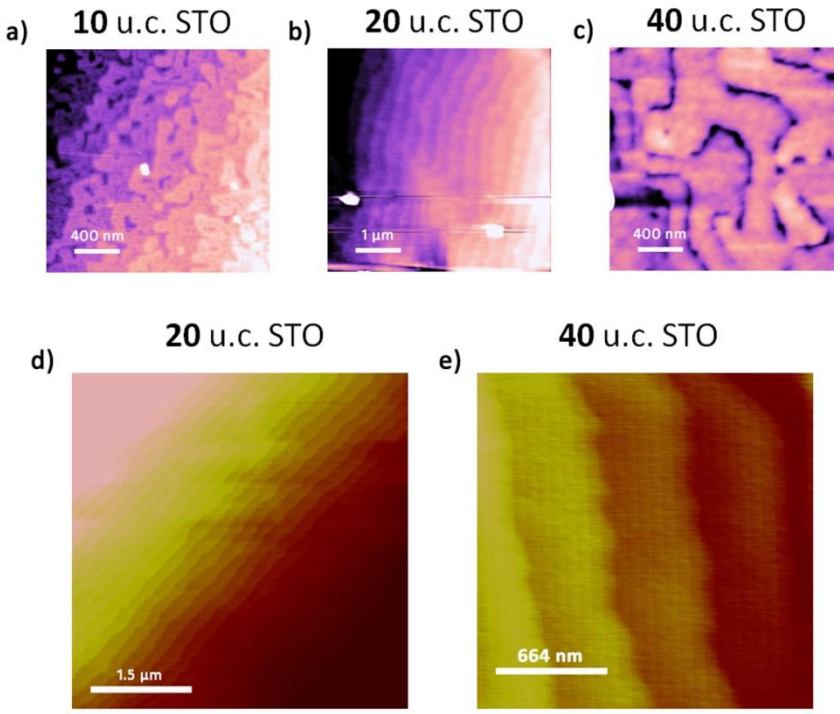

Figure 4.9 AFM topographic images of STO/STO surfaces with different STO layer thickness grown at 1100 ℃: (a) 10 u.c. STO; (b) 20 u.c. STO; (c) 40 u.c. STO; (d) 20 u.c. STO; (e) 40 u.c. STO.

4.3.2.3 Transport Properties of LAO/STO/STO

Figure 4.10(a) shows sheet resistance (R_S) of LAO/STO/STO interfaces, as a function of temperature (T) for different STO interlayer thickness (x in u.c.) grown at 800 ℃. From the graph, one can see that when x equals 15 or below, the interfaces are conducting and R_S vs. T curve shows metallic behavior, i.e. R_S decreases as T decreases, due to the weakened phonon scattering. Besides, R_S at room temperature follows the tendency that with increased x, R_S increases. When x approaches 20, the LAO/STO/STO interface shows a metal-to-insulator transition (MIT) and the structure becomes insulating (the resistance can be measurable down to 100 K but the R_S vs. T behaves as insulating). Finally, when x reaches 30, R_S is beyond the measurement limit thus not shown in the graph. The structure becomes completely insulating.

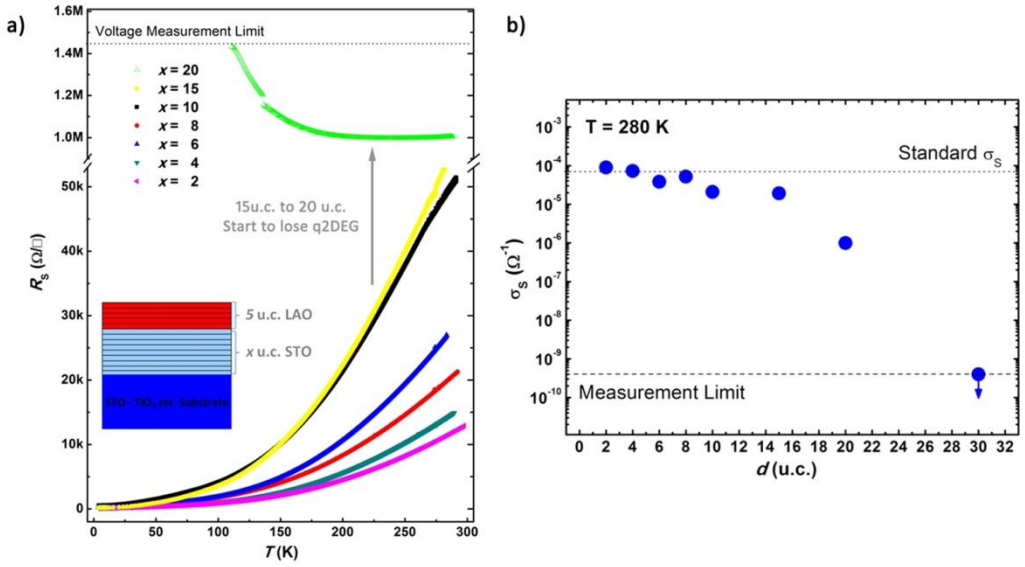

Figure 4.10 (a) Sheet resistance (R_S) of LAO/STO/STO interfaces with STO grown at 800 ℃ as a function of temperature (T) for different STO thickness (x); (b) sheet conductance (σ_S) at 280 K extracted from (a) as a function of x. The inset figure in (a)

recalls again the framework of the subject studied.

Sheet conductance can be extracted from Fig. 4.10(a) for different samples. As shown in Fig. 4.10(b), this metal-to-insulator tendency can be clearly identified from the sheet conductance (σ_S) at 280 K of LAO/STO/STO interfaces as a function of *x*. By comparing this result to the transport properties reported in 4.3.1, one can see that the critical thickness of STO interlayer, for LAO/STO interfaces to be conducting, is promoted from 5 u.c. to above 20 u.c (nearly 8 nm). But still, when the thickness exceeds this critical value, the conducting interface, i.e. q2-DEG is destroyed. This means that although the BHF treatment has favorable impact on the conductivity of the heterointerface, q2-DEG cannot be solely generated on artificial STO thin films.

Figure 4.11 shows the temperature-dependent sheet carrier density (n_S) and mobility (μ) extracted from Hall measurement of the above samples. It can be found that, the mobilities of the LAO/STO/STO interfaces, for different *x*, are at the same order of magnitude, as typical LAO/STO interfaces. However, from the figure, one can clearly see that, as *x* increases n_S drops. This probably suggests that, as the thickness of STO thin film increases, more carriers generated at the first interface (LAO/STO interface) suffer from more scattering by the defects created within STO layer during growth at typical temperatures and thus become localized. Consequently, at low temperatures, the carriers start to "freeze-out", giving rise to the metal-to-insulator transition as the thickness of STO increases.

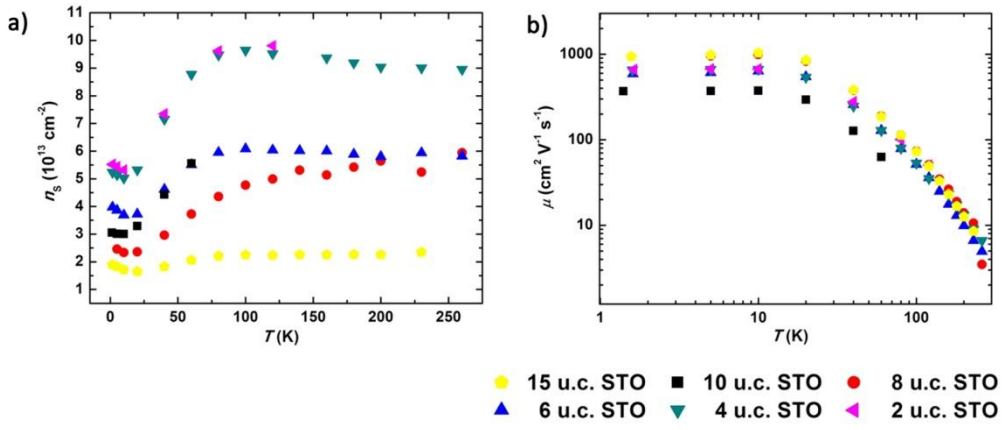

Figure 4.11 (a) Sheet carrier density (n_S) and (b) Hall mobility (μ) of LAO/STO/STO interfaces as a function of temperature for different STO thickness.

To more deeply reveal the relation between n_S and x, and understand the fact that, with presence of artificial STO, part of the carriers are "lost" or localized, the above results are re-plotted in Fig. 4.12. From Figs. 4.12(a) and (b), the tendency that as x increases, n_S and n_S-per-monolayer decrease.

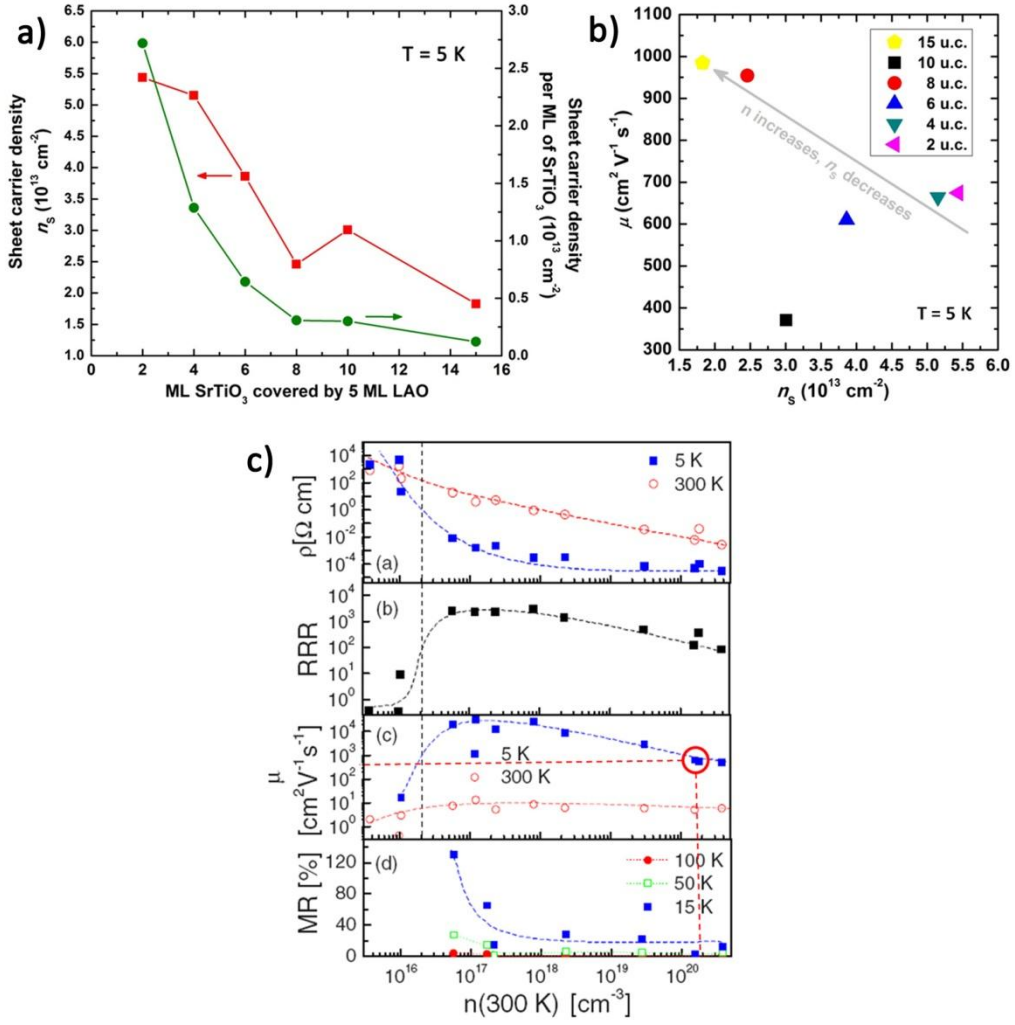

Figure 4.12 (a) Sheet carrier density and sheet carrier density per ML of STO as a function of STO layer thickness at T = 5 K; (b) mobility as a function of sheet carrier density for samples with different STO thickness at T = 5 K; (c) different transport properties of $SrTiO_{3-\delta}$ measured at 5 K and 300 K. The red circle and dashed line

indicate the regime we adopted to estimate the thickness of q2-DEG (adopted from Ref. [48]).

By considering the fact that μ of the samples for different x falls in the same order of magnitude and the q2-DEG is related to doped STO crystal, we can make a rough estimation for the thickness of q2-DEG generated in such LAO/STO/STO structures in light of the following equation:

$$n_{3D}(cm^{-3}) \cdot d = n_{2D}(cm^{-2})$$

where n_{3D} represents the 3D carrier density of doped bulk STO and n_{2D} represents the sheet carrier density of q2-DEG at LAO/STO interfaces. Using the n_{3D} value of the intersect of the vertical red dashed line and the x axis as indicated in Fig. 4.12(c), the thickness of the gas for the samples above can be calculated. For example, for the 4 u.c. STO interlayer, $d \approx 5$ nm; and for the 15 u.c. STO, $d \approx 1.1$ nm. Apparently, the thickness of the electron gas drops quickly as the thickness of STO layer increases. The gas is more confined for relatively thicker STO layer.

Figure 4.13 shows magnetoresistance (MR) as functions of perpendicular magnetic fields ($\mu_0 H_\perp$) and parallel magnetic fields ($\mu_0 H_{/\!/}$) up to 7 Tesla for LAO/STO/STO interfaces with different x. We can see that under applied perpendicular magnetic fields, the system holds positive MR while under applied parallel magnetic fields, the system has negative MR. This is in accordance with typical LAO/STO heterointerfaces. Moreover, the shape of the curves, especially at low fields, looks like prototypical LAO/STO system.

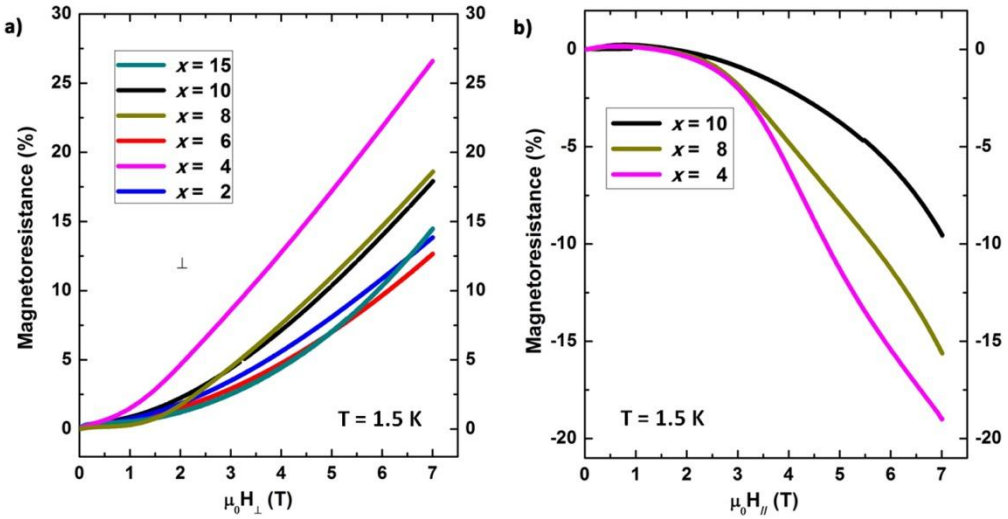

Figure 4.13 Magnetoresistance as a function of (a) perpendicular magnetic fields and (b) parallel magnetic fields for different LAO/STO/STO samples with different STO thickness.

For the LAO/STO/STO interfaces with STO grown at 1100 ℃, more or less as supposed, distinct $R_S(T)$ behavior was observed. As shown in Fig. 4.14, all the LAO/STO/STO samples with STO thickness up to 40 unit cells present metallic $R_S(T)$ behaviors. The sheet resistance keeps going down as temperature drops to cryogenic region. Figs. 4.14(b) and (c) display n_S and μ as a function of temperature down to 1.5 K. Similar to previous results obtained from "STO grown at 800 ℃" LAO/STO/STO samples, n_S drops as the STO thickness increases, probably also being a sign of charge localization happens in artificial STO layer.

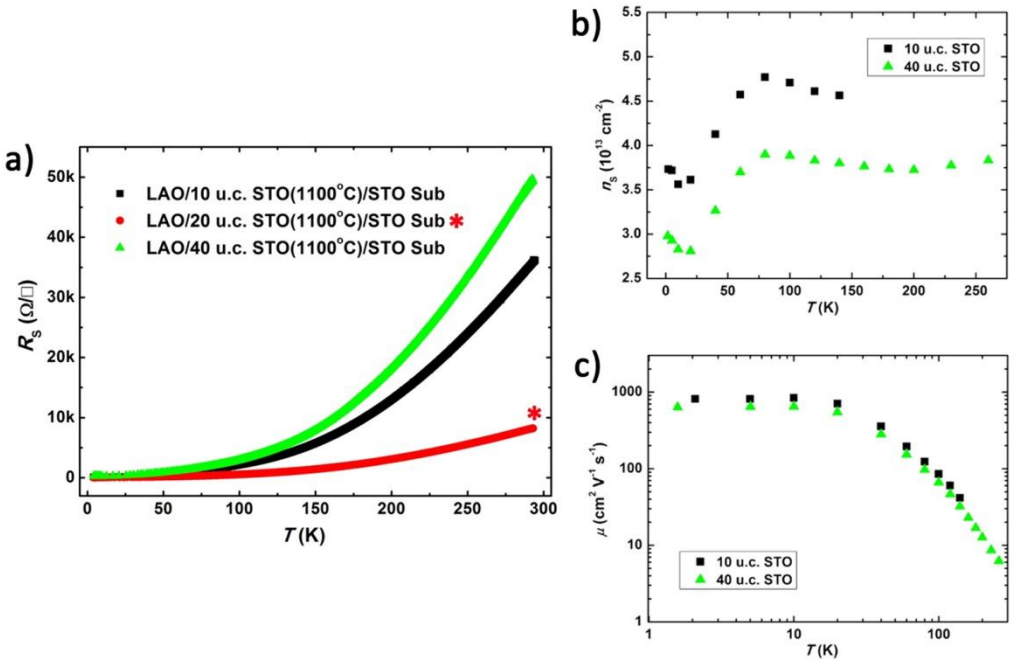

Figure 4.14 (a) Sheet resistance, (b) sheet carrier density and (c) mobility as a function of temperature for LAO/STO/STO interfaces with different thickness of STO grown at 1100 ℃ and 1×10^{-6} torr. (The sample labeled by an asterisk is broken and measured using general four-point configuration rather than Hall bar geometry.)

A comparison in temperature-dependent sheet resistance can thus be made for LAO/STO/STO structures with STO interlayer of constant thickness (20 u.c.) grown at different temperatures. From this, we can clearly witness the evolution of the transports of LAO/STO/STO samples as a function of STO growth temperature. For growth temperature of 650 ℃, samples show insulating behavior, with R_S over the measurement limit at RT. For growth temperature of 800 ℃ [see Fig. 4.15(a)], R_S is readable but shows characteristic $R_S(T)$ behavior down to around 110 K before it becomes immeasurable. When growth temperature is chosen to be 1100 ℃, it can be clearly seen in Fig. 4.15(b) that q2-DEG is preserved. This striking evolution can be interpreted as that, when growth temperature of STO interlayer increases from 650 ℃ to 1100 ℃ together with the growth mode changed from layer-by-layer to step-flow, the quality of STO interlayer is effectively improved thus diminishes the scatterings in artificial STO layer. As a result, charge localization in this layer is suppressed or

eliminated. The enhanced dielectric properties, as reported in Ref. [33] may also play important role in leading to diverse transport properties as the STO growth temperature varies.

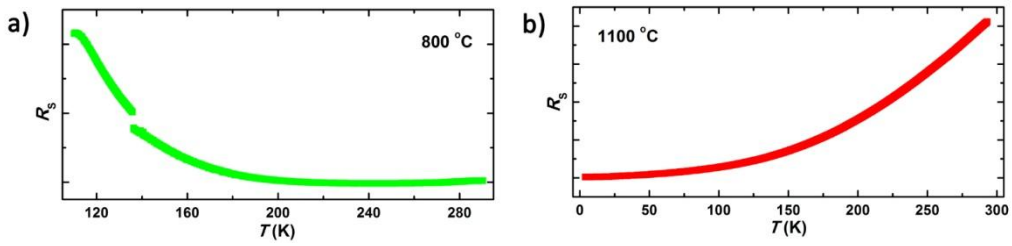

Figure 4.15 Sheet resistance of LAO/STO/STO interfaces with STO (20 u.c.) grown at different temperatures: (a) 800 ℃; (b) 1100 ℃.

4.3.3 *Ex-situ* Fabricated LAO/STO on Other Substrates

Due to the fascinating fact that the metallicity and q2-DEG can be preserved on the LAO/artificial STO heterointerface, we try to "get rid of" single-crystal STO substrates by growing STO at 1100 ℃ on other single-crystal substrates such as $DyScO_3$ (DSO) and $NdGaO_3$ (NGO). Figure 4.16(a) shows x-ray diffraction (XRD) patterns of STO thin films grown on DSO and NGO substrates. From top to bottom, the pink curve represents STO/DSO structure after BHF treatment and annealing process; the blue curve represents the same structure after deposition of STO and before the treatment; the red curve represents STO grown at 800 ℃ on an NGO substrate; the green curve represents STO grown at 1100 ℃ on an NGO substrate. One can see the fringes associated with the main STO peaks in the first three curves, but for STO grown at 1100 ℃ on NGO, these fringes are absent probably due to the intermixing between STO and NGO at high temperatures. One can also observe that the c-axis of STO shrinks when growth temperature on NGO substrates increases from 800 ℃ to 1100 ℃.

Although the structural aspects of the STO/DSO and STO/NGO structures are good, for example, RHEED intensity has the step-flow mode characteristics (not shown here) and XRD patterns are acceptably good indicating that STO films are

good, the LAO/STO/DSO and LAO/STO/NGO interfaces fabricated in this work show insulating behavior, as demonstrated in $R_S(T)$ curves in Fig. 4.16(b). The incredible difference in $R_S(T)$ for the heterostructures with STO grown at 1100 ℃ on STO and other perovskite substrates indicates that the crystal quality or dielectric constant of STO cannot be solely responsible for generating q2-DEG. Strain and the probable strain-induced defects in STO layer may have great influence on scattering the mobile electrons, resulting in elimination of q2-DEG. This proves that LAO/STO heterointerface is very sensitive to the by-components and other physical parameters; besides, it strongly relies on STO single crystal.

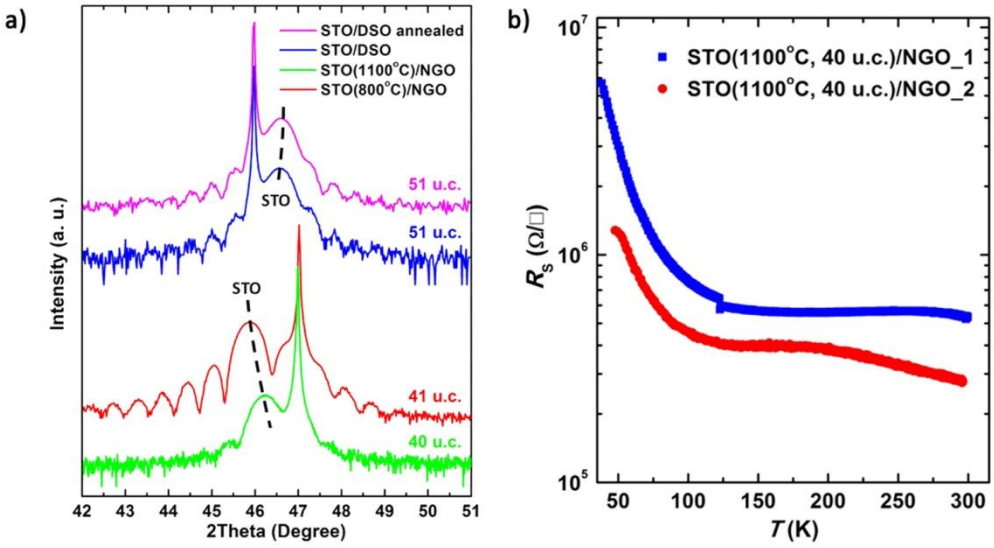

Figure 4.16 (a) X-ray diffractions around (002) peaks of STO thin films grown on DSO and NGO substrates; (b) sheet resistance vs. temperature for LAO/STO/NGO structures.

4.4 Summary

In this chapter, artificial STO was grown on different single-crystal perovskite substrates at different conditions, and LAO/STO heterointerfaces were fabricated on this artificial STO layer. By analyzing the structural as well as transport properties of these heterointerfaces, we summarize the results as below:

[1] The *in-situ* fabricated LAO/STO interface is non-conducting when the thickness of the STO interlayer is well above 5 unit cells.

[2] It appears that the surface *ex-situ* treatment, i.e. the surface termination control has great impact on the electronic properties of the interfaces.

[3] For the samples with LAO grown on *ex-situ* treated STO/STO surfaces, the conducting interface starts to disappear above a certain thickness of artificial STO layer (20 u.c. ≈ 8 nm) if STO is grown at 800 °C. And the number of charge carriers decreases regularly as the thickness increases.

[4] The conducting interface can be preserved at least up to 40 u.c. (≈ 16 nm) STO layer thick if STO is grown at 1100 ℃ and the surface is treated before LAO deposition. (Even the STO surface is not good.)

[5] So far, STO grown at high temperature (1100 ℃) on other perovskite substrates didn't give any sign of generation of q2-DEG at LAO/STO heterointerfaces built on the artificial STO layer, indicating the importance of single-crystal STO.

CHAPTER 5

CONCLUSION AND PERSPECTIVES

In conclusion, the methods to obtain single TiO_2-terminated STO substrate surfaces are explored and the high quality of surface is demonstrated. The DSO/STO heterointerface and the LAO/STO/STO heterostructure have been fabricated by Laser-MBE and PLD. Their structural and transport properties have been characterized and studied down to cryogenic region. The main results and discoveries of this project are summarized as follows:

[1] Electronic transport properties of DSO/STO polar heterointerface grown at different oxygen pressure by Laser-MBE are successfully demonstrated with high mobility and carrier density. Transport results show that this system holds some similarities such as metallic behavior, high mobility and high carrier density compared to LAO/STO system. It also exhibits characteristics regarding the interface quantum states and metal-to-semiconductor (M-S) transition. Field effect characterization reveals pronounced modulation of electric doping level and quantum phase transition. This heterostructure promises the potential interest for understanding quasi-two-dimensional electron gases (q2-DEG) as well as its applications in all-oxide device.

[2] Artificial STO was grown on different single-crystal perovskite substrates at different conditions by PLD, and the LAO/STO heterointerfaces were fabricated on this artificial STO layer. By analyzing the structural as well as transport properties of these heterointerfaces, it reveals that the surface *ex-situ* treatment, i.e. the surface termination control is vital for generation of q2-DEG at the interfaces. By treating the surface of the artificial STO thin film, the metallic q2-DEG can be preserved when the thickness of STO is above 5 u.c., obviously distinguished from *in-situ* grown LAO/artificial STO/STO interface. The

transport properties of the heterointerfaces with artificial STO layers grown at different deposition temperatures indicate that for typical growth temperatures, defects can be formed and accommodate in artificial STO layer thus become the scattering source for the mobile electrons. This results in the descending charge density as the STO thickness increases, before the charge "freeze-out" happens at low temperatures (for STO grown at 650 ℃ and 800 ℃, thickness above 20 u.c.). On the contrary, STO grown at high temperature (1100 ℃) is better crystallized, reducing the defects thus providing the foundations for the metallic transport of q2-DEG. Moreover, the intrinsic difference in the dielectric constant of STO grown at different temperatures may also have great impact on the existence of the q2-DEG. This work initiates a novel means to study fundamental questions regarding the origin of the q2-DEG discovered at LAO/STO interfaces. The success in building up LAO/artificial STO/STO heterostructure with preserved conducting interface lights up the ability to control q2-DEG on artificial STO and further incorporate oxide electronics with typical silicon-based devices.

[3] However, so far, STO grown at high temperature (1100 ℃) on other perovskite substrates didn't show the presence of q2-DEG at LAO/STO heterointerfaces built on the artificial STO layer, indicating the importance of single-crystal STO. More work needs to be done on enabling to build LAO/STO heterointerfaces on other perovskite substrates, and finally on silicon.

In future work, for the LAO/STO/STO heterostructures, in the case of STO grown at 800 ℃, since the number of carriers decreases with the increase of the thickness of STO layer, it is important to perform further transport measurements such as superconductivity measurement for the samples to estimate the q2-DEG thickness. The thickness of the q2-DEG can provide information on charge confinement and localization as well as other physical parameters of transport properties, helping understand the difference between the impact of STO thin films and of STO single crystals.

Potential applications of LAO/STO heterointerfaces are driven by combining the q2-DEG with ferromagnetic materials to fabricate spin injection devices and spin field effect transistors. By applying a gate voltage to the q2-DEG channel, the spin-polarization of electrons can be modified or changed through effective magnetic field induced by Rashba spin-orbit coupling. Even without the gate voltage, the conductivity which depends on the spin polarization can be tuned by changing the magnetizations in ferromagnetic source and drain electrodes. In future, the fabrication of such devices and the measurement of the spin-dependent conductivity in q2-DEG can be the focus of the extended work based on this project.

REFERENCES

[1] H. Kroemer, "Nobel Lecture: Quasielectric fields and band offsets: teaching electrons new tricks", *Rev. Mod. Phys.* **73**, 783 (2001).

[2] A. Tsukazaki, A. Ohtomo, T. Kita, Y. Ohno, H. Ohno, and M. Kawasaki, "Quantum Hall effect in polar oxide heterostructures", *Science* **315**, 1388 (2007).

[3] E. Bousquet, M. Dawber, N. Stucki, C. Lichtensteiger, P. Hermet, S. Gariglio, J.-M. Triscone, and Philippe Ghosez, "Improper ferroelectricity in perovskite oxide artificial superlattices", *Nature* **452**, 732 (2008).

[4] D. P. Norton, B. C. Chakoumakos, J. D. Budai, D. H. Lowndes, B. C. Sales, J. R. Thompson, and D. K. Christen, "Superconductivity in $SrCuO_2/BaCuO_2$ superlattices: Formation of artificially-layered super-conducting materials", *Science* **265**, 2074 (1994).

[5] K. S. Takahashi, M. Kawasaki, and Y. Tokura, "Interface ferromagnetism in oxide superlattices of $CaMnO_3/CaRuO_3$", *Appl. Phys. Lett.* **79**, 1324 (2001).

[6] A. Ohtomo and H. Y. Hwang, "A high-mobility electron gas at the $LaAlO_3/SrTiO_3$ heterointerface", *Nature* **427**, 423 (2004); Corrigendum: *Nature* **441**, 120 (2006).

[7] M. Johnsson and P. Lemmens, "Perovskites and thin films – crystallography and chemistry", *J. Phys.: Condens. Matter* **20**, 264001 (2008).

[8] D. A. Crandles, B. Nicholas, C. Dreher, C. C. Homes, A. W. McConnell, B. P. Clayman, W. H. Gong, and J. E. Greedan, "Optical properties of highly reduced $SrTiO_{3-x}$", *Phys. Rev. B* **59**, 12842 (1999).

[9] T. Matzke and M. Cappadonia, "Proton conductive perovskite solid solutions with enhanced mechanical stability", *Solid State Ionics* **86-88**, 659 (1996).

[10] O. N. Tufte and E. L. Stelzer, "Magnetoresistance in semiconducting strontium titanate", *Phys. Rev.* **173**, 775 (1968).

[11] B. F. Naylor and O. A. Cook, "High-temperature heat contents of the metatitanates of calcium, iron and magnesium", *J. Am. Chem. Soc.* **68**, 1003

(1946).

[12] B. Jaffe, W. R. Cook, and H. Jaffe, *Piezoelectric Ceramics*, Academic, London (1971).

[13] H. D. Megaw, "Crystal structure of barium titanate", *Nature* **155**, 484 (1945).

[14] G. Bednorz and K. A. Müller, "Possible high T_C superconductivity in the Ba-La-Cu-O system", *Z. Phys. B* **64**, 189 (1986).

[15] J.-H. Park, E. Vescovo, H.-J. Kim, C. Kwon, R. Ramesh, and T. Venkatesan, "Direct evidence for a half-metallic ferromagnet", *Nature* **392**, 794 (1998).

[16] W. Eerenstein, N. D. Mathur, and J. F. Scott, "Multiferroic and magnetoelectric materials", *Nature* **442**, 759 (2006).

[17] J. Wang, J. B. Neaton, H. Zheng, V. Nagarajan, S. B. Ogale, B. Liu, D. Viehland, V. Vaithyanathan, D. G. Schlom, U. V. Waghmare, N. A. Spaldin, K. M. Rabe, M. Wuttig, and R. Ramesh, "Epitaxial $BiFeO_3$ multiferroic thin film heterostructures", *Science* **299**, 1719 (2003).

[18] T. Sakudo and H. Unoki, "Dielectric properties of $SrTiO_3$ at low temperatures", *Phys. Rev. Lett.* **26**, 851 (1971).

[19] K. A. Müller and H. Burkard, "$SrTiO_3$: An intrinsic quantum paraelectric below 4 K", *Phys. Rev. B* **19**, 3593 (1979).

[20] H. P. R. Frederikse, W. R. Thurber, and W. R. Holser, "Electronic transport in strontium titanate", *Phys. Rev.* **134**, A442 (1964).

[21] J. F. Schooley, W. R. Hosler, and M. L. Cohen, "Superconductivity in Semiconducting $SrTiO_3$", *Phys. Rev. Lett.* **12**, 474 (1964).

[22] J. F. Schooley, W. R. Hosler, E. Ambler, J. H. Becker, M. L. Cohen, and C. S. Koonce, "Dependence of the superconducting transition temperature on carrier concentration in semiconducting $SrTiO_3$", *Phys. Rev. Lett.* **14**, 305 (1965).

[23] P. Chaudhari, R. H. Koch, R. B. Laibowitz, T. R. McGuire, and R. J. Gambino, "Critical-current measurements in epitaxial films of $YBa_2Cu_3O_{7-x}$ compound", *Phys. Rev. Lett.* **58**, 2684 (1987).

[24] E. L. Nagaev, "Colossal-magnetoresistance materials: Manganites and conventional ferromagnetic semiconductors", *Phys. Repts.* **346**, 387 (2001).

[25] G. Shirane and Y. Yamada, "Lattice-dynamical study of the 110 °phase transition

in $SrTiO_3$", *Phys. Rev.* **177**, 858 (1969).

[26] K. A. Müller, W. Berlinger, and F. Waldner, "Characteristic structural phase transition in perovskite-type compounds", *Phys. Rev. Lett.* **21**, 814 (1968).

[27] Z. P. Wu, "Structure and dielectric properties of epitaxial perovskite titanate thin films", *M. Phil. Thesis*, The Hong Kong Polytechnic University (2008).

[28] R. A. Cowley, "Temperature dependence of a transverse optic mode in strontium titanate", *Phys. Rev. Lett.* **9**, 159 (1962).

[29] W. Zhong, P. Zhang, Y. Wang, and T. Ren, "Size effect on the dielectric properties of $BaTiO_3$", *Ferroelectrics* **160**, 55 (1994).

[30] M. A. Saifi and L. E. Cross, "Dielectric properties of strontium titanate at low temperature", *Phys. Rev. B* **2**, 677 (1970).

[31] H.-M. Christen, J. Mannhart, E. J. Williams, and C. Gerber, "Dielectric properties of sputtered $SrTiO_3$ films", *Phys. Rev. B* **49**, 12095 (1994).

[32] M. Lippmaa, N. Nakagawa, M. Kawasaki, S. Ohashi, and H. Koinuma, "Dielectric properties of homoepitaxial $SrTiO_3$ thin films grown in the step-flow mode", *J. Electroceramics* **4**, 365 (2000).

[33] M. Lippmaa, N. Nakagawa, M. Kawasaki, S. Ohashi, Y. Inaguma, M. Itoh, and H. Koinuma, "Step-flow growth of $SrTiO_3$ thin films with a dielectric constant exceeding 10^4", *Appl. Phys. Lett.* **74**, 3543 (1999).

[34] J. H. Haeni, P. Irvin, W. Chang, R. Uecker, P. Reiche, Y. L. Li, S. Choudhury, W. Tian, M. E. Hawley, B. Craigo, A. K. Tagantsev, X. Q. Pan, S. K. Streiffer, L. Q. Chen, S. W. Kirchoefer, J. Levy, and D. G. Schlom, "Room-temperature ferroelectricity in strained $SrTiO_3$", *Nature* **430**, 758 (2004).

[35] I. Pallecchi, G. Grassano, D. Marré, L. Pellegrino, M. Putti, and A. S. Siri, "$SrTiO_3$-based metal–insulator–semiconductor heterostructures", *Appl. Phys. Lett.* **78**, 2244 (2001).

[36] P. Zubko, N. Stucki, C. Lichtensteiger, and J.-M. Triscone, "X-ray diffraction studies of 180° ferroelectric domains in $PbTiO_3/SrTiO_3$ superlattices under an applied electric field", *Phys. Rev. Lett.* **104**, 187601 (2010).

[37] J. Kim, Y. Kim, Y. S. Kim, J. Lee, L. Kim, and D. Jung, "Large nonlinear dielectric properties of artificial $BaTiO_3/SrTiO_3$ superlattices", *Appl. Phys. Lett.*

80, 3581 (2002).

[38] M. Bowen, A. Barthélémy, M. Bibes, E. Jacquet, J.-P. Contour, A. Fert, F. Ciccacci, L. Duo, and R. Bertacco, "Spin-polarized tunneling spectroscopy in tunnel junctions with half-metallic electrodes", *Phys. Rev. Lett.* **95**, 137203 (2005).

[39] C. H. Ahn, J.-M. Triscone, and J. Mannhart, "Electric field effect in correlated oxide systems", *Nature* **424**, 1015 (2003).

[40] C. H. Ahn, A. Bhattacharya, M. Di Ventra, J. N. Eckstein, C. D. Frisbie, M. E. Gershenson, A. M. Goldman, I. H. Inoue, J. Mannhart, A. J. Millis, A. F. Morpurgo, D. Natelson, and J.-M. Triscone, "Electrostatic modification of novel materials", *Rev. Mod. Phys.* **78**, 1185 (2006).

[41] M. Eblen-Zayas, A. Bhattacharya, N. E. Staley, A. L. Kobrinskii, and A. M. Goldman, "Ambipolar gate effect and low temperature magnetoresistance of ultrathin $La_{0.8}Ca_{0.2}MnO_3$ films", *Phys. Rev. Lett.* **94**, 037204 (2005).

[42] S. Ohta, T. Nomura, H. Ohta, and K. Koumoto, "High-temperature carrier transport and thermoelectric properties of heavily La- or Nb-doped $SrTiO_3$ single crystals", *J. Appl. Phys.* **97**, 034106 (2005).

[43] O. N. Tufte and P. W. Chapman, "Electron mobility in semiconducting strontium titanate", *Phys. Rev.* **155**, 796 (1967).

[44] S. Shapiro, "Phonon structure in tunneling in $SrTiO_3$", *Phys. Rev.* **140**, A169 (1965).

[45] A. Ferreira, J. Abrantes, J. Jurado, and J. Frade, "Oxygen stoichiometry of $Sr_{0.97}(Ti,Fe)O_{3-\delta}$ materials", *Solid State Ionics* **135**, 761 (2000).

[46] C. Shin, H. Yoo, and C. Lee, "Al-doped $SrTiO_3$: Part I, anomalous oxygen nonstoichiometry", *Solid State Ionics* **178**, 1081 (2007).

[47] J. Mannhart and D. G. Schlom, "Semiconductor physics: The value of seeing nothing", *Nature* **430**, 620 (2004).

[48] A. Spinelli, M. A. Torija, C. Liu, C. Jan, and C. Leighton, "Electronic transport in doped $SrTiO_3$: Conduction mechanisms and potential applications", *Phys. Rev. B* **81**, 155110 (2010).

[49] K. Szot, W. Speier, G. Bihlmayer, and R. Waser, "Switching the electrical

resistance of individual dislocations in single-crystalline $SrTiO_3$", *Nat. Mater.* **5**, 312 (2006).

[50] C. S. Koonce, M. L. Cohen, J. F. Schooley, W. R. Hosler, and E. R. Pfeiffer, "Superconducting transition temperatures of semiconducting $SrTiO_3$", *Phys. Rev.* **163**, 380 (1967).

[51] A. D. Caviglia, S. Gariglio, N. Reyren, D. Jaccard, T. Schneider, M. Gabay, S. Thiel, G. Hammerl, J. Mannhart, and J.-M. Triscone, "Electric field control of the $LaAlO_3/SrTiO_3$ interface ground state", *Nature* **456**, 624 (2008).

[52] A. Ohtomo and H. Y. Hwang, "Growth mode control of the free carrier density in $SrTiO_{3-\delta}$ films", *J. Appl. Phys.* **102**, 083704 (2007).

[53] K. Ueno, S. Nakamura, H. Shimotani, A. Ohtomo, N. Kimura, T. Nojima, H. Aoki, Y. Iwasa, and M. Kawasaki, "Electric-field-induced superconductivity in an insulator", *Nat. Mater.* **7**, 855 (2008).

[54] Y. Kozuka, M. Kim, C. Bell, B. G. Kim, Y. Hikita, and H. Y. Hwang, "Two-dimensional normal-state quantum oscillations in a superconducting heterostructure", *Nature* **462**, 487 (2009).

[55] J. Son, P. Moetakef, B. Jalan, O. Bierwagen, N. J. Wright, R. Engel-Herbert, and S. Stemmer, "Epitaxial $SrTiO_3$ films with electron mobilities exceeding 30,000 $cm^2 V^{-1} s^{-1}$", *Nat. Mater.* **9**, 482 (2010).

[56] H. P. R. Frederikse, W. R. Holser, and W. R. Thurber, "Magnetoresistance of semiconducting $SrTiO_3$", *Phys. Rev.* **143**, 648 (1966).

[57] R. Pool, "A transistor that works electron by electron", *Science* **249**, 629 (1990).

[58] M. Sundaram, S. A. Chalmers, P. F. Hopkins, and A. C. Gossard, "New quantum structures", *Science* **254**, 1326 (1991).

[59] K. V. Klitzing, G. Dorda, and M. Pepper, "New method for high-accuracy determination of the fine-structure constant based on quantized Hall resistance", *Phys. Rev. Lett.* **45**, 494 (1980).

[60] M. Breitschaft, V. Tinkl, N. Pavlenko, S. Paetel, C. Richter, J. R. Kirtley, Y. C. Liao, G. Hammerl, V. Eyert, T. Kopp, and J. Mannhart, "Two-dimensional electron liquid state at $LaAlO_3$-$SrTiO_3$ interfaces", *Phys. Rev. B* **81**, 153414 (2010).

[61] Y. Kawano, T. Uchida, and K. Ishibashi, "Terahertz sensing with a carbon nanotube/two-dimensional electron gas hybrid transistor", *Appl. Phys. Lett.* **95**, 083123 (2009).

[62] Y. Kawano and K. Ishibashi, "Scanning nanoelectrometer based on a two-dimensional electron gas transistor with a probe-integrated gate electrode", *Appl. Phys. Lett.* **96**, 142109 (2010).

[63] D. Dijkkamp, T. Venkatesan, X. D. Wu, S. A. Shaheen, N. Jisrawi, Y. H. Min-Lee, W. L. Mclean, and M. Croft, "Preparation of Y-Ba-Cu oxide superconductor thin films using pulsed laser evaporation from high T_C bulk material", *Appl. Phys. Lett.* **51**, 619 (1987).

[64] D. G. Schlom, J. N. Eckstein, E. S. Hellman, S. K. Streiffer, J. S. Harris, M. R. Beasley, J. C. Bravman, T. H. Geballe, C. Webb, K. E. von Dessonneck, and F. Turner, "Molecular beam epitaxy of layered Dy-Ba-Cu-O compounds", *Appl. Phys. Lett.* **53**, 1660 (1988).

[65] M. Kawasaki, K. Takahashi, T. Maeda, R. Tsuchiya, M. Shinohara, O. Ishiyama, T. Yonezawa, M. Yoshimoto, and H. Koinuma, "Atomic control of the $SrTiO_3$ crystal surface", *Science* **266**, 1540 (1994).

[66] G. J. H. M. Rijnders, G. Koster, D. H. A. Blank, and H. Rogalla, "*In situ* monitoring during pulsed laser deposition of complex oxides using reflection high energy electron diffraction under high oxygen pressure", *Appl. Phys. Lett.* **70**, 1888 (1997).

[67] N. Reyren, S. Thiel, A. D. Caviglia, L. Fitting Kourkoutis, G. Hammerl, C. Richter, C. W. Schneider, T. Kopp, A.-S. Rüetschi, D. Jaccard, M. Gabay, D. A. Muller, J.-M. Triscone, J. Mannhart, "Superconducting interfaces between insulating oxides", *Science* **317**, 1196 (2007).

[68] A. Brinkman, M. Huijben, M. van Zalk, J. Huijben, U. Zentler, J. C. Maan, W. G. van der Wiel, G. Rijnders, D. H. A. Blank, and H. Hilgenkamp, "Magnetic effects at the interface between non-magnetic oxides", *Nat. Mater.* **6**, 493 (2007).

[69] C. Cen, S. Thiel, J. Mannhart, and J. Levy, "Oxide nanoelectronics on demand", *Science* **323**, 1026 (2009).

[70] M. Salluzzo, J. C. Cezar, N. B. Brookes, V. Bisogni, G. M. De Luca, C. Richter,

S. Thiel, J. Mannhart, M. Huijben, A. Brinkman, G. Rijnders, and G. Ghiringhelli, "Orbital reconstruction and the two-dimensional electron gas at the $LaAlO_3/SrTiO_3$ interface", *Phys. Rev. Lett.* **102**, 166804 (2009).

[71] C. Bell, S. Harashima, Y. Kozuka, M. Kim, B. G. Kim, Y. Hikita, and H.Y. Hwang, "Dominant mobility modulation by the electric field effect at the $LaAlO_3/SrTiO_3$ interface", *Phys. Rev. Lett.* **103**, 226802 (2009).

[72] A. D. Caviglia, M. Gabay, S. Gariglio, N. Reyren, C. Cancellieri, and J.-M. Triscone, "Tunable Rashba spin-orbit interaction at oxide interfaces", *Phys. Rev. Lett.* **104**, 126803 (2010).

[73] O. Copie, V. Garcia, C. Bödefeld, C. Carrétéro, M. Bibes, G. Herranz, E. Jacquet, J.-L. Maurice, B. Vinter, S. Fusil, K. Bouzehouane, H. Jaffrès, and A. Barthélémy, "Towards two-dimensional metallic behavior at $LaAlO_3/SrTiO_3$ interfaces", *Phys. Rev. Lett.* **102**, 216804 (2009).

[74] W. Son, E. Cho, B. Lee, J. Lee, and S. Han, "Density and spatial distribution of charge carriers in the intrinsic n-type $LaAlO_3$-$SrTiO_3$ interface", *Phys. Rev. B* **79**, 245411 (2009).

[75] J. Lee and A. A. Demkov, "Charge origin and localization at the n-type $SrTiO_3/LaAlO_3$ interface", *Phys. Rev. B* **78**, 193104 (2008).

[76] R. Pentcheva and W. E. Pickett, "Avoiding the polarization catastrophe in $LaAlO_3$ overlayers on $SrTiO_3$(001) through polar distortion", *Phys. Rev. Lett.* **102**, 107602 (2009).

[77] Z. S. Popović, S. Satpathy, and R. M. Martin, "Origin of the two-dimensional electron gas carrier density at the $LaAlO_3$ on $SrTiO_3$ interface", *Phys. Rev. Lett.* **101**, 256801 (2008).

[78] S. Okamoto, A. J. Millis, and N. A. Spaldin, "Lattice relaxation in oxide heterostructures: $LaTiO_3/SrTiO_3$ superlattices", *Phys. Rev. Lett.* **97**, 056802 (2006).

[79] J. Mannhart, D. H. A. Blank, H. Y. Hwang, A. J. Millis, J.-M. Triscone, "Two dimensional electron gases at oxide interfaces", *MRS Bulletin* **33**, 1027 (2008).

[80] S. Okamoto, A. J. Millis, "Electronic reconstruction at an interface between a Mott insulator and a band insulator", *Nature* **428**, 630 (2004).

[81] G. Herranz, M. Basletic, M. Bibes, C. Carretero, E. Tafra, E. Jacquet, K. Bouzehouane, C. Deranlot, A. Hamzic, J. M. Broto, A. Barthélémy, and A. Fert, "High mobility in $LaAlO_3/SrTiO_3$ heterostructures: Origin, dimensionality, and perspectives", *Phys. Rev. Lett.* **98**, 216803 (2007).

[82] H. Lehnert, H. Boysen, J. Schneider, F. Frey, D. Hohlwein, P. Radaelli, and H. Ehrenberg, "A powder diffraction study of the phase transition in $LaAlO_3$", *Z. Kristallogr.* **412**, 536 (2000).

[83] S. A. Hayward, F. D. Morrison, S. A. T. Redfern, E. K. H. Salje, J. F. Scott, K. S. Knight, S. Tarantino, A. M. Glazer, V. Shuvaeva, P. Daniel, M. Zhang, and M. A. Carpenter, "Transformation processes in $LaAlO_3$: Neutron diffraction, dielectric, thermal, optical, and Raman studies", *Phys. Rev. B* **72**, 054110 (2005).

[84] R. W. Simon, C. E. Platt, A. E. Lee, G. S. Lee, K. P. Daly, M. S. Wire, and J. A. Luine, "Low-loss substrate for epitaxial growth of high-temperature superconductor thin films", *Appl. Phys. Lett.* **53**, 2677 (1988).

[85] P. Delugas, V. Fiorentini, and A. Filippetti, "Dielectric properties and long-wavelength optical modes of the high-κ oxide $LaAlO_3$", *Phys. Rev. B* **71**, 134302 (2005).

[86] X. B. Lu, P. F. Lee, and J. Y. Dai, "Synthesis and memory effect study of Ge nanocrystals embedded in $LaAlO_3$ high-*k* dielectrics", *Appl. Phys. Lett.* **86**, 203111 (2005).

[87] G. A. Baraff, J. A. Appelbaum, and D. R. Hamann, "Self-consistent calculation of the electronic structure at an abrupt GaAs-Ge interface", *Phys. Rev. Lett.* **38**, 237 (1976).

[88] H. Y. Hwang, "Applied physics: Tuning interface states", *Science* **313**, 1895 (2006).

[89] S. Thiel, G. Hammerl, A. Schmehl, C. W. Schneider, and J. Mannhart, "Tunable quasi-two-dimensional electron gases in oxide heterostructures", *Science* **313**, 1942 (2006).

[90] M. Ben Shalom, M. Sachs, D. Rakhmilevitch, A. Palevski, and Y. Dagan, "Tuning spin-orbit coupling and superconductivity at the $SrTiO_3/LaAlO_3$ interface: A magnetotransport study", *Phys. Rev. Lett.* **104**, 126802 (2010).

[91] N. Reyren, S. Gariglio, A. D. Caviglia, D. Jaccard, T. Schneider, and J.-M. Triscone, "Anisotropy of the superconducting transport properties of the $LaAlO_3/SrTiO_3$ interface", *Appl. Phys. Lett.* **94**, 112506 (2009).

[92] M. Ben Shalom, C. W. Tai, Y. Lereah, M. Sachs, E. Levy, D. Rakhmilevitch, A. Palevski, and Y. Dagan, "Anisotropic magnetotransport at the $SrTiO_3/LaAlO_3$ interface", *Phys. Rev. B* **80**, 140403(R) (2009).

[93] C. W. Schneider, S. Thiel, G. Hammerl, C. Richter, and J. Mannhart, "Microlithography of electron gases formed at interfaces in oxide heterostructures", *Appl. Phys. Lett.* **89**, 122101 (2006).

[94] C. Cen, S. Thiel, G. Hammerl, C. W. Schneider, K. E. Andersen, C. S. Hellberg, J. Mannhart, and J. Levy, "Nanoscale control of an interfacial metal–insulator transition at room temperature", *Nat. Mater.* **7**, 298 (2008).

[95] D. F. Bogorin, C. W. Bark, H. W. Jang, C. Cen, C. M. Folkman, C.-B. Eom, and J. Levy, "Nanoscale rectification at the $LaAlO_3/SrTiO_3$ interface", *Appl. Phys. Lett.* **97**, 013102 (2010).

[96] G. Koster, B. L. Kropman, G. J. H. M. Rijnders, D. H. A. Blank, and H. Rogalla, "Quasi-ideal strontium titanate crystal surfaces through formation of strontium hydroxide", *Appl. Phys. Lett.* **73**, 2920 (1998).

[97] T. Ohnishi, K. shibuya, M. Lippmaa, D. Kobayashi, H. Kumigashira, M. Oshima, and H. Koinuma, "Preparation of thermally stable TiO_2-terminated $SrTiO_3$ (100) substrate surfaces", *Appl. Phys. Lett.* **85**, 272 (2004).

[98] D. Kobayashi, H. Kumigashira, M. Oshima, T. Ohnishi, M. Lippmaa, K. Ono, M. Kawasaki, and H. Koinuma, "High-resolution synchrotron-radiation photoemission characterization for atomically-controlled $SrTiO_3$ (001) substrate surfaces subjected to various surface treatments", *J. Appl. Phys.* **96**, 7183 (2004).

[99] M. Kareev, S. Prosandeev, J. Liu, C. Gan, A. Kareev, J. W. Freeland, M. Xiao, and J. Chakhalian, "Atomic control and characterization of surface defect states of TiO_2 terminated $SrTiO_3$ single crystals", *Appl. Phys. Lett.* **93**, 061909 (2008).

[100] J. Zhang, D. Doutt, T. Merz, J. Chakhalian, M. Kareev, J. Liu, and L. J. Brillson, "Depth-resolved subsurface defects in chemically etched $SrTiO_3$", *Appl. Phys. Lett.* **94**, 092904 (2009).

[101] A. E. Espinal, L. Zhang, C.-H. Chen, A. Morey, Y. Nie, L. Espinal, B. O. Wells, R. Joesten, M. Aindow, and S. L. Suib, "Nanostructured arrays of semiconducting octahedral molecular sieves by pulsed-laser deposition", *Nat. Mater.* **9**, 54 (2010).

[102] D. B. Geohegan, "Physics and diagnostics of laser ablation plume propagation for high-T_C superconductor film growth", *Thin Solid Films* **220**, 138 (1992).

[103] M. Kanai and T. Kawai, "Superconductivity of (Ba,Sr,Ca)CuO_2 Artificial Lattices", *Phys. C* **235-240**, 174 (1994).

[104] S. Thiel, "Study of interface properties in $LaAlO_3/SrTiO_3$ heterostructures", *Ph.D. Thesis*, University of Augsburg (2009).

[105] F.C. Frank and J.H. van der Merwe, "One-dimensional dislocations. I. static theory", *Proc. Roy. Soc. London A* **198**, 205 (1949).

[106] M. Volmer and A. Weber, "Nuclei formation in supersaturated states", *Z. Phys. Chem.* **119**, 277 (1926).

[107] I.N. Stranski and Krastanov, "Theory of orientation separation of ionic crystals", *Acad. Wiss. Math.-Naturw. Klasse IIb* **146**, 797 (1938).

[108] W. Braun, *Applied RHEED: Reflection High-Energy Electron Diffraction During Crystal Growth*, Springer, Berlin (1999).

[109] Wikipedia, *Atomic force microscopy*: http://en.wikipedia.org/wiki/Atomic_force_microscope

[110] M. Huijben, G. Rijnders, D.H.A. Blank, S. Bals, S. Van Aert, J. Verbeeck, G. Van Tendeloo, A. Brinkman, and H. Hilgenkamp, "Electronically coupled complementary interfaces between perovskite band insulators", *Nat. Mater.* **5**, 556 (2006).

[111] A. Kalabukhov, R. Gunnarsson, J. Borjesson, E. Olsson, T. Claeson, and D. Winkler, "Effect of oxygen vacancies in the $SrTiO_3$ substrate on the electrical properties of the $LaAlO_3/SrTiO_3$ interface", *Phys. Rev. B* **75**, 121404(R) (2007).

[112] L. J. van der Pauw, "A method of measuring specific resistivity and Hall effect of discs of arbitrary shape", *Philips Res. Repts.* **13**, 1 (1958).

[113] Wikipedia, *Van der Pauw method*: http://en.wikipedia.org/wiki/Van_der_Pauw_method

[114] Wikipedia, *Hall effect*: http://en.wikipedia.org/wiki/Hall_effect

[115] N. Nakagawa, H. Y. Hwang, and D. A. Muller, "Why some interfaces cannot be sharp", *Nature Mater.* **5**, 204 (2006).

[116] A. Ohtomo, D. A. Muller, J. L. Grazul, and H. Y. Hwang, "Artificial charge-modulation in atomic-scale perovskite titanate superlattices", *Nature* **419**, 378 (2002).

[117] A. Kalabukhov, R. Gunnarsson, T. Claeson, and D. Winkler, "Electrical transport properties of polar heterointerface between $KTaO_3$ and $SrTiO_3$", arXiv: 0704.1050v1 (2007).

[118] M. K. Niranjan, Y. Wang, S. S. Jaswal, and E. Y. Tsymbal, "Prediction of a switchable two-dimensional electron gas at ferroelectric oxide interfaces", *Phys. Rev. Lett.* **103**, 016804 (2009).

[119] P. Perna, D. Maccariello, M. Radovic, U. S. Uccio, I. Pallecchi, M. Codda, D. Marré, C. Cantoni, J. Gazquez, M. Varela, S. Pennycook, and F. M. Granozio, "Novel conducting interfaces between band insulating oxides", arXiv: 1001.3956v1 (2010).

[120] M. Luysberg, M. Heidelmann, L. Houben, M. Boese, T. Heeg, J. Schubert, and M. Roeckerath, "Intermixing and charge neutrality at $DyScO_3/SrTiO_3$ interfaces", *Acta Mater.* **57**, 3192 (2009).

[121] D. Kan, T. Terashima, R. Kanda, A. Masuno, K. Tanaka, S. Chu, H. Kan, A. Ishizumi, Y. Kanemitsu, Y. Shimakawa, and M. Takano, "Blue-light emission at room temperature from Ar^+-irradiated $SrTiO_3$", *Nat. Mater.* **4**, 816 (2005).

[122] H. Ihrig, J. H. T. Hengst, and M. Klerk, "Conductivity-dependent cathodoluminescence in $BaTiO_3$, $SrTiO_3$ and TiO_2", *Z. Phys. B: Condens. Matter* **40**, 301 (1981).

[123] M. Basletic, J.-L. Maurice, C. Carrétéro, G. Herranz, O. Copie, M. Bibes, É. Jacquet, K. Bouzehouane, S. Fusil, and A. Barthélémy, "Mapping the spatial

distribution of charge carriers in $LaAlO_3/SrTiO_3$ heterostructures", *Nat. Mater.* **7**, 621 (2008).

[124] Y. Segal, J. H. Ngai, J. W. Reiner, F. J. Walker, and C. H. Ahn, "X-ray photoemission studies of the metal-insulator transition in $LaAlO_3/SrTiO_3$ structures grown by molecular beam epitaxy", *Phys. Rev. B* **80**, 241107 R (2009).

[125] W. Siemons, G. Koster, H. Yamamoto, W. A. Harrison, G. Lucovsky, T. H. Geballe, D. H. A. Blank, and M. R. Beasley, "Origin of charge density at $LaAlO_3$ on $SrTiO_3$ heterointerfaces: Possibility of intrinsic doping", *Phys. Rev. Lett.* **98**, 196802 (2007).

[126] W. Siemons, M. Huijben, G. Rijnders, D. H. A. Blank, T. H. Geballe, M. R. Beasley, and G. Koster, "Dielectric-permittivity-driven charge carrier modulation at oxide interfaces", *Phys. Rev. B* **81**, 241308(R) (2010).

[127] X. Y. Zhou, J. Miao, J. Y. Dai, H. L. W. Chan, C. L. Choy, Y. Wang, and Q. Li, "Epitaxial growth of $SrTiO_3$ thin film on Si by laser molecular beam epitaxy", *Appl. Phys. Lett.* **90**, 012902 (2007).

[128] J.-M. Triscone, M. G. Karkut, L. Antognazza, O. Brunner, and Ø. Fischer, "Y-Ba-Cu-O/Dy-Ba-Cu-O superlattices: A first step towards the artificial construction of high-T_C superconductors", *Phys. Rev. Lett.* **63**, 1016 (1989).

[129] J.-M. Triscone, P. Fivat, M. Andersson, M. Decroux, and Ø. Fischer, "Two-dimensional and three-dimensional vortex lattice dynamics in $DyBa_2Cu_3O_7$-$(Y_{1-x}Pr_x)Ba_2Cu_3O_7$ coupled heterostructures", *Phys. Rev. B* **50**, 1229 (1994).